

TECHNICAL MEMORANDUM

X-139

Declassified by authority of NASA
Classification Change Notices No. 214
Dated *1-5-SEP-1971

ANALYSIS OF PRESSURE DISTRIBUTIONS FOR A
SERIES OF CONTROLS ON A 40° SWEPTBACK
WING AT A MACH NUMBER OF 1.61

By Douglas R. Lord

Langley Research Center
Langley Field, Va.

CLASSIFICATION CHANGED
UNCLASSIFIED

TO

NASA 10.71-350 3/20/71

N71-7343 II

(ACCESSION NUMBER)

(THRU)

(PAGES)

(CODE)

(NASA CR OR TMX OR AD NUMBER)

(CATEGORY)

FACILITY FORM 602

NATIONAL AERONAUTICS AND SPACE ADMINISTRATION
WASHINGTON

November 1959

~~CONFIDENTIAL~~

NATIONAL AERONAUTICS AND SPACE ADMINISTRATION

TECHNICAL MEMORANDUM X-139

ANALYSIS OF PRESSURE DISTRIBUTIONS FOR A
SERIES OF CONTROLS ON A 40° SWEEPBACK

WING AT A MACH NUMBER OF 1.61*

By Douglas R. Lord

SUMMARY

An investigation has been made at a Mach number of 1.61 and Reynolds numbers of 1.7×10^6 and 3.6×10^6 to determine the pressure distributions over a swept wing with a series of eight control configurations. The wing had 40° of sweep of the quarter-chord line, an aspect ratio of 3.1, and a taper ratio of 0.4. Tests were made at angles of attack from -15° to 15° for control deflections from -60° to 60°.

The basic wing pressure distributions indicated a weak oblique shock on the low-pressure side of the wing. At control deflections from -10° to 20° the pressure changes on the trailing-edge controls were limited in chordwise extent to the control surface and changed regularly with control deflection. At negative control deflections of -20° and greater, separation or shock detachment occurred ahead of the hinge line and increased in chordwise extent with outboard movement along the span and with increasingly negative control deflections. Linear-theory predictions of the pressures due to control deflection were only fair because of viscous and shock-detachment effects not considered by theory. The predictions of the pressures due to angle of attack were somewhat better at low control deflections.

On the flap-type controls, increasing the trailing-edge thickness increased the pressures on the control and in the separated or detached-shock region ahead of the control, and moving the hinge line rearward reduced the pressures on the high-pressure side of the control and altered the flow separation or shock detachment ahead of the control.

INTRODUCTION

As part of a general program of research on controls, an investigation has been made in the Langley 4- by 4-foot supersonic pressure tunnel to determine the important parameters in the design of controls for use on a 40° sweptback wing at supersonic speeds. The tabulated pressure data from these tests were presented in reference 1. The tests included six flap-type, one horn-balance, one tip-type, and six fixed-spoiler-type controls which were tested on a wing having 40° of sweep of the quarter-chord line, an aspect ratio of 3.1, and a taper ratio of 0.4.

The purpose of this report is to present an analysis of the pressure distributions obtained on the eight movable-control configurations. The wing angle-of-attack range for these tests was from -15° to 15° and the maximum control-deflection range, relative to the wing, was from -60° to 60° . The tests were conducted at Mach numbers of 1.61 and 2.01 for Reynolds numbers of 1.7×10^6 and 3.6×10^6 , based on the mean aerodynamic chord of 11.72 inches.

SYMBOLS

$b/2$	wing semispan
c	wing chord
C_p	pressure coefficient, $\frac{p_l - p}{q}$
$C_{p,r}$	resultant-pressure coefficient (lower surface C_p minus upper surface C_p)
M	stream Mach number
p	stream static pressure
p_l	local wing-surface static pressure
q	stream dynamic pressure
R	Reynolds number based on wing mean aerodynamic chord
x	distance from wing leading edge in chordwise direction
y	distance from wing root in spanwise direction

- α wing angle of attack, deg
- δ control deflection relative to wing (positive when control trailing edge is deflected down), deg
- Δ prefix indicating change due to α or δ

APPARATUS

Wind Tunnel

This investigation was conducted in the Langley 4- by 4-foot supersonic pressure tunnel, which is a rectangular, closed-throat, single-return type of wind tunnel with provisions for the control of the pressure, temperature, and humidity of the enclosed air. Flexible-nozzle walls were adjusted to give the desired test-section Mach numbers of 1.61 and 2.01. During the tests, the dewpoint was kept below -20° F so that the effects of water condensation in the supersonic nozzle were negligible.

Model and Model Mounting

The model used in this investigation consisted of a swept wing having interchangeable controls and various associated control adapters (or replacement sections) required to fit the controls to the basic wing component. The control configurations are presented in figure 1, with the movable controls denoted by shaded areas. The eight basic configurations are identified as configurations 1 to 7 and configuration 9. The location of the pressure orifices for all of the configurations can be determined from table 1, and the spanwise stations are shown in figure 2.

The basic wing was swept back at 40° along the 25-percent-chord line and had a root chord of 15.88 inches, a tip chord of 6.17 inches, a semi-span of 17.02 inches, an aspect ratio of 3.1, and a taper ratio of 0.4. The wing section had a thickness of 5 percent chord and was made up of a round-leading-edge NACA 65-series section extending from the leading edge to the 40-percent-chord line, a flat midsection (0.79 inch thick at the root and 0.31 inch thick at the tip) extending to the 75-percent-chord line, and a wedge-shaped trailing edge. Configuration 2 had a blunt trailing edge as shown in figure 1(a). All of the trailing-edge controls had a chord of 27.5 percent of the wing chord. The hinge line on configuration 4 was along the 81.25-percent-wing-chord line; on configuration 5 it was along the 87.5-percent-chord line; and on configuration 9 it was along the 50-percent-chord line. On all other configurations the hinge line was at the 75-percent-chord line.

The basic wing and controls were constructed of steel with the pressure tubes installed in grooves in the upper surface and faired over with plastic.

The semispan wing was mounted horizontally in the tunnel from a turntable in a steel boundary-layer bypass plate which was located vertically in the test section about 10 inches from the sidewall. Photographs of two of the configurations, mounted for testing, are shown in figure 3.

TESTS

The turntable in the bypass plate, on which the wing was mounted, was rotated to change the model angle of attack. (See fig. 3.) Since the angular deflection of the wing under load was negligible, the angle of attack was measured with a vernier on the outside of the tunnel. Control-surface deflection was changed by means of a gear mechanism which rotates the strain-gage balance, the torque tube, and the control as a unit. The control deflections were set with the aid of a slide-wire control-position indicator mounted on the torque tube near the wing root and were checked under load with a cathetometer mounted outside the tunnel. The pressure distributions were determined from photographs of multitube manometer boards to which the leads from the model orifices were attached.

Because structural limitations made it impossible to get sufficient pressure tubes through the torque tube to instrument both surfaces of the model, orifices were installed on one surface only. Due to this limitation the models were tested at positive and negative angles of attack over the control-deflection range.

Configurations 1 to 9 were tested over a control-deflection range from -30° to 30° for angles of attack from -15° to 15° . Additional tests were made on configuration 1 over a control-deflection range from -60° to 60° at angles of attack of 0° , $\pm 6^\circ$, and $\pm 12^\circ$. The angles mentioned here are in some cases only nominal. The actual values, corrected for deflection under load, are given in the tables of reference 1.

Most of the tests were made at a tunnel stagnation pressure of 13 lb/sq in. abs at $M = 1.61$ and 15 lb/sq in. abs at $M = 2.01$, corresponding to a Reynolds number of 3.6×10^6 based on the mean aerodynamic chord of 11.72 inches. Additional tests were made on configurations 1 and 2 at $R = 1.7 \times 10^6$ at $M = 1.61$. In order to insure a turbulent boundary layer over the model, 1/4-inch-wide strips of No. 60

carborundum grains were attached to both the upper and lower surfaces a short distance back from the leading edge. These strips completely spanned the model except within 1/4 inch of the orifice stations.

PRECISION OF DATA

The mean Mach numbers in the region occupied by the model are estimated from calibrations to be 1.61 and 2.01 with local variations being smaller than ± 0.02 . There is no evidence of any significant flow angularities. The estimated accuracies in setting the wing angle of attack and control deflection are $\pm 0.05^\circ$ and $\pm 0.1^\circ$, respectively. The measured pressure coefficients are believed to be accurate within ± 0.01 .

RESULTS

The pressure-distribution results of this investigation are presented in three sections. The first section includes the basic-wing chordwise pressure distributions and selected pressure distributions and pressure-coefficient contours for some of the configurations with deflected controls. These results are presented in figures 4 to 12.

In the second section, comparisons are made between some of the experimental results and the linear-theory predictions by plotting the incremental surface-pressure coefficients and the incremental resultant-pressure coefficients due to control deflection or angle of attack, normalized by the respective angles. These plots are presented for configurations 1 and 3 in figures 13 to 20.

In the third section, experimental comparisons are presented to demonstrate the effect of configuration changes on the surface-pressure distributions. These comparisons, which are presented in figures 21 to 24, show the upper-surface pressure distributions at the most significant stations for a limited number of angular conditions. Both positive and negative angles of attack and control deflections are shown, so that the changes on both high- and low-pressure surfaces of the model can be seen.

Although data were obtained at Mach numbers of 1.61 and 2.01, the analysis presented herein will be limited to $M = 1.61$. Comparison of the pressure distributions at the two Mach numbers indicated that the change in pressure coefficient was inversely proportional to the change in $\sqrt{M^2 - 1}$, as previously shown in reference 3, except for minor variations in the magnitude and extent of local disturbances.



DISCUSSION

Basic Pressure Distributions

Wing.- Consider first the pressure distributions over configuration 1 with a control deflection of 0° . The curves are presented over the complete wing span at angles of attack from -15° to 15° in figure 4. From the discontinuities in pressure distribution near the hinge line it is readily apparent that the full-span control was not satisfactorily hinged to the wing proper and the bending in the control resulted in abrupt pressure changes near the hinge line at many of the angles of attack. This control was hinged to the wing near the root and tip only, and the resulting bowing of the control was observed during the testing. The pressures over the control indicate that there was little, if any, interchange of air from the lower-wing surface despite the enlarged hinge-line gap.

L
3
7
0

In order to get a more accurate picture of the pressure distributions over the basic wing, the pressure distributions for the solid portions of configurations 3 and 6 are presented in figure 5. At $\alpha = 0^\circ$, the pressure distributions show that the airfoil section (which has rounded-leading edge, flat midsection, wedge-trailing edge) causes a rapid acceleration of the air from the leading-edge stagnation point to a relatively constant pressure equal to the free-stream value ($C_p = 0$). At the wing surface discontinuity where the trailing-edge wedge begins ($x/c = 0.75$), an expansion occurs, as would be expected. There is very little change in pressure distribution across the span of the wing.

As the angle of attack is increased from 0° to 15° the pressure distributions flatten out as the pressures approach a vacuum ($C_p = -0.55$ at $M = 1.61$). The lowest pressures are obtained at station 7, probably as a result of the buildup of a tip vortex. This wing-tip effect is discussed in more detail in reference 3. Near the wing trailing edge (fig. 5) a compression occurs at most of the stations due to separation ahead of the trailing-edge shock. A somewhat unusual phenomenon is the occurrence of a pressure increase at station 3 near $x/c = 0.50$ and at station 2 near $x/c = 0.25$ for angles of attack from 9° to 15° . This indicates a weak shock similar to the one previously noted at this Mach number on a more highly swept wing in reference 2. The shock therein was attributed to a component of flow normal to the wing leading edge which required an oblique shock to realine the flow with the main stream.

The plots of figure 5 also show that for negative angles of attack (corresponding to the high-pressure side of the wing), the pressure increases regularly with increasing negative angle of attack at all stations except for station 7. The strong relieving effect of the wing tip



is there evident, and the upper-surface tip vortex is so strong that it causes negative pressures on the lower surface near the trailing edge.

Deflected controls.- In order to examine the general effect of deflecting a trailing-edge control on this wing, upper-surface pressure distributions are presented in figure 6 for the full-span trailing-edge control having a sharp trailing edge (conf. 1) at three angles of attack for all of the test control deflections from -20° to 20° . The similarity of the pressure distributions at stations 3 and 5 shows that the flow over the center portion of the span is essentially two dimensional. This two-dimensional flow at combined angle of attack and control deflection is comparable to the results previously found on a similar, but unswept wing in reference 3. At low values of δ (10° or less), the chordwise distributions over the control retain the shape exhibited in the undeflected condition while the pressures increased or decreased due to negative or positive deflections, respectively. As the control is deflected to 20° , no unusual changes occur, the pressures decreasing regularly. At a control deflection of 20° , however, the pressure rise at the hinge line becomes too large for the flow to stay attached and shock detachment or flow separation occurs ahead of the hinge line such as was previously observed in references 3 to 5 for unswept controls on a straight and on a delta wing. On the control surface at $\delta = -20^\circ$, the pressures exhibit a peak pressure point followed by an expansion toward the trailing edge. This phenomenon was described in detail in reference 3 and is attributable to the fact that the flow becomes subsonic and must therefore accelerate to a sonic point at the trailing edge.

As the angle of attack is increased from -12° to 12° (fig. 6) the change in pressure coefficient with change in control deflection decreases. This is due to the increase in local Mach number ahead of the control and the fact that the pressures are approaching a vacuum. The separation ahead of the trailing-edge shock, previously discussed for the basic wing, tends to increase as the control deflection is increased.

At $\alpha = 0^\circ$, the pressures are fairly constant across the span of the wing. At $\alpha = -12^\circ$, considerable decrease in pressure occurs at station 7 due to the relieving effect of the wing tip. When the angle of attack is increased to 12° a gradual decrease in pressure across the span is evident and the tip vortex completely eliminates any effect of control deflection at station 7.

This discussion on the pressure distributions for the full-span control has shown that for control deflections from -10° to 20° the pressure changes were confined in chordwise extent to the control surface and were very regular. Since these characteristics are generally true for the remaining controls, pressure distributions are presented in figures 8 to 11 for several of the controls, at control deflections of -20° , 0° , and 20° , only. The pressure distributions on the inboard

trailing-edge control (fig. 7) show similar effects due to control deflection to those just discussed on the full-span control. In addition, however, at station 4 a loss in loading occurs for negative control deflection due to the proximity of the parting line. On the wing outboard of the control, there appears to be little if any carryover except for the angular condition at which the hinge-line separation is known to be most severe ($\alpha = -12^\circ$, $\delta = -20^\circ$).

For the outboard trailing-edge control (fig. 8), the pressure distributions over the control are again very similar to the distributions over the full-span control. The hinge-line separation seems considerably reduced (station 7, fig. 8(a)); however, this is due in part to the reduced control deflections for this control. The loss in pressure at station 24 as compared to that at station 5 is again attributed to a parting line effect and is expected. The carryover of pressures due to control deflection inboard of the control is practically nonexistent.

The pressure distributions due to deflecting the horn-balance control (fig. 9) are essentially identical to those for configuration 6 at the orifice stations 1 to 6. At station 7, however, the unporting of the control at the parting line causes large gradients in the pressure distributions due to the cross flows characteristic of tip-type controls having long parting lines. (See ref. 4.) On the overhang portion of the control (fig. 9), the pressure distributions are erratic, particularly at the negative control deflections due to the strong crossflows in this region and the low aspect ratio of this portion of the control. At station 10, when the control is undeflected, the pressure distributions are similar to those at station 7 for the basic wing.

The pressure distributions for the tip-control configuration (fig. 10) show that the tip-control effect does not extend inboard even as far as station 6. At station 7 the large pressure gradients due to unporting the control are again evident; however, the differences from the pressure distributions described on configuration 7 demonstrate the effects of the different hinge-line location and the lack of deflection of the wing downstream of $x/c = 0.75$. On the control the distributions are markedly like the distributions on the corresponding stations for configuration 7 despite the changes in hinge-line location and plan form.

Pressure contours.— Although it is questionable whether control deflections greater than 30° are of practical importance in this speed range, some tests were made of configuration 1 with the controls deflected to approximately 60° . In figure 11, pressure contours are shown for configuration 1 throughout the negative control-deflection range at angles of attack of -12° , 0° , and 12° . At $\alpha = 12^\circ$, lack of data for station 7 at this reduced Reynolds number (1.7×10^6) restricts the spanwise extent of the pressure contours.

The most severe hinge-line separation or shock detachment condition occurs at $\alpha = -12^\circ$ (fig. 11(a)). At $\delta = -20^\circ$ a shock can be noticed originating near the hinge line at the wing root and angling somewhat ahead of the hinge line across the wing span. As the negative control deflection is gradually increased to -60° , the shock increases in intensity, becomes perpendicular to the wing root, and moves continuously forward. The maximum pressures on the control first occur quite far outboard but then gradually move inboard. Meanwhile the pressures at the wing tip are relatively constant. As the angle of attack is increased from -12° to 12° (fig. 11) the effect of the control deflection on the wing pressures is delayed to larger control deflections. At $\alpha = 12^\circ$ the effect of the weak oblique shock emanating from near the wing apex is again evident.

In order to compare the hinge-line separation effects for the various control configurations, pressure contours are plotted in figure 12 for all of the partial-span controls at $\alpha = -12^\circ$ with the controls deflected to the maximum negative test angle. Comparison of the contour diagrams for configurations 3, 4, and 5 shows that, as the control hinge line is moved rearward, the separation ahead of the control decreases and the maximum pressure point on the control moves outboard. Configuration 6 exhibits little separation at $\delta = -20^\circ$; however, the pressure contour of configuration 7 indicates that separation on the outboard controls does occur when δ reaches -27° . The carryover effect of the overhanging portions of the controls on configurations 7 and 9 is restricted to a fairly narrow region at the wing tip. The low-aspect-ratio portions of these two controls also show the large dropoff in pressures away from the mid-span which was previously mentioned.

Theoretical Predictions

Application and limitations of theory.— The prediction of the wing surface pressures due to the wing section was not attempted because of the rounded-leading edge. It was also believed that the changes in pressure due to angle of attack and control deflection were of primary importance. In order to make theoretical predictions of the surface-pressure coefficients due to control deflection and/or angle of attack, the three-dimensional linear theory (e.g., ref. 6) was employed. This theoretical method makes several simplifying assumptions which should be considered before a detailed comparison of the experimental and theoretical results is made. First, the theory assumes that the angular deflections are small and that the effects due to control deflection and angle of attack can be superimposed. Within the range of the present tests, this means that at some conditions, linear theory predicts pressures lower than absolute vacuum. It also means that as the controls are deflected, sizeable openings will appear at the wing-control parting lines contrary to the theoretical assumption. Other simplifications of the linear theory are that the wing has no thickness and that viscous

effects will be nonexistent. As shown in the previous section, the flow over the model exhibits extensive regions of flow separation or shock detachment which can be expected to cause regions of disagreement between linear theory and experiment. Despite these shortcomings of the linear theory, it can be used to indicate trends and, in conditions where the linear-theory assumptions are approached, it can show the magnitudes of the pressure coefficients.

In the present report, theoretical computations were made for configurations 1 and 3, only, and at a Mach number of 1.61. Linear theory would not predict any change in pressures due to thickening the trailing edge (configuration 2) or due to moving the hinge line (configurations 4 and 5). The numerous reflections of the Mach lines on the low-aspect-ratio portions of configurations 7 and 9 make it extremely difficult to compute the linear-theory pressures for these configurations.

The theoretical calculations that were made, however, are presented in comparison with the corresponding experimental results in figures 13 to 16 for configuration 1 and figures 17 to 20 for configuration 3. First, the incremental pressure coefficients due to control deflection or angle of attack were computed. Then, by combining the pressure increments obtained at the proper angular conditions, the resultant-pressure coefficients were obtained as would be measured on the two surfaces of the wing, since the model was symmetrical.

Surface-pressure coefficients due to δ . In general, the pressures over the controls due to control deflection (figs. 13 and 17) show that at positive control deflections (the low-pressure side of the control) the experimental pressures are considerably less than the theoretical predictions. At negative control deflections, however, the experimental values are equal or greater than theory at $\alpha = -12^\circ$, but then decrease as α is increased to 12° . Wherever control-deflection data of -30° are available, the increased pressures ahead of the hinge line due to viscous separation or shock detachment can be observed. Near the wing tip on configuration 1 (fig. 13) the predicted dropoff in loading from that at the inboard stations does not materialize. On the partial-span configuration 3 (fig. 17) the pressures at station 4 do show a dropoff at the negative control deflections due to the parting line, but the theoretical predictions are still poor. The carryover pressures at station 24 are usually much less than theory predicts and at $\delta = -30^\circ$ are sometimes reversed in sign due to the large effect of the control unporting.

Surface-pressure coefficients due to α . For a control deflection of 0° (figs. 14(c) and 18(c)), the theoretical predictions of the pressure coefficients due to angle of attack are fairly good except in two regions of the wing. In the region ahead of the Mach lines from the wing apex and wing tip, where two-dimensional pressures are predicted,

the experimental pressures are fairly constant across the span at a value below that predicted. In the tip region of the wing at positive angles of attack the experimental pressures are considerably in excess of theory due to the vortex formation previously described. The changes in pressures over the deflected controls (figs. 14 and 18) due to changing the angle of attack are generally less than theoretical for the positive control deflections and greater than theoretical for the negative control deflections.

Resultant-pressure coefficients due to δ .— The chordwise loadings due to control deflection, shown in figures 15 and 19, indicate that on the controls, the loadings are slightly greater than half the theoretical predictions. This is the result of the poor prediction of the pressure change on the low-pressure surface of the control and fairly good prediction on the high-pressure surface. Near the wing tip the decrease in theoretical loading makes the prediction appear more reasonable. At the largest control deflections, the separation ahead of the hinge line again causes large differences between theory and experiment in this region. At $\delta = 30^\circ$, the spanwise carryover of loading at station 24 (fig. 19) has been eliminated by the parting-line crossflow effects.

Resultant-pressure coefficients due to α .— The chordwise loadings due to angle of attack, shown in figures 16 and 20, indicate that the prediction of the loading is fairly good, although there is a large amount of scatter of the experimental data. Again the difference between the experimental and theoretical loading in the two-dimensional region ahead of the Mach lines and the higher-than-predicted loading near the wing tip are apparent.

Configuration Changes

Effect of trailing-edge thickness.— The change in pressure distributions due to increasing the trailing-edge thickness of the full-span control is shown in figure 21. Although it appears that the angle of attack was not set correctly for one of the configurations, the change due to trailing-edge thickness can still be ascertained. In general, the effect is to increase the pressures over the control and to increase the amount of flow separation or shock detachment ahead of the control. These changes are in agreement with the changes found owing to increasing the trailing-edge thickness on the unswept hinge-line controls of references 3 and 4. It was shown in reference 3 that the increased pressures were a result of the increased turning angle at the control hinge line and that the pressures could be predicted fairly accurately by shock-expansion theory.

Effect of reducing the control span.— A comparison of the pressure distributions at stations 2 to 4 for the full-span control with those

for the inboard half-span control is presented in figure 22. At stations 2 and 3 (and, although not shown, station 1) the pressure distributions for the two configurations are practically identical, except for some minor changes near the hinge line due to the bending in the control of configuration 1. At station 4, the control tip causes a decrease in pressure over the control near the trailing edge at negative control deflections. This effect was noted previously.

Effect of hinge-line movement.- On the inboard half-span controls, as the hinge line is moved rearward (hinge line is at $0.75c$ for configuration 3 and at $0.875c$ for configuration 5) changes in the pressure distributions occur as shown in figure 23. Ahead of the control ($x/c < 0.725$) pressure increases due to flow separation or shock detachment disappear at the negative control deflections but appear at the positive control deflections due to the leading edge of the control unporting above the wing surface. On the surface of the control ($0.725 \leq x/c \leq 1.00$) at positive control deflections there is relatively little change in the pressures as a result of moving the hinge line rearward. At the negative control deflections, however, the pressures on the control surface are altered considerably. Ahead of the hinge line on configuration 5 ($0.725 \leq x/c \leq 0.875$) the pressures are reduced from those observed on configuration 3. This trend is evident at all angles of attack and is apparently caused by two conflicting phenomena. The flow on the upper surface of the wing attempts to expand near the leading edge of the balanced control; however, the high-pressure air on the lower surface of the wing ahead of the control (due to the leading-edge unporting) bleeds through to the upper surface of the control and nullifies the expansion. After the hinge line, the pressures on configuration 5 are very similar to those on configuration 3 and would correspond even closer if plotted on the basis of the distance from the hinge line divided by the chord length from the hinge line to the trailing edge. Meanwhile, outboard of the controls (fig. 24) changes in pressure distribution occur with movement of the hinge line due to the change in separation condition from the negative control deflections to the positive control deflections as would be expected.

CONCLUSIONS

The results have been reported herein of an experimental and theoretical pressure investigation of eight controls on a 40° sweptback wing at a Mach number of 1.61. From the investigation, which covered a range of angles of attack from -15° to 15° and control deflections from -60° to 60° , the following primary conclusions may be reached:

Basic pressure distributions:

1. On the low-pressure surface of the basic wing at angles of attack from 9° to 15° a weak shock occurs, originating near the apex, probably as a result of the realignment of a component of the flow perpendicular to the leading edge.

2. At control deflections from -10° to 20° the pressure changes on the trailing-edge controls were limited in chordwise extent to the control surface and changed regularly with control deflection.

3. At negative control deflections of -20° and greater, separation or shock detachment occurred ahead of the hinge line and increased in chordwise extent with outboard movement along the span and with increasingly negative control deflections.

4. Erratic variations in pressure occur near the parting lines of the large horn-balance control or the tip control similar to the cross-flow effects previously found for tip controls on a delta wing.

Theoretical predictions:

1. For the trailing-edge flap-type controls, the experimental increments in surface pressure coefficient due to control deflection are generally in only fair or poor agreement with linear theory because of flow separations and possibly shock detachment. The pressure rise ahead of the control hinge line is not predicted by theory and the carryover at the parting line is smaller than predicted theoretically.

2. The experimental increments in surface pressure coefficient due to angle of attack were generally in good agreement with those predicted by linear theory for the basic wing except in the region ahead of the Mach lines from the wing apex and wing tip, and near the wing tip. The agreement tends to deteriorate as the control is deflected.

3. The experimental resultant pressure coefficients due to control deflection or angle of attack generally followed the theoretical trends for the trailing-edge controls but the values usually fell below the theoretical predictions.

Configuration changes:

1. The effect of increasing the trailing-edge thickness on the trailing-edge control is to increase the pressures on the control and to increase the flow separation or shock detachment ahead of the control.

2. As the hinge line is moved rearward on the inboard half-span trailing-edge control, the pressures on the high-pressure surface of the

10

1370

1

- 五

(a) Spanwise location of orifice stations

[illegible]

TABLE 1.- ORIFICE LOCATIONS - Continued

(b) Chordwise location of orifices on configurations 1 and 2

Orifice	Values of x/c at station:										
	1	2	3	4	24	5	6	7	8	9	10
1	0	0	0	0		0	0	0			
2	.050	.050	.050	.050		.050	.050	.050			
3	.100	.100	.100	.100		.100	.100	.100			
4	.150	.150	.150	.150		.150	.150	.150			
5	.200	.200	.200	.200		.200	.200	.200			
6	.250	.250	.250	.250		.250	.250	.250			
7	.300	.300	.300	.300		.300	.300	.300			
8	.350	.350	.350	.350		.350	.350	.350			
9	.400	.400	.400	.400		.400	.400	.400			
10	.450	.450		.450		.450	.450	.450			
11	.500	.500		.500		.500					
12	.550	.550		.550		.550	.550	.550			
13	.600	.600	.600	.600		.600	.600	.600			
14	.650	.650	.650	.650		.650	.650	.650			
15	.700	.700	.700	.700		.700	.700	.700			
16	.725	.725	.725	.725		.725	.725	.725			
17		.725	.725	.725		.725	.725	.725			
18		.750	.750	.750		.750	.750	.750			
19	.80	.80	.80	.80		.80	.80	.80			
20	.85	.85	.85	.85		.85	.85	.85			
21	.90	.90	.90	.90		.90	.90	.90			
22	.98	.98	.98	.98		.98	.98	.98			

TABLE 1.- ORIFICE LOCATIONS - Continued

(c) Chordwise location of orifices on configuration 3

Orifice	Values of x/c at station:										
	1	2	3	4	24	5	6	7	8	9	10
1	0	0	0	0		0	0	0			
2	.050	.050	.050	.050		.050	.050	.050			
3	.100	.100	.100	.100		.100	.100	.100			
4	.150	.150	.150	.150		.150	.150	.150			
5	.200	.200	.200	.200		.200	.200	.200			
6	.250	.250	.250	.250		.250	.250	.250			
7	.300	.300	.300	.300		.300	.300	.300			
8	.350	.350	.350	.350		.350	.350	.350			
9	.400	.400	.400	.400		.400	.400	.400			
10	.450	.450		.450		.450	.450	.450			
11	.500	.500		.500		.500					
12	.550	.550		.550		.550	.550	.550			
13	.600	.600	.600	.600		.600	.600	.600			
14	.650	.650	.650	.650		.650	.650	.650			
15	.700	.700	.700	.700		.700	.700	.700			
16	.725	.725	.725	.725		.725	.725	.725			
17		.725	.725	.725							
18		.750	.750	.750		.750	.750	.750			
19	.800	.800	.800	.800	0.800	.800	.800	.800			
20	.850	.850	.850	.850	.850	.850	.850	.850			
21	.900	.900	.900	.900	.900	.900	.900	.900			
22	.980	.980	.980	.980	.980	.980	.980	.980			

TABLE 1.- ORIFICE LOCATIONS - Continued

(d) Chordwise location of orifices on configurations 4 and 5

Orifice	Values of x/c at station:										
	1	2	3	4	24	5	6	7	8	9	10
1	0	0	0	0		0	0	0			
2	.050	.050	.050	.050		.050	.050	.050			
3	.100	.100	.100	.100		.100	.100	.100			
4	.150	.150	.150	.150		.150	.150	.150			
5	.200	.200	.200	.200		.200	.200	.200			
6	.250	.250	.250	.250		.250	.250	.250			
7	.300	.300	.300	.300		.300	.300	.300			
8	.350	.350	.350	.350		.350	.350	.350			
9	.400	.400	.400	.400		.400	.400	.400			
10	.450	.450		.450		.450	.450	.450			
11	.500	.500		.500		.500					
12	.550	.550		.550		.550	.550	.550			
13	.600	.600	.600	.600		.600	.600	.600			
14	.650	.650	.650	.650		.650	.650	.650			
15	.700	.700	.700	.700		.700	.700	.700			
16	.725	.725	.725	.725		.725	.725	.725			
17	.725	.725	.725	.725							
18	.750	.750	.750	.750		.750	.750	.750			
19	.800	.800	.800	.800	0.800	.800	.800	.800			
20	.850	.850	.850	.850	.850	.850	.850	.850			
21	.900	.900	.900	.900	.900	.900	.900	.900			
22	.980	.980	.980	.980	.980	.980	.980	.980			

TABLE 1.- ORIFICE LOCATIONS - Continued

(e) Chordwise location of orifices on configuration 6

Orifice	Values of x/c at station:										
	1	2	3	4	24	5	6	7	8	9	10
1	0	0	0	0		0	0	0			
2	.050	.050	.050	.050		.050	.050	.050			
3	.100	.100	.100	.100		.100	.100	.100			
4	.150	.150	.150	.150		.150	.150	.150			
5	.200	.200	.200	.200		.200	.200	.200			
6	.250	.250	.250	.250		.250	.250	.250			
7	.300	.300	.300	.300		.300	.300	.300			
8	.350	.350	.350	.350		.350	.350	.350			
9	.400	.400	.400	.400		.400	.400	.400			
10	.450	.450		.450		.450	.450	.450			
11	.500	.500		.500		.500					
12	.550	.550		.550		.550	.550	.550			
13	.600	.600	.600	.600		.600	.600	.600			
14	.650	.650	.650	.650		.650	.650	.650			
15	.700	.700	.700	.700		.700	.700	.700			
16	.725	.725	.725	.725		.725	.725	.725			
17											
18	.750	.750	.750	.750		.750	.750	.750			
19	.800	.800	.800	.800	0.800	.800	.800	.800			
20	.850	.850	.850	.850	.850	.850	.850	.850			
21	.900	.900	.900	.900	.900	.900	.900	.900			
22	.980	.980	.980	.980	.980	.980	.980	.980			

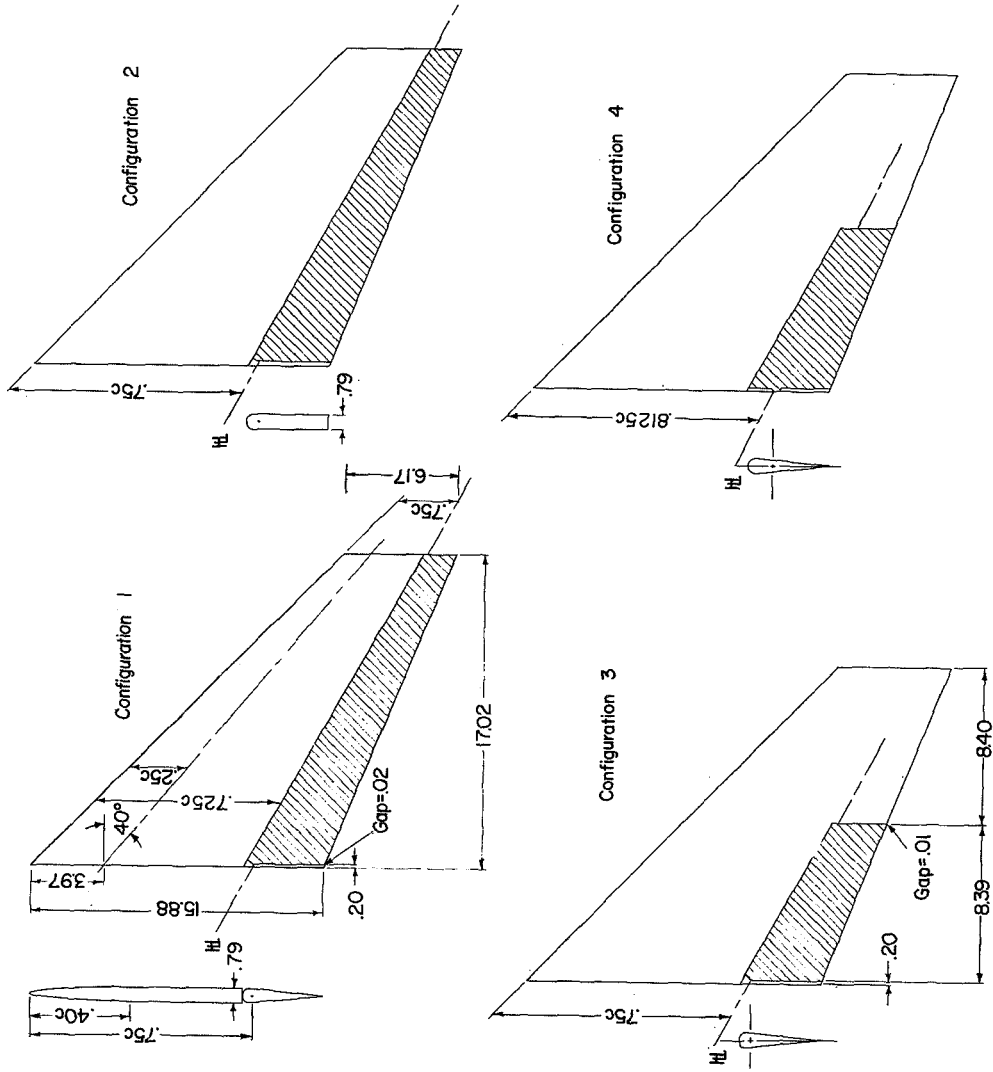
TABLE 1.- ORIFICE LOCATIONS - Continued

(f) Chordwise location of orifices on configuration 7

Orifice	Values of x/c at station:										
	1	2	3	4	24	5	6	7	8	9	10
1	0	0	0	0		0	0	0	0	0.110	0
2	.050	.050	.050	.050		.050	.050	.050	.100	.230	.130
3	.100	.100	.100	.100		.100	.100	.100	.200	.450	.260
4	.150	.150	.150	.150		.150	.150	.150	.400	.680	.520
5	.200	.200	.200	.200		.200	.200	.200	.610	.910	.790
6	.250	.250	.250	.250		.250	.250	.250	.810		.990
7	.300	.300	.300	.300		.300	.300	.300	.960		
8	.350	.350	.350	.350		.350	.350	.350			
9	.400	.400	.400	.400		.400	.400	.400			
10	.450	.450		.450		.450	.450	.450			
11	.500	.500		.500		.500					
12	.550	.550		.550		.550	.550	.550			
13	.600	.600	.600	.600		.600	.600	.600			
14	.650	.650	.650	.650		.650	.650	.650			
15	.700	.700	.700	.700		.700	.700	.700			
16	.725	.725	.725	.725		.725	.725	.725			
17						.725	.725	.725			
18	.750	.750	.750	.750		.750	.750	.750			
19	.800	.800	.800	.800		.800	.800	.800			
20	.850	.850	.850	.850		.850	.850	.850			
21	.900	.900	.900	.900		.900	.900	.900			
22	.980	.980	.980	.980		.980	.980	.980			

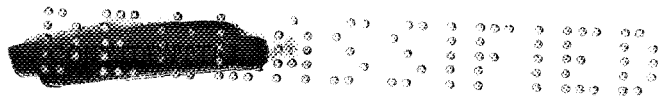
TABLE 1.- ORIFICE LOCATIONS - Concluded
(g) Chordwise location of orifices on configuration 9

Orifice	Values of x/c at station:										
	1	2	3	4	24	5	6	7	8	9	10
1	0	0	0	0		0	0	0	0	0	0
2	.050	.050	.050	.050		.050	.050	.050	.100	.200	.100
3	.100	.100	.100	.100		.100	.100	.100	.200	.400	.200
4	.150	.150	.150	.150		.150	.150	.150	.400	.600	.400
5	.200	.200	.200	.200		.200	.200	.200	.600	.800	.600
6	.250	.250	.250	.250		.250	.250	.250	.800	.950	.800
7	.300	.300	.300	.300		.300	.300	.300	.950		.950
8	.350	.350	.350	.350		.350	.350	.350			
9	.400	.400	.400	.400		.400	.400	.400			
10	.450	.450		.450		.450	.450	.450			
11	.500	.500		.500		.500		.550			
12	.550	.550		.550		.550	.550	.550			
13	.600	.600	.600	.600		.600	.600	.600			
14	.650	.650	.650	.650		.650	.650	.650			
15	.700	.700	.700	.700		.700	.700	.700			
16	.725	.725	.725	.725		.725	.725	.725			
17											
18	.750	.750	.750	.750		.750	.750	.750			
19	.800	.800	.800	.800		.800	.800	.800			
20	.850	.850	.850	.850		.850	.850	.850			
21	.900	.900	.900	.900		.900	.900	.900			
22	.980	.980	.980	.980		.980	.980	.980			

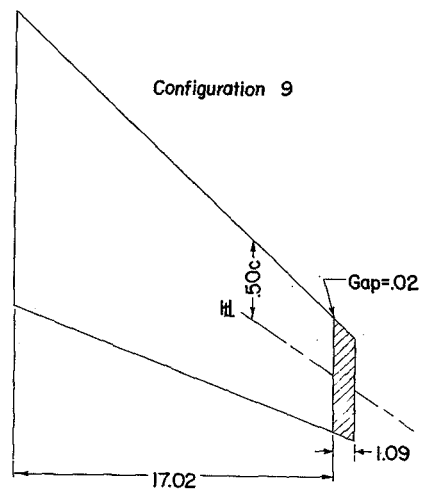
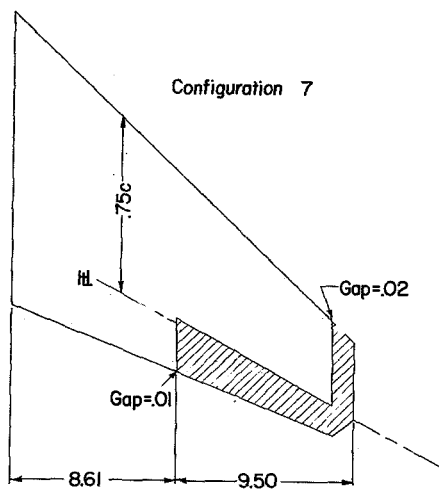
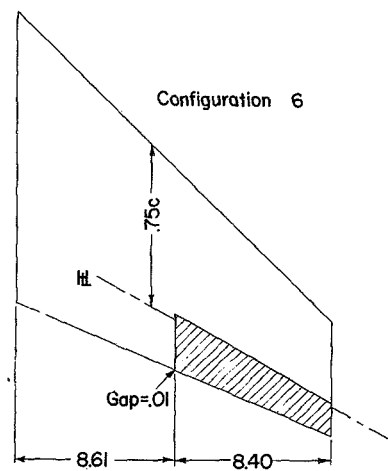
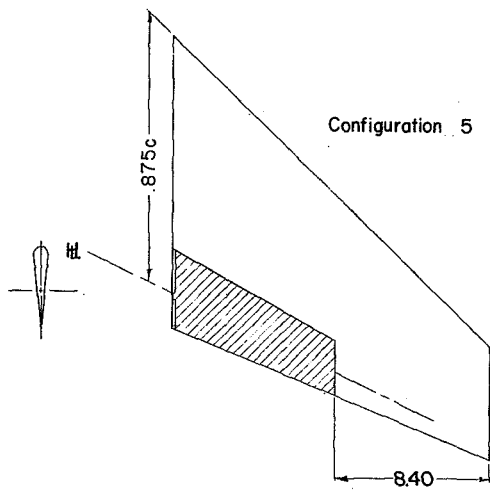


(a) Configurations 1 to 4.

Figure 1.- Sketches of the model configurations tested. (All dimensions in inches.)



L-370



(b) Configurations 5 to 9.

Figure 1.- Concluded.

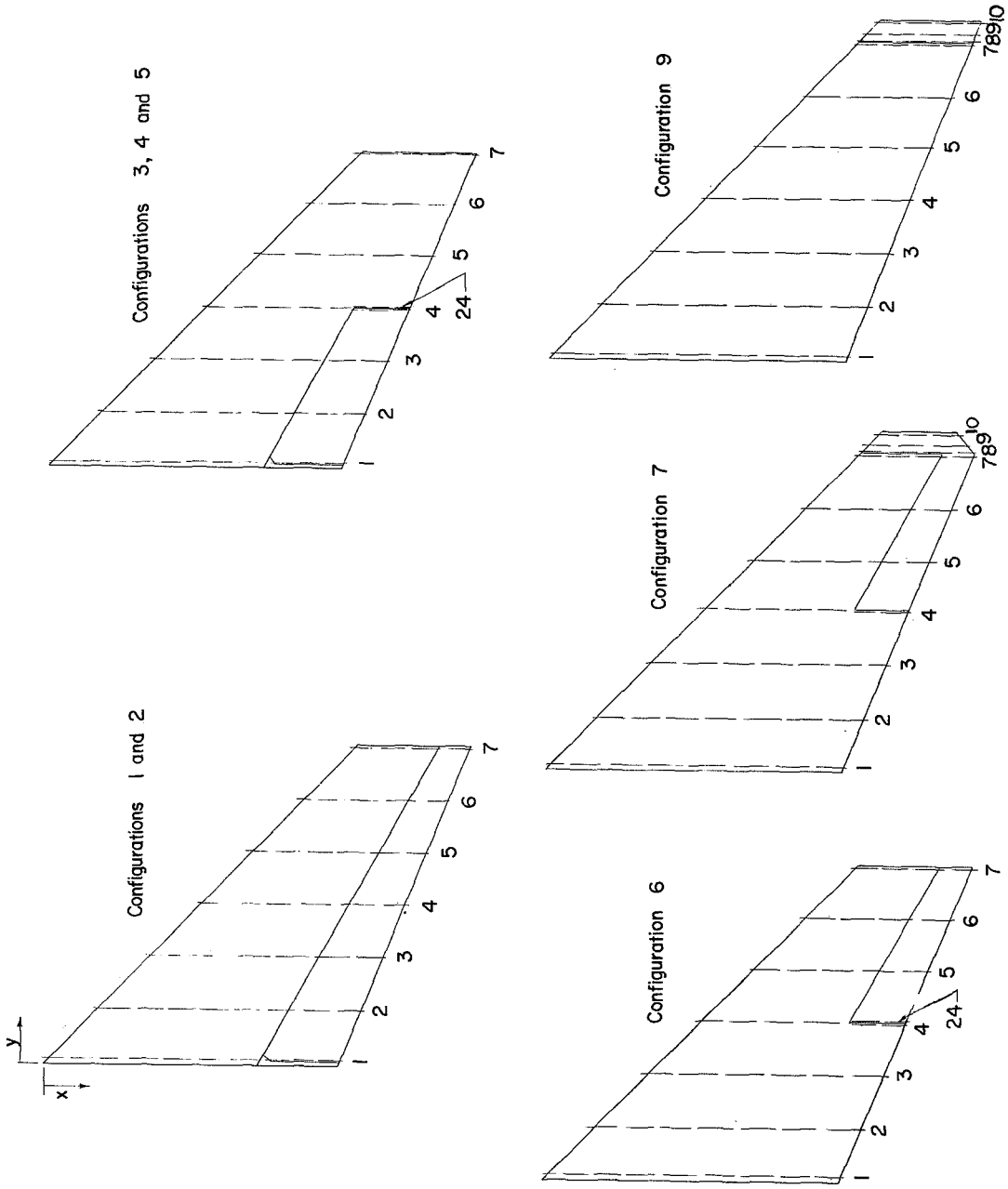
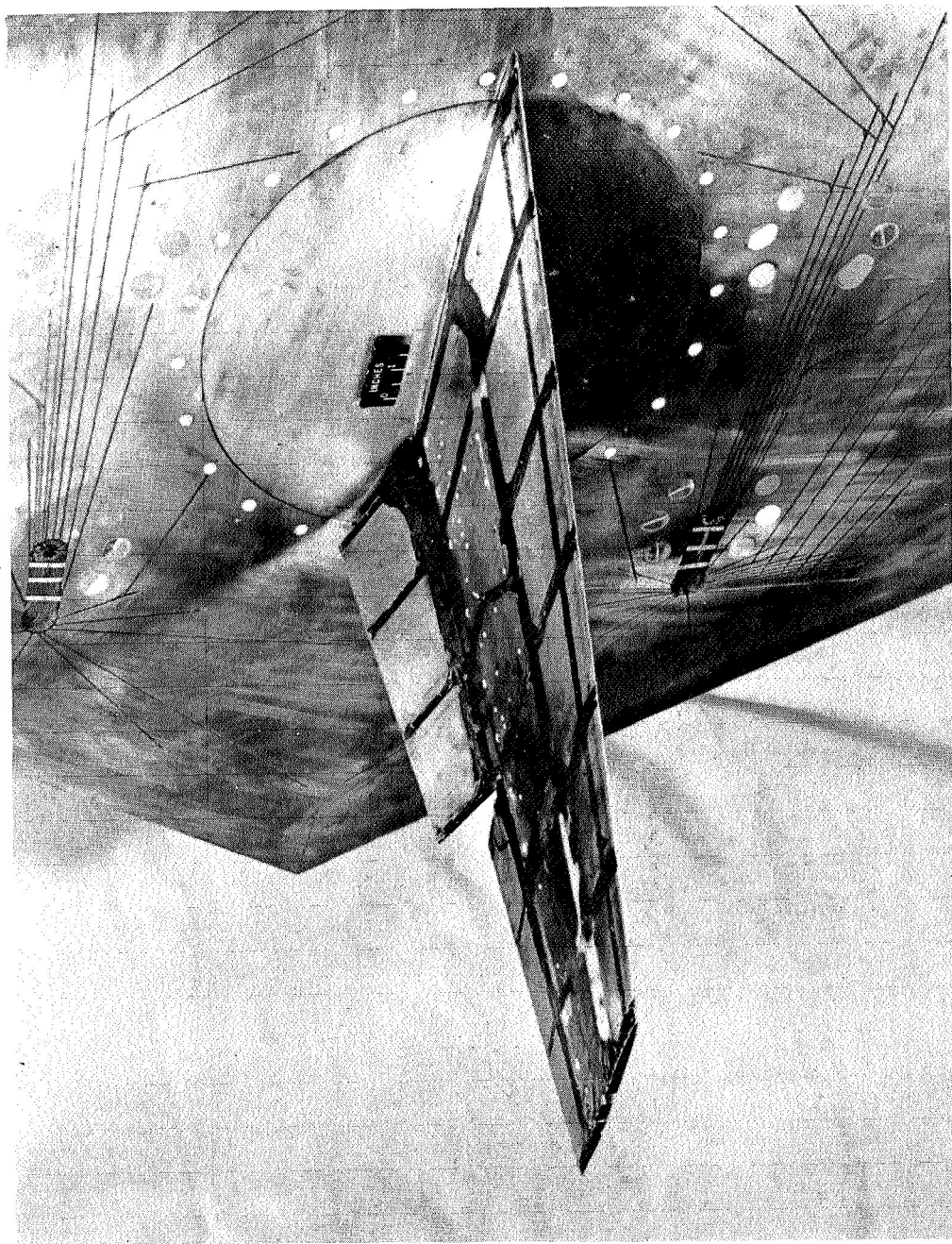


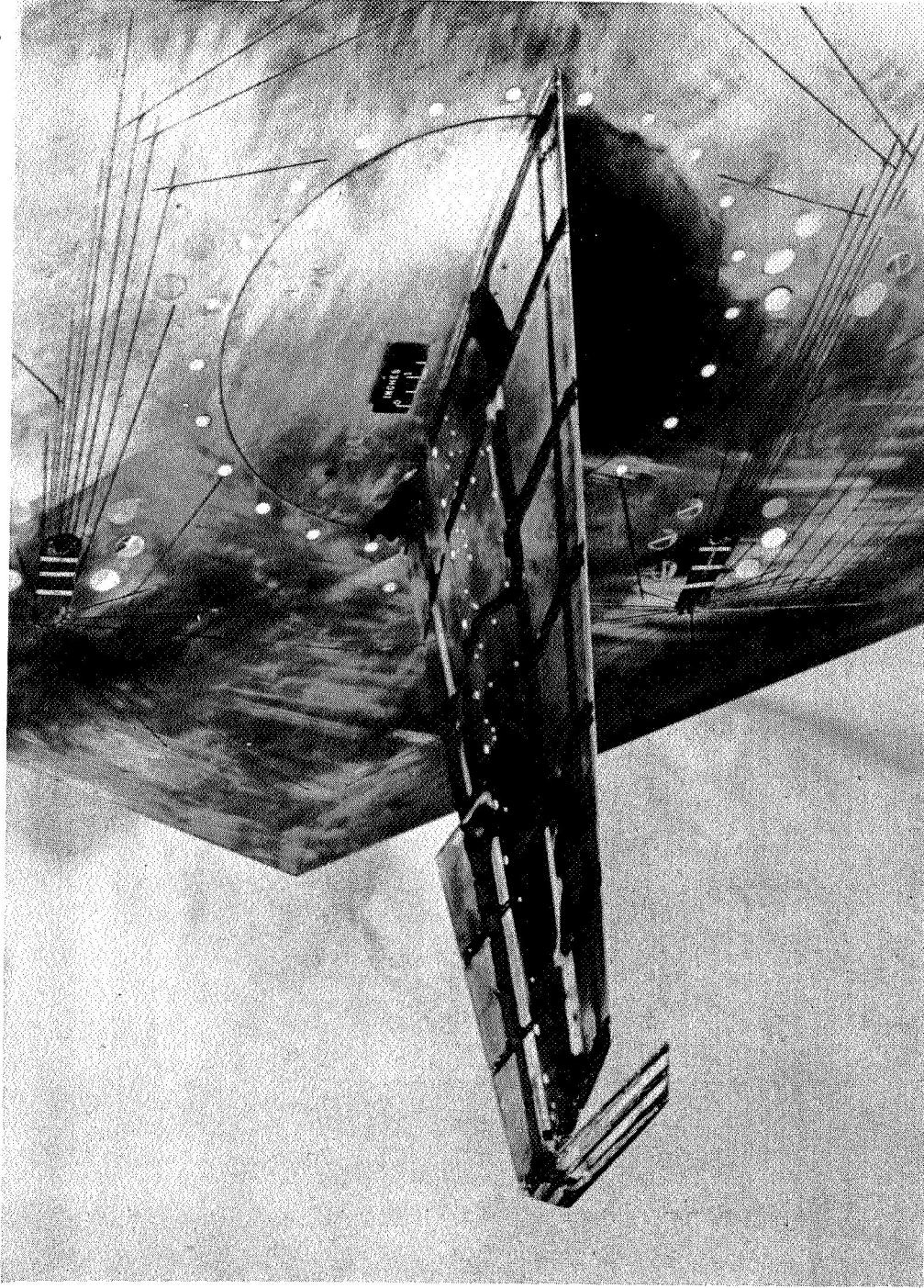
Figure 2.- Locations of the orifice stations.



(a) Configuration 3.

Figure 3.- Two of the movable-control configurations mounted on the bypass plate for testing.

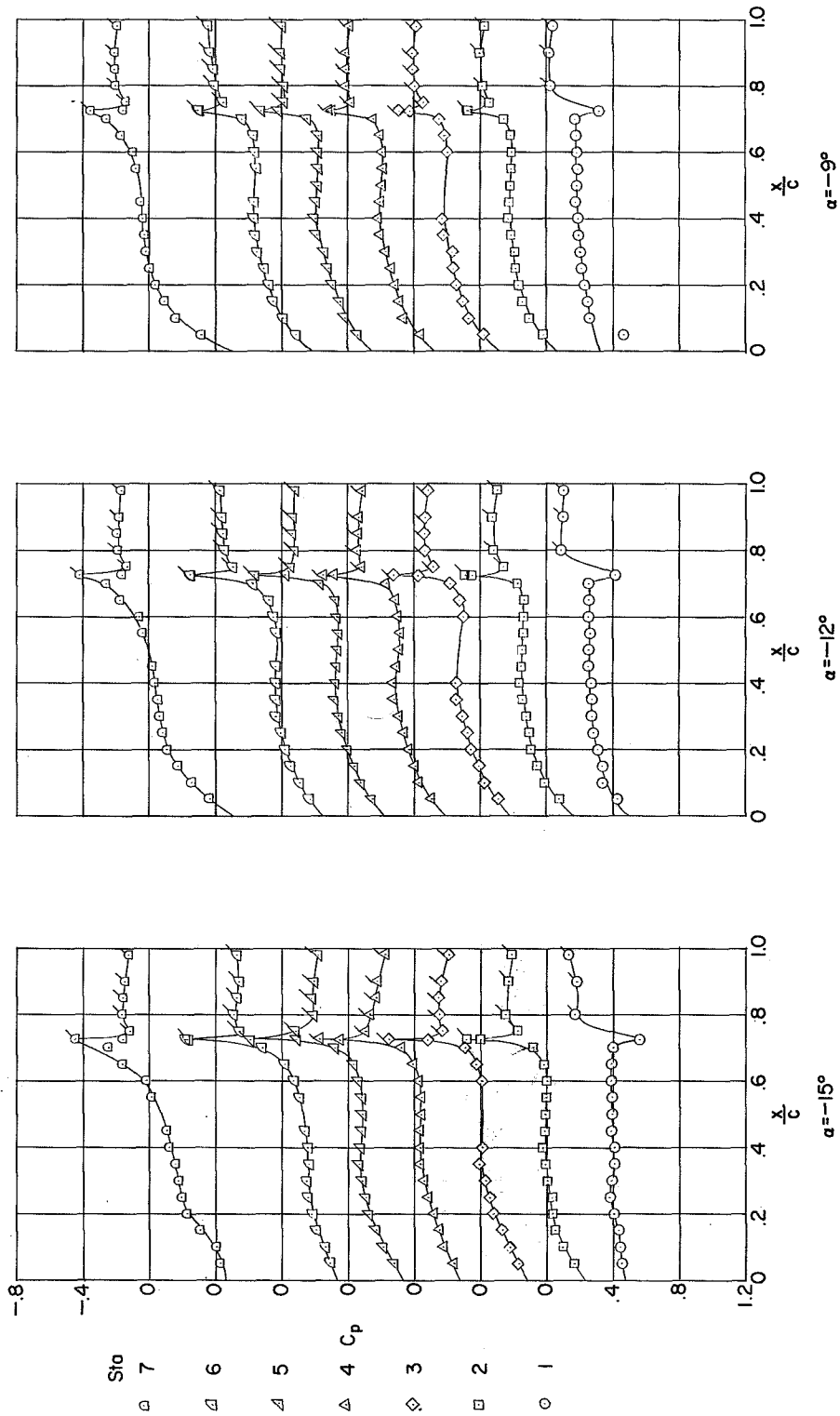
L-91657



(b) Configuration 7.

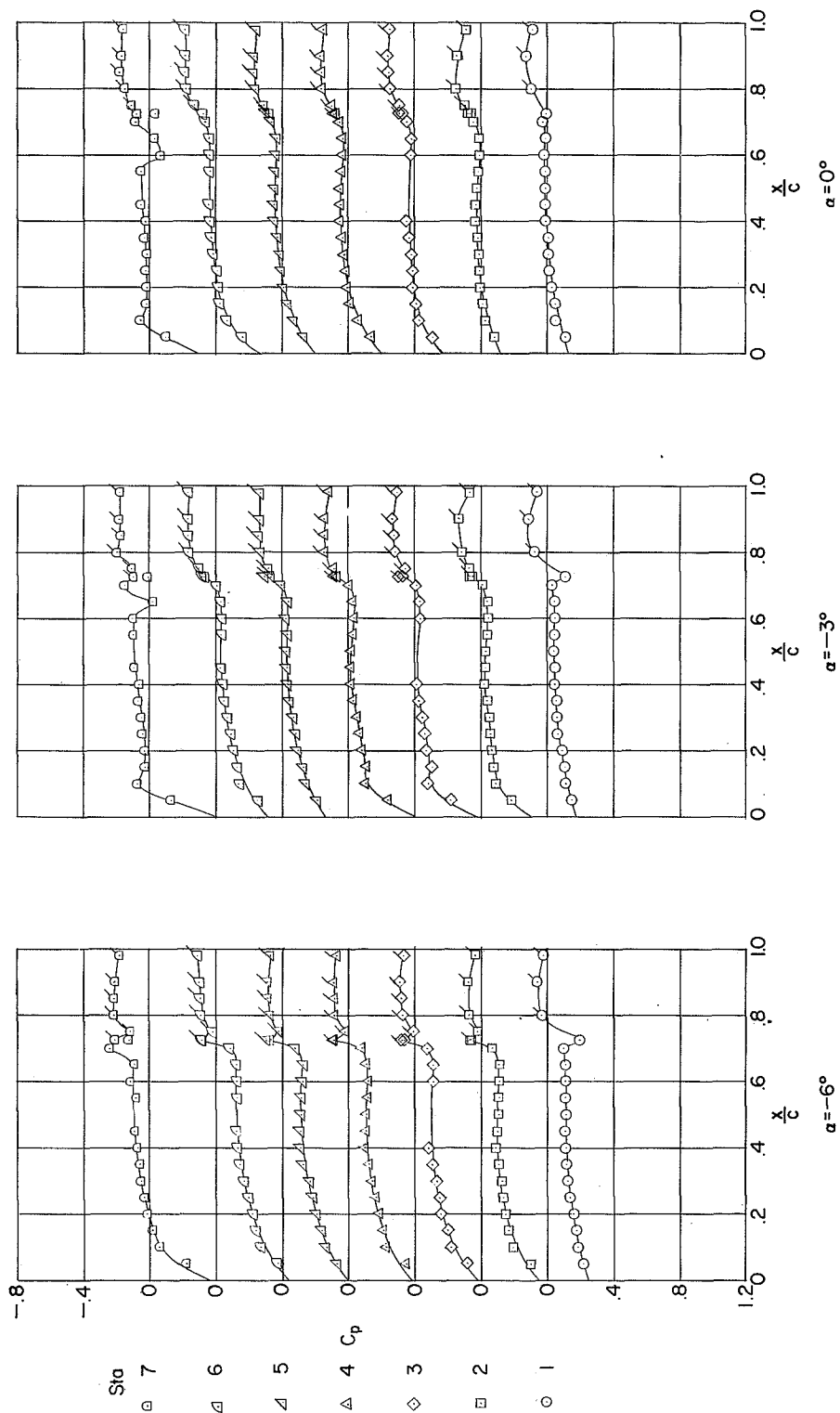
Figure 3.- Concluded.

L-91654



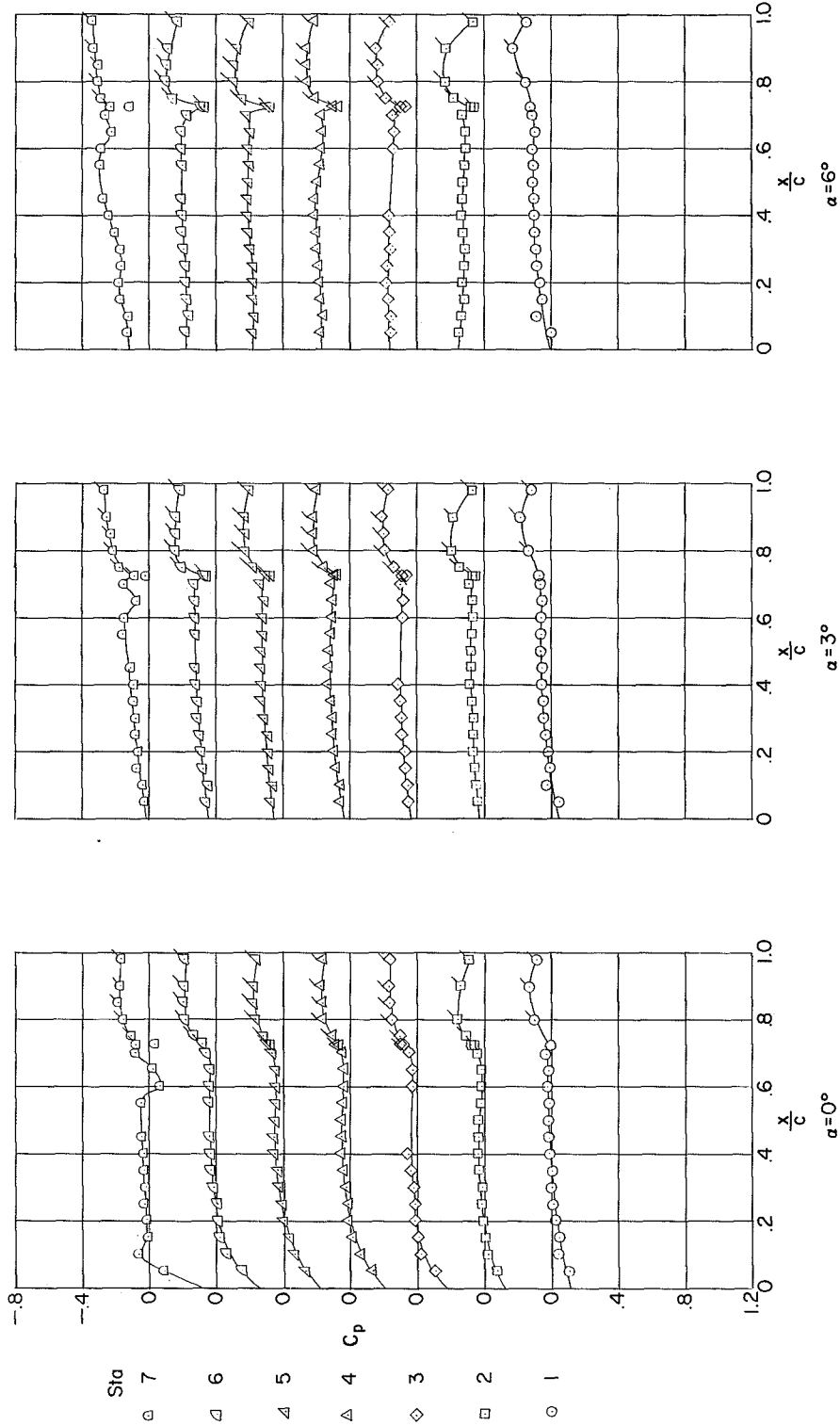
(a) $\alpha = -15^\circ$ to -9° .

Figure 4.- Upper-surface chordwise pressure distributions for configuration 1 with the control undeflected. Flagged symbols indicate orifices on control. $M = 1.61$; $R = 3.6 \times 10^6$.



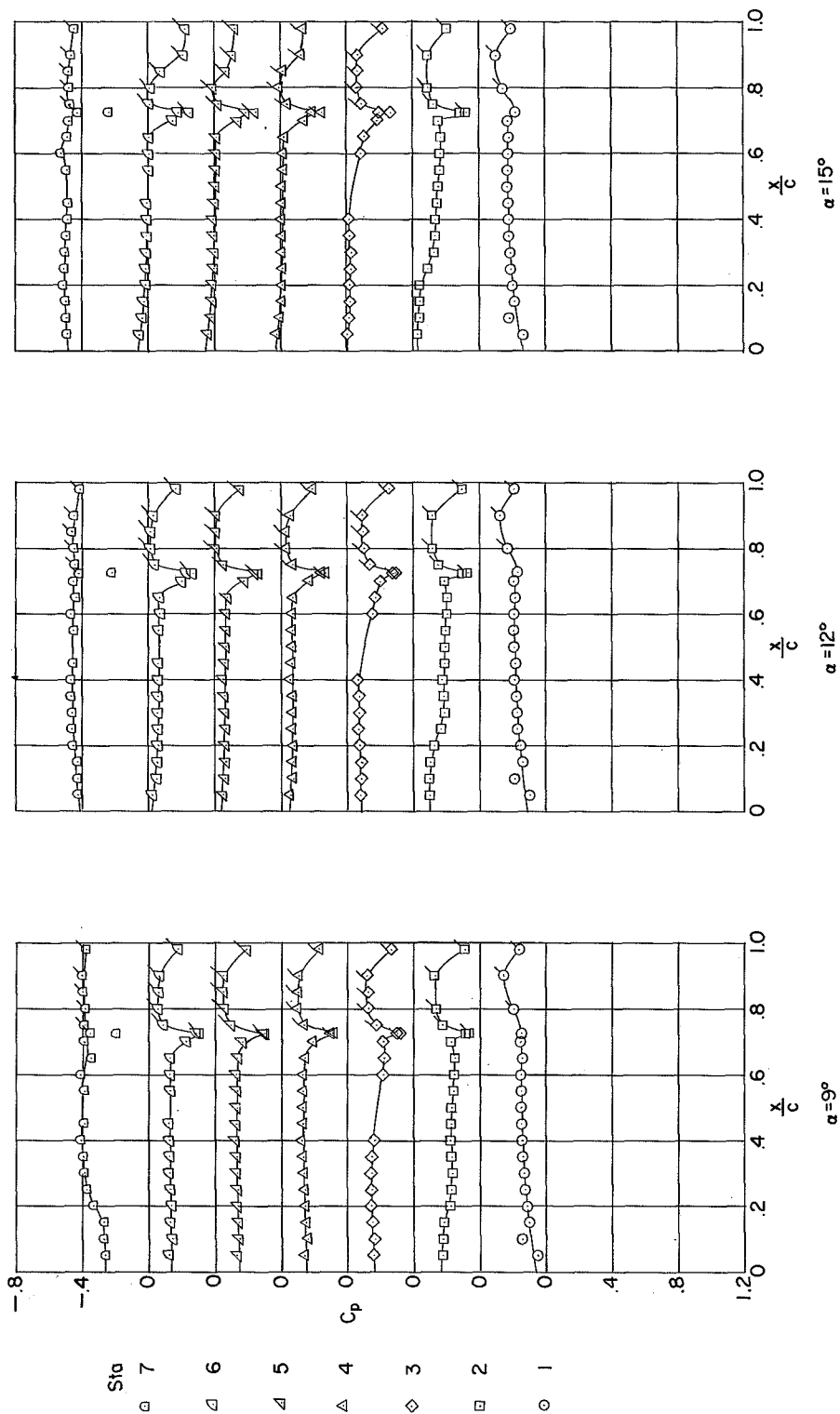
(b) $\alpha = -6^\circ$ to 0° .

Figure 4.- Continued.



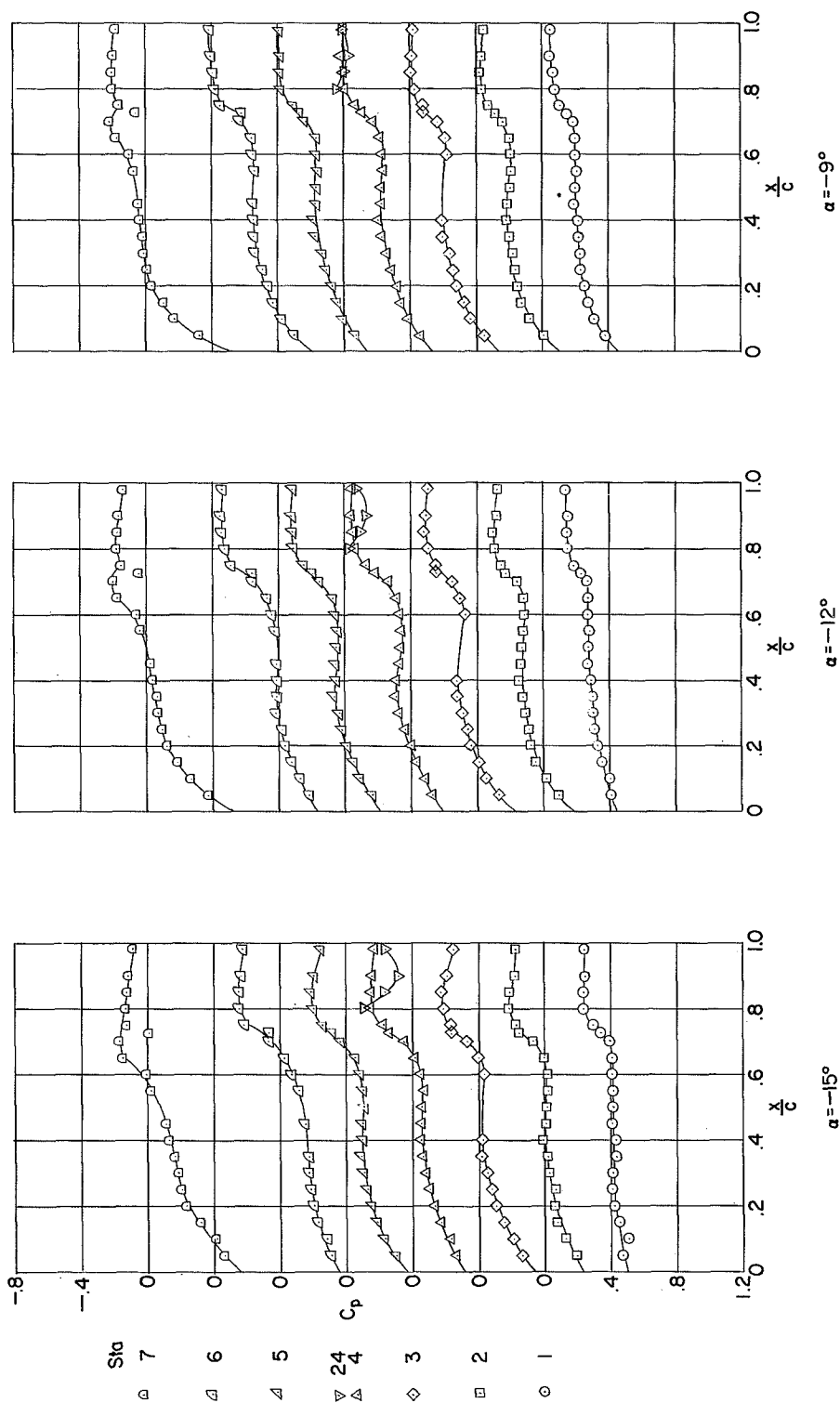
(c) $\alpha = 0^\circ$ to 6° .

Figure 4.- Continued.



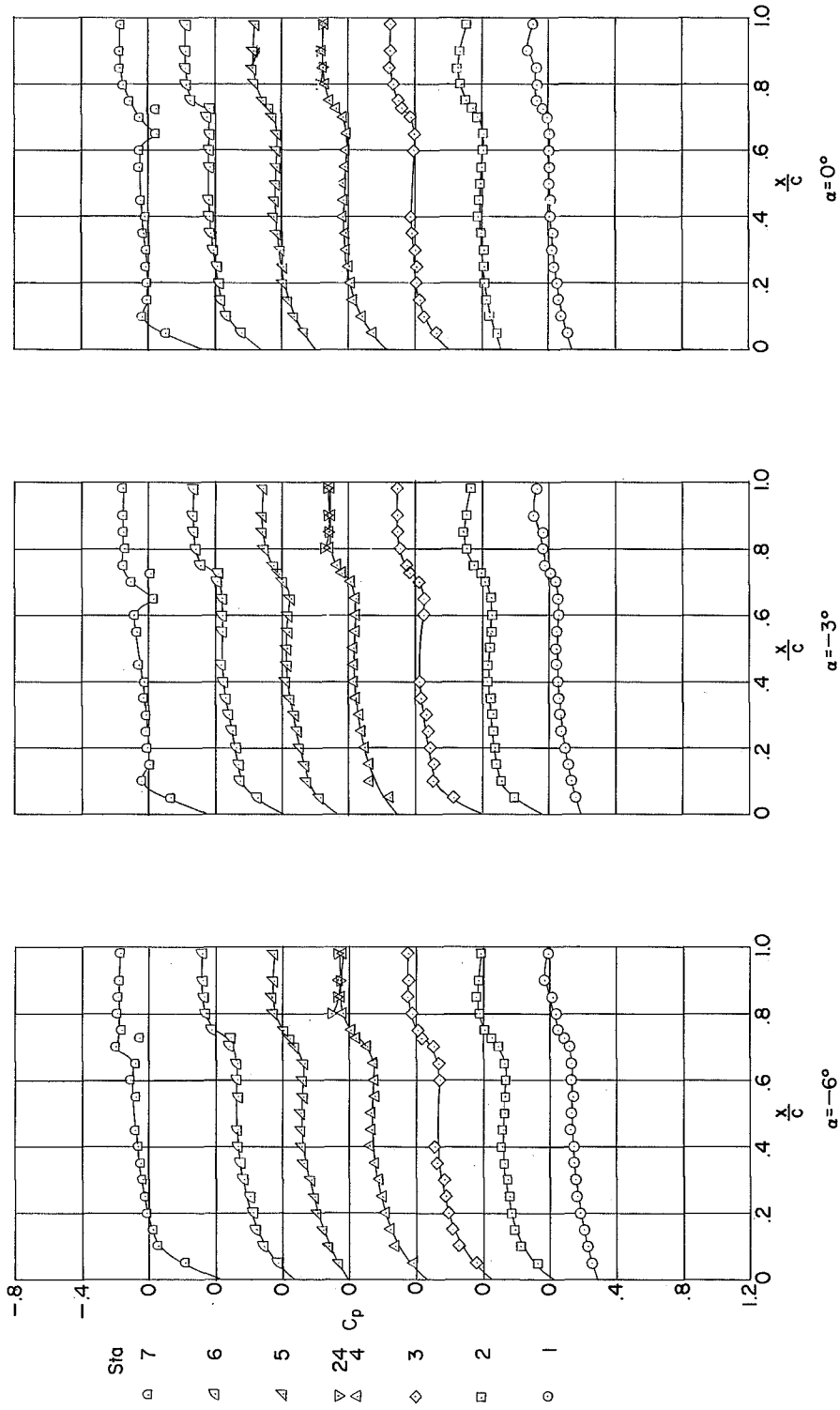
(d) $\alpha = 9^\circ$ to 15° .

Figure 4.- Concluded.



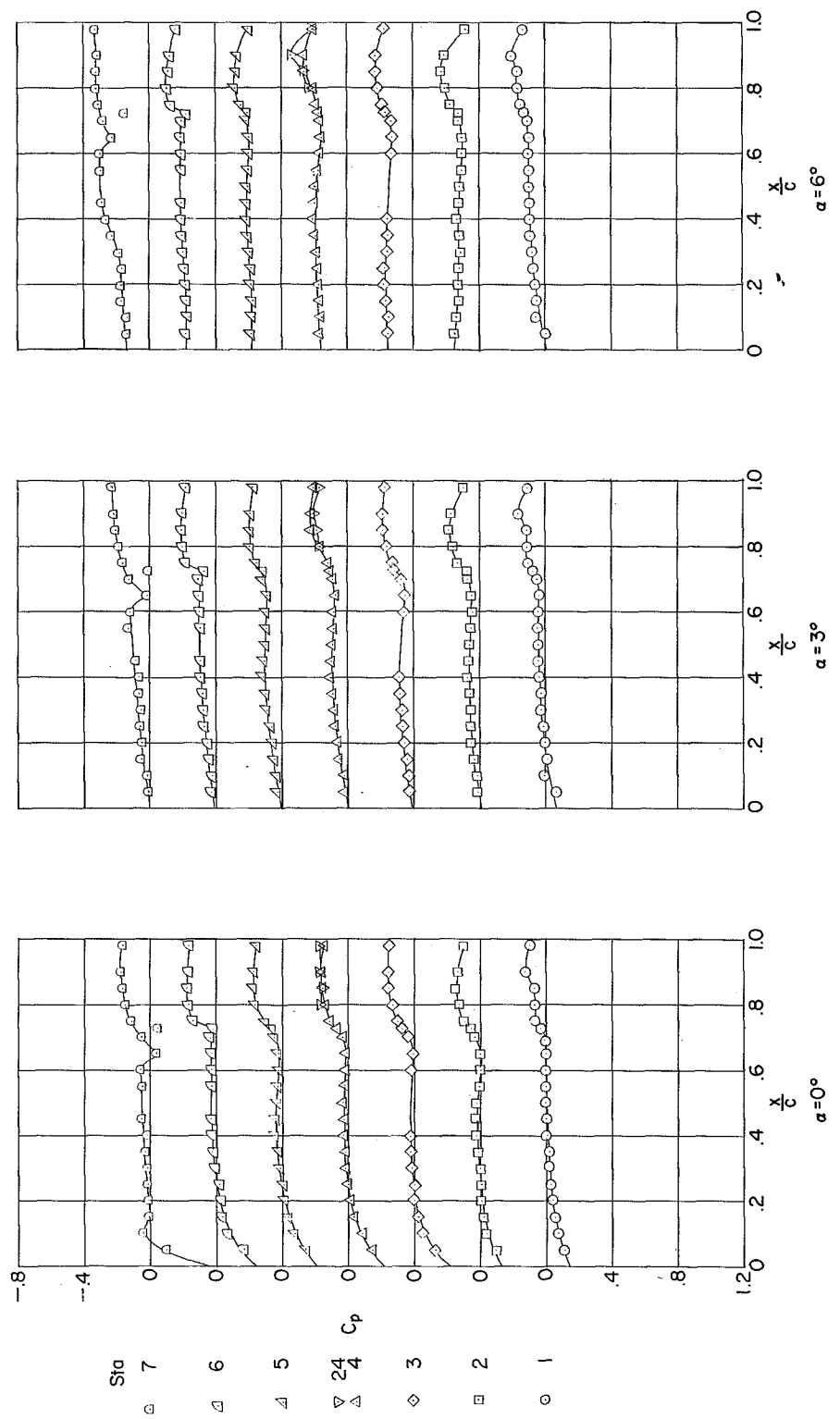
(a) $\alpha = -15^\circ$ to -9° .

Figure 5.- Composite upper-surface chordwise pressure distributions for the basic wing. Stations 1 to 4 obtained from configuration 6 and station 24, 5 to 7 obtained from configuration 3. $M = 1.61$; $R = 3.6 \times 10^6$; $\delta = 0^\circ$.

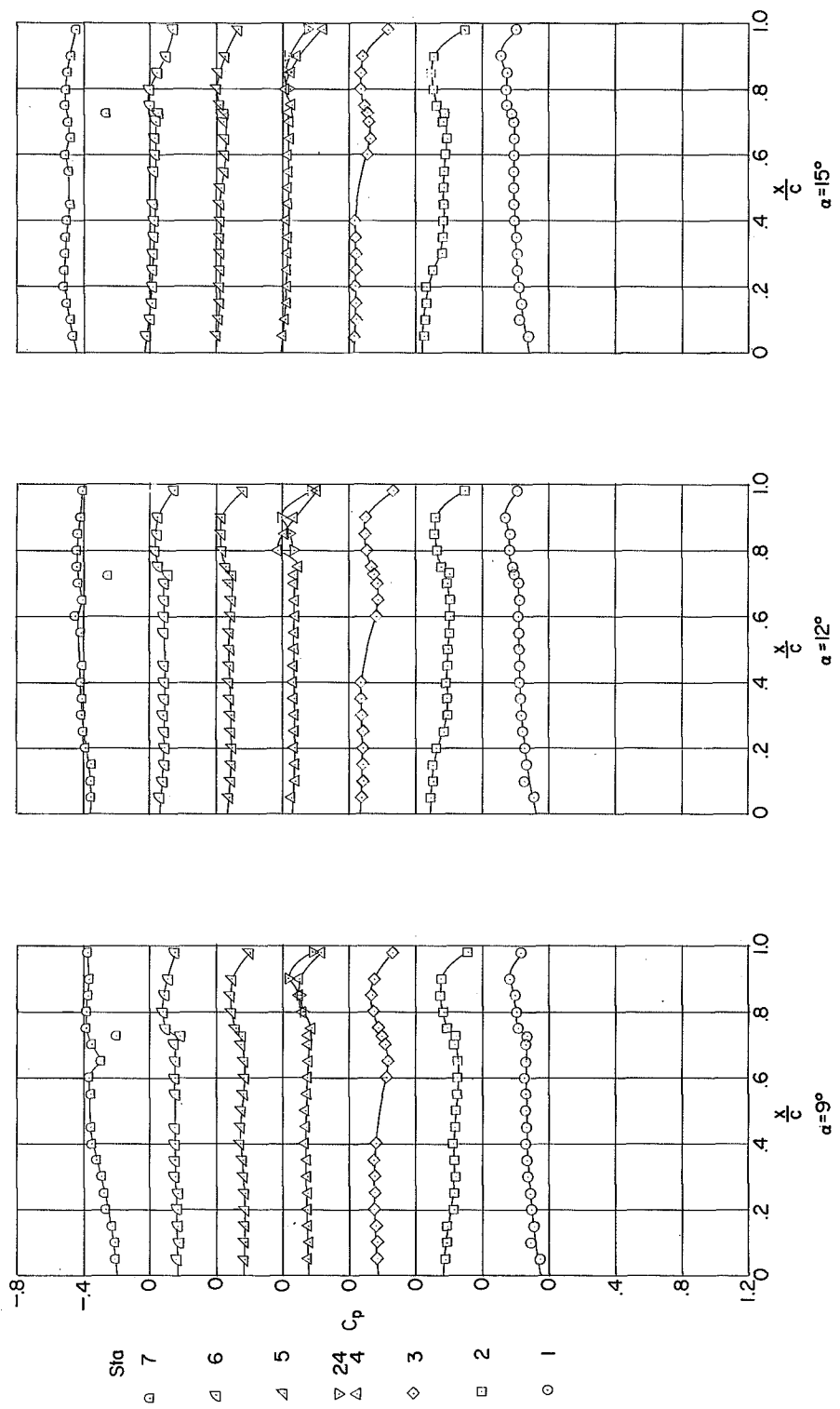


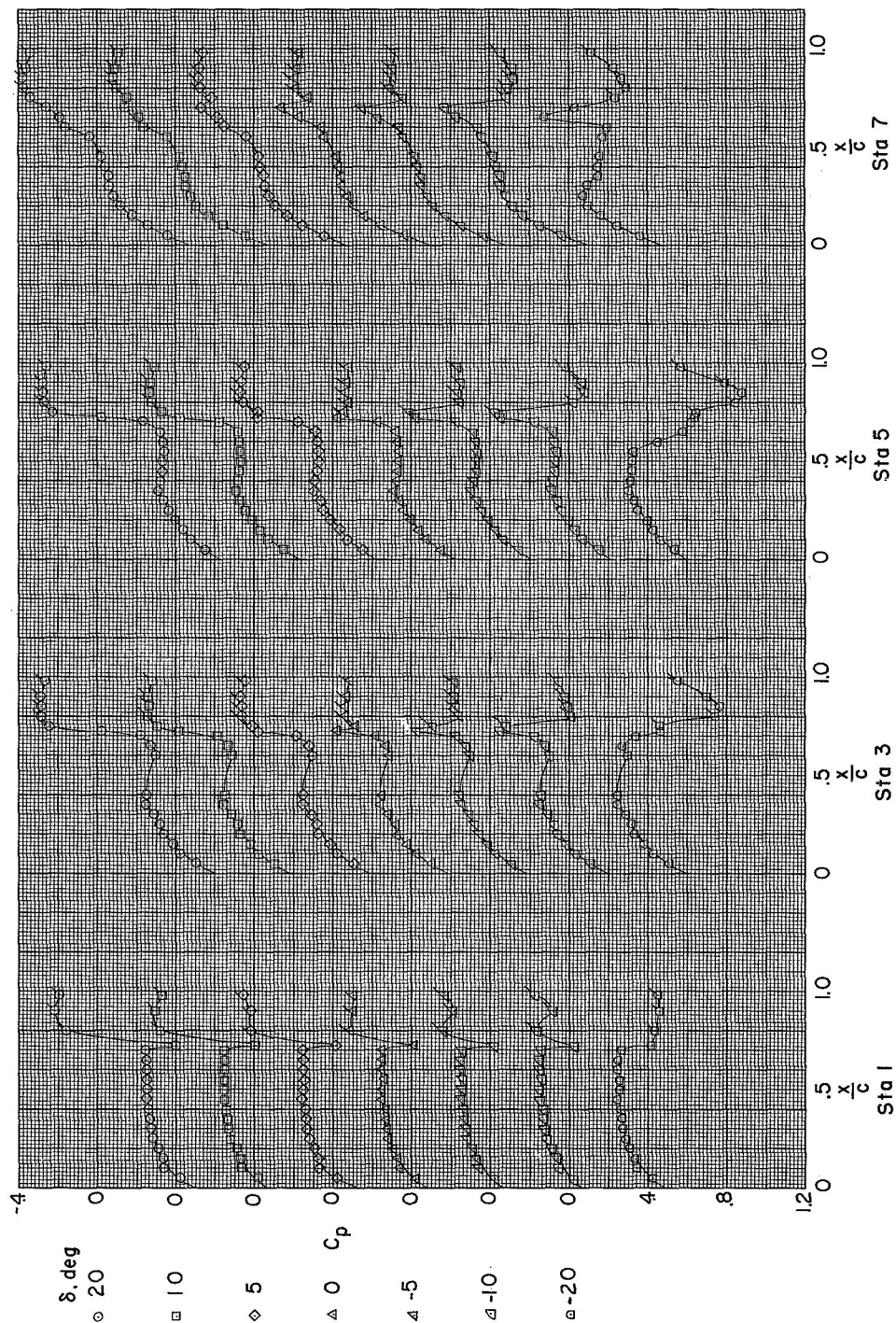
(b) $\alpha = -6^\circ$ to 0° .

Figure 5.- Continued.



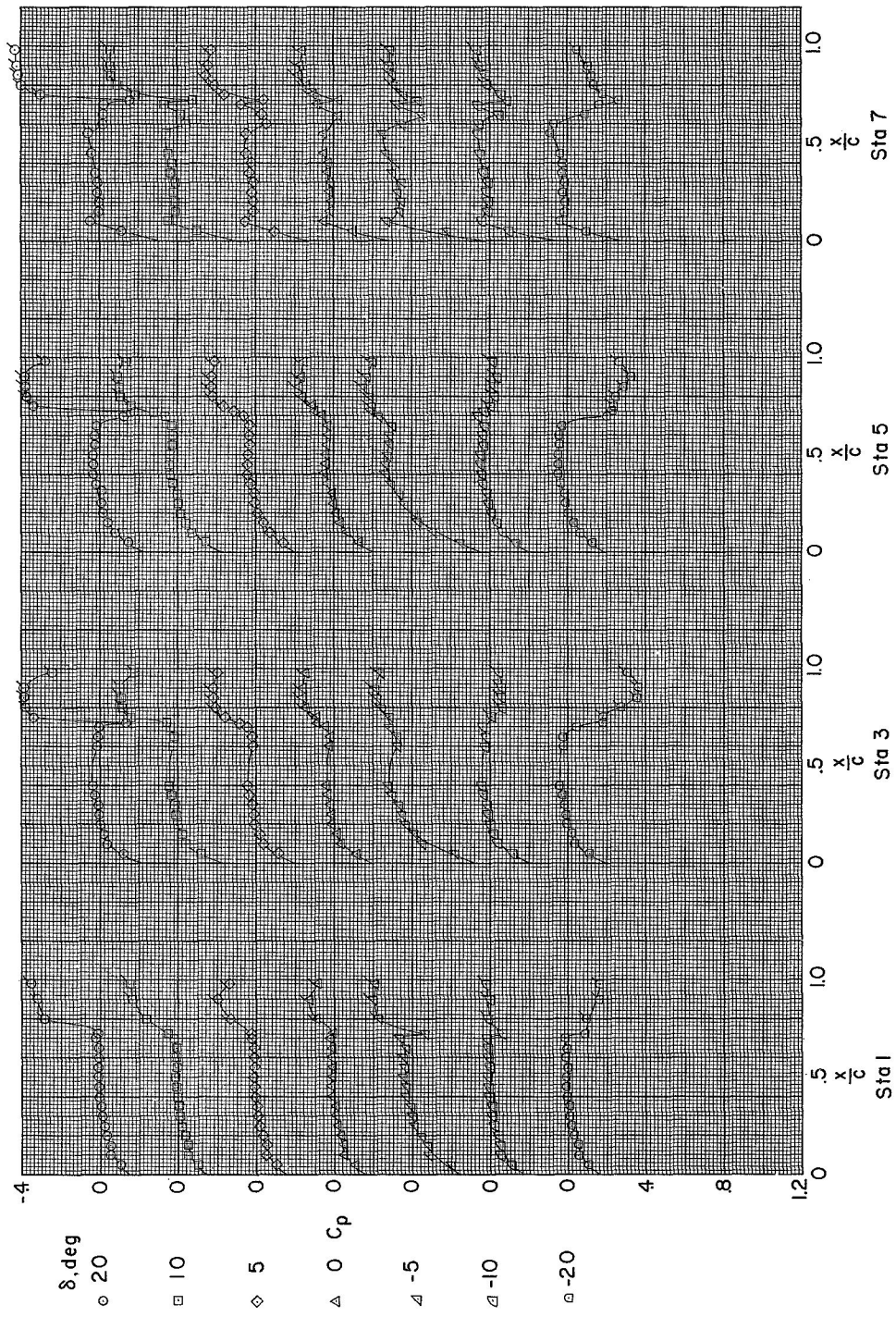
(c) $\alpha = 0^\circ$ to 6° .
Figure 5.- Continued.





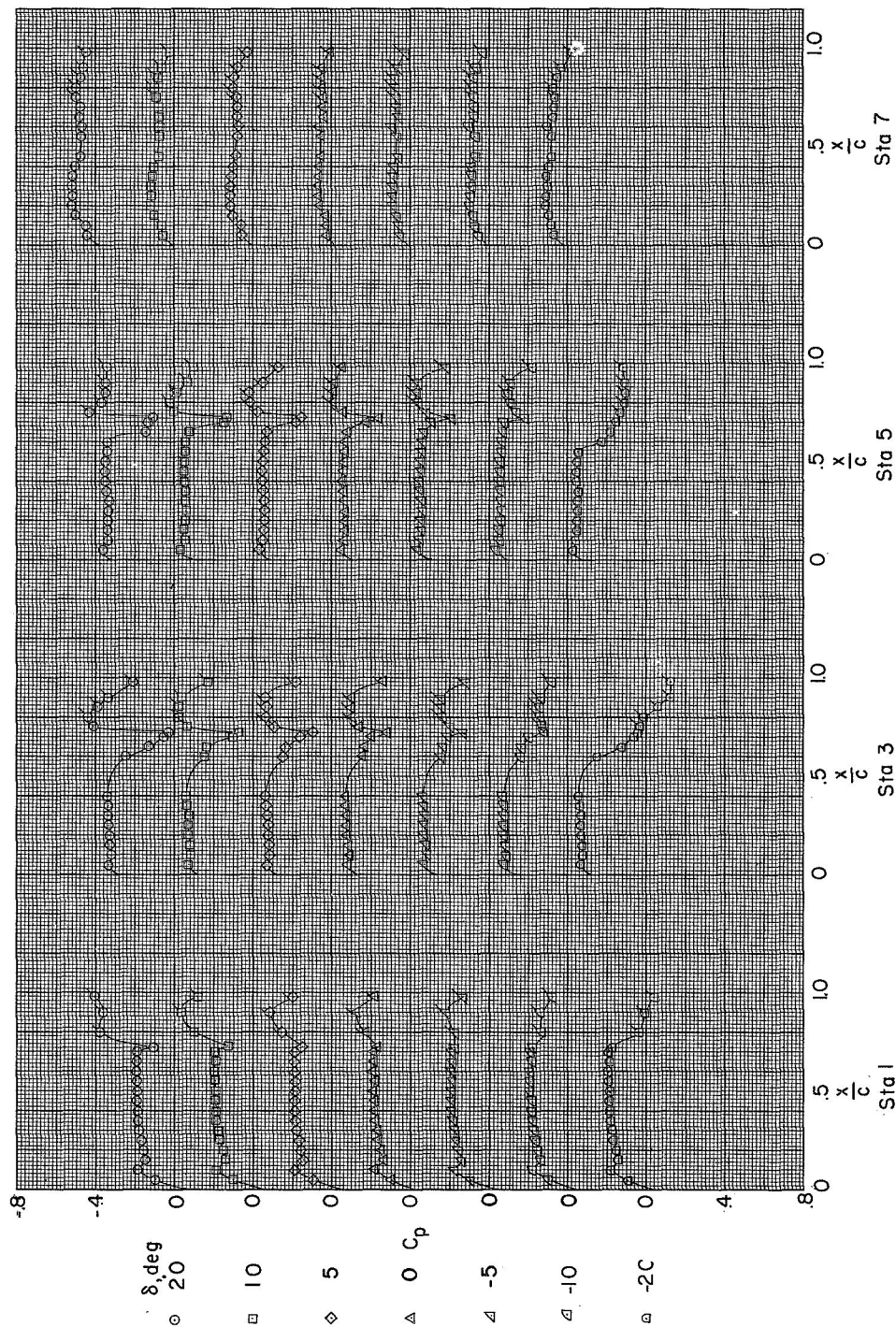
(a) $\alpha = -12^\circ$.

Figure 6.- Upper-surface chordwise pressure distributions for configuration 1. Flagged symbols indicate orifices on control. $M = 1.61$; $R = 3.6 \times 10^6$.



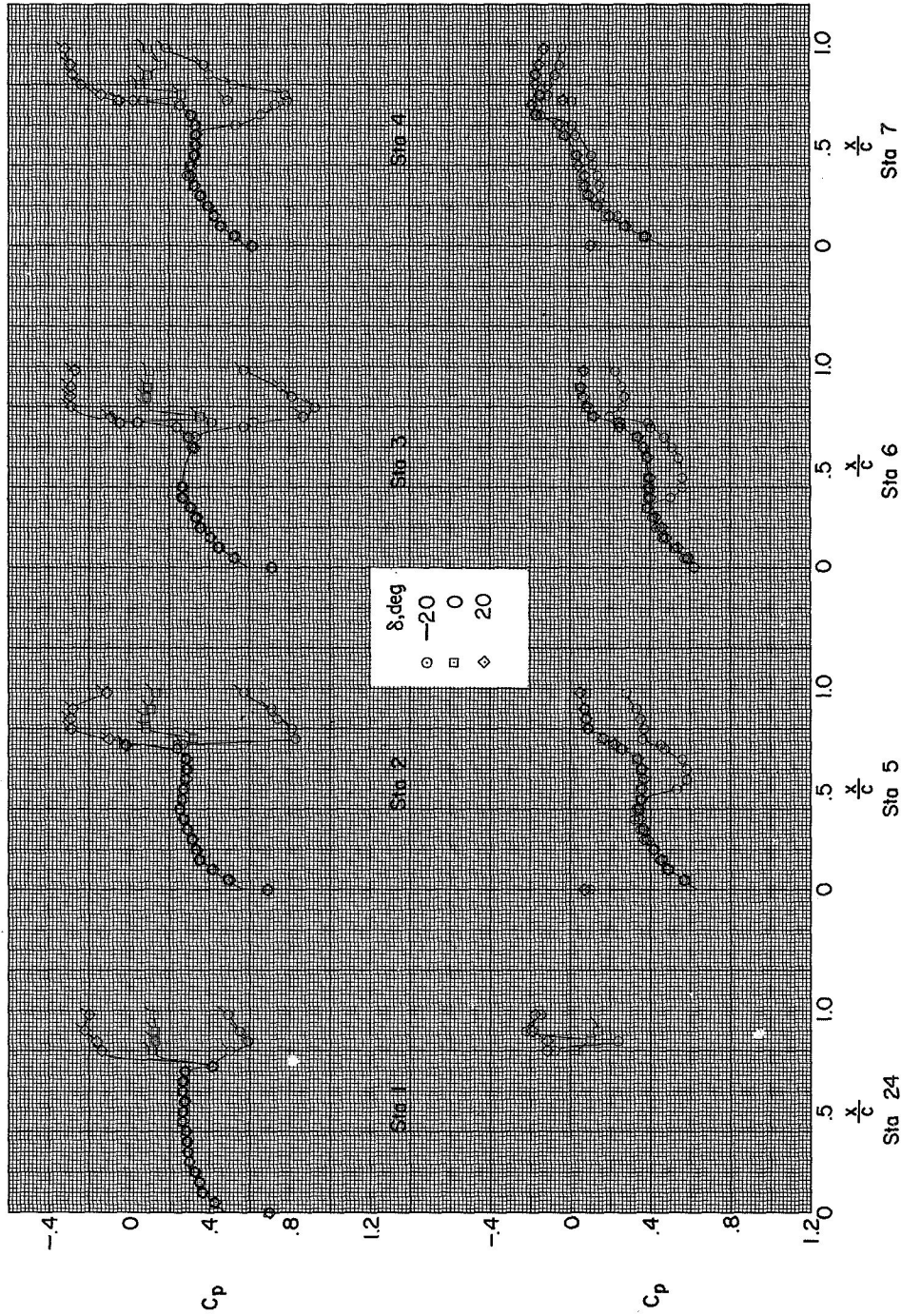
(b) $\alpha = 0^\circ$.

Figure 6.- Continued.



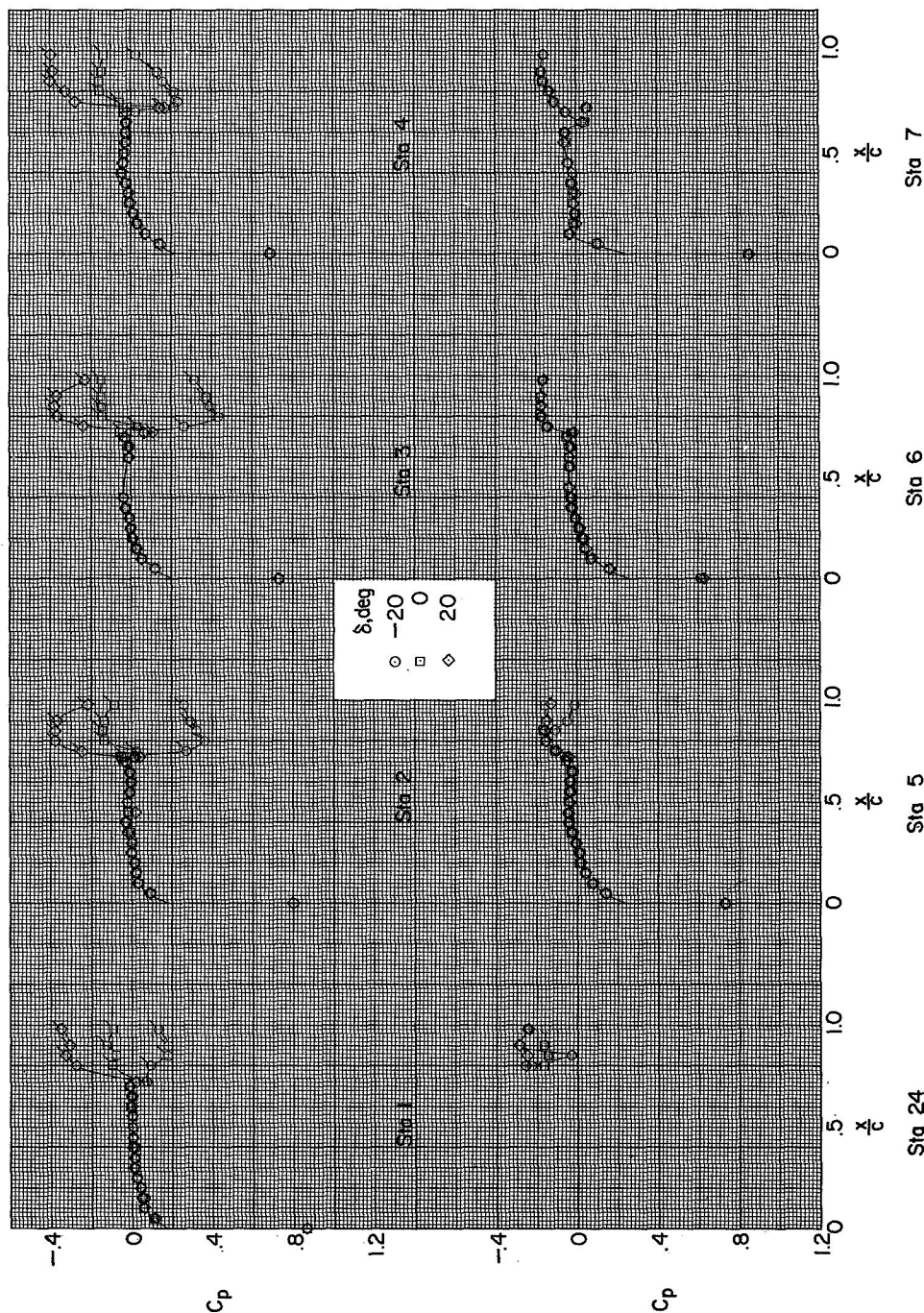
(c) $\alpha = 12^\circ$.

Figure 6.- Concluded.



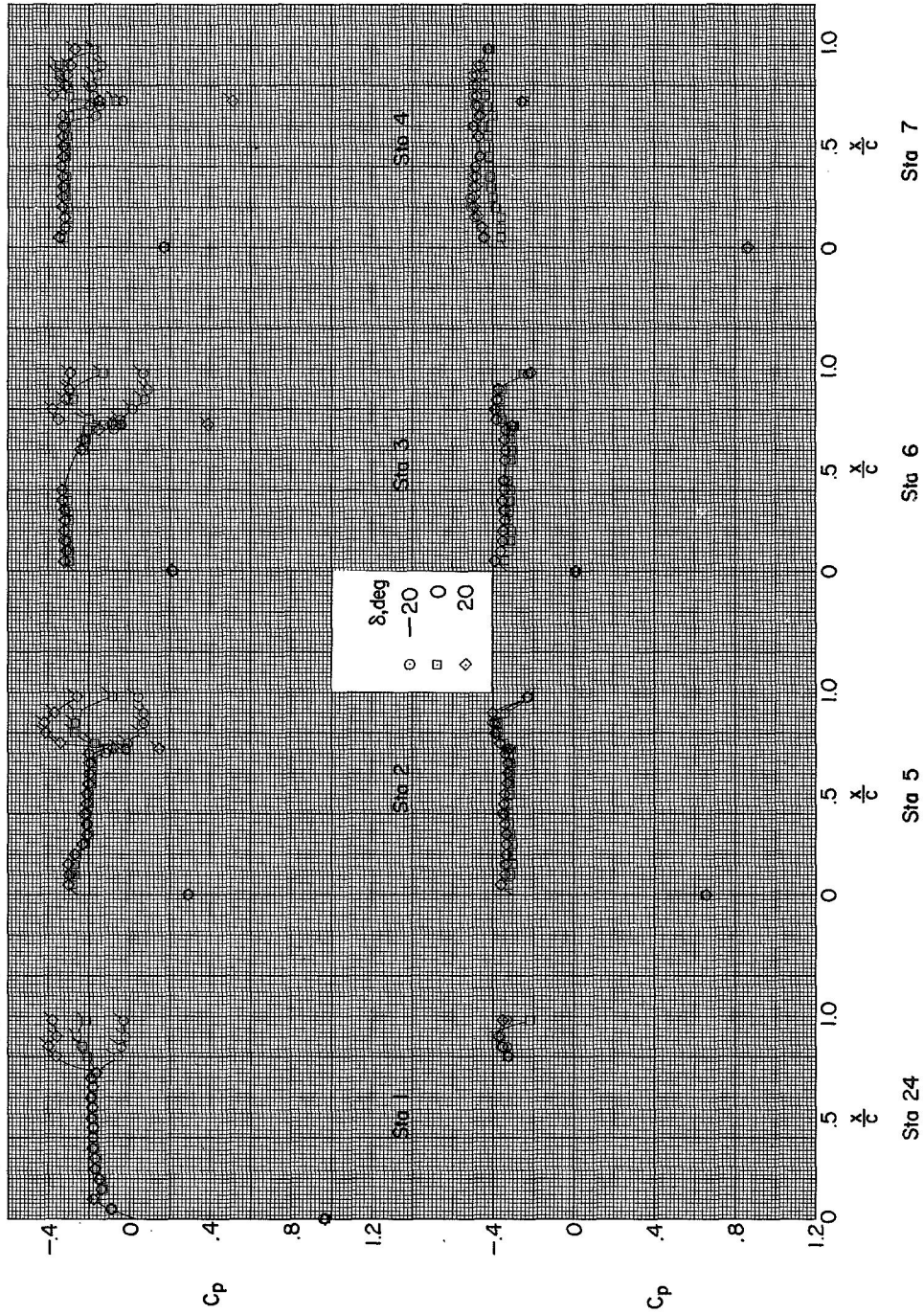
(a) $\alpha = -12^\circ$.

Figure 7.- Upper-surface chordwise pressure distributions for configuration 3. Flagged symbols indicate orifices on control. $M = 1.61$; $R = 3.6 \times 10^6$.



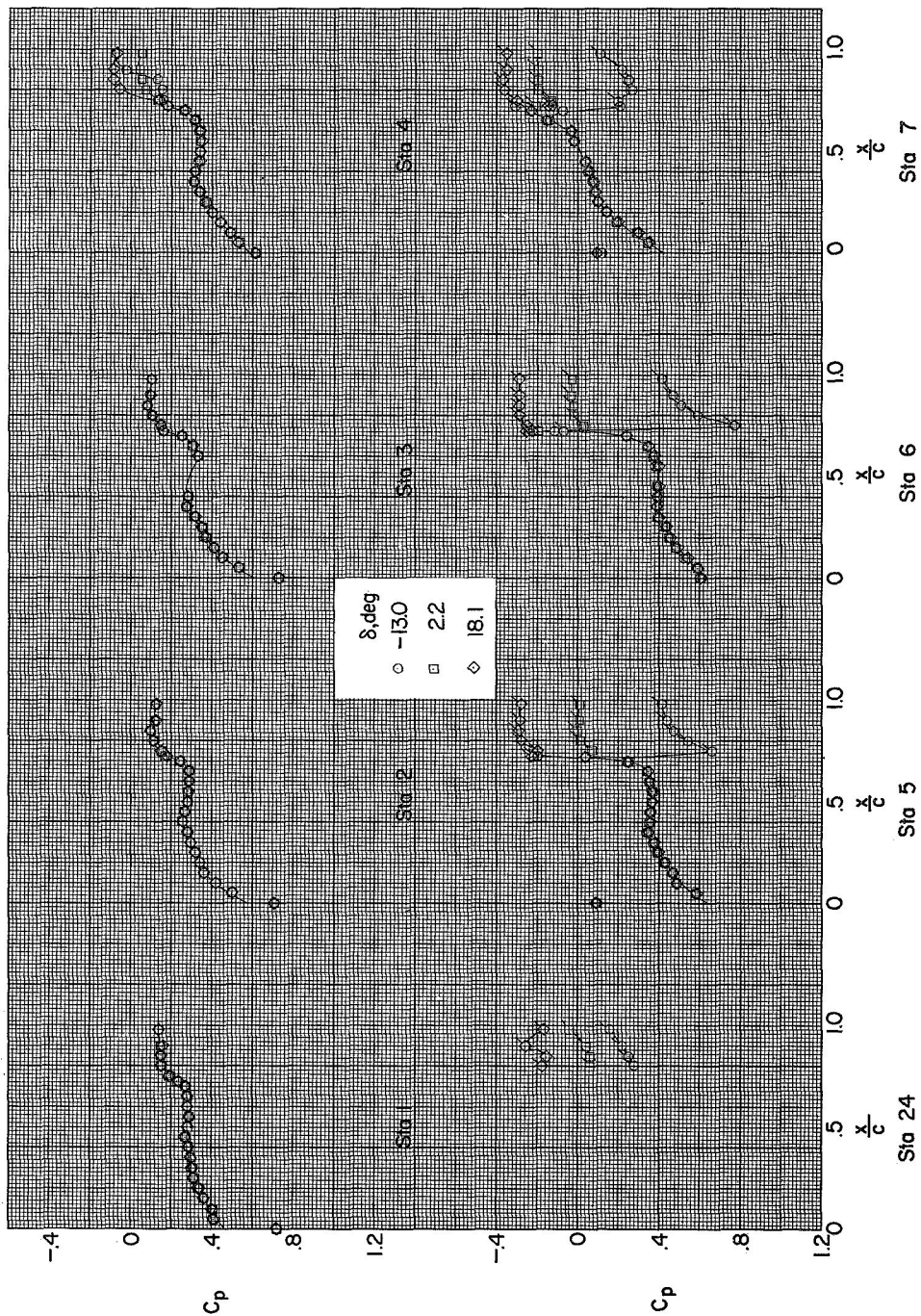
(b) $\alpha = 0^\circ$

Figure 7.- Continued.



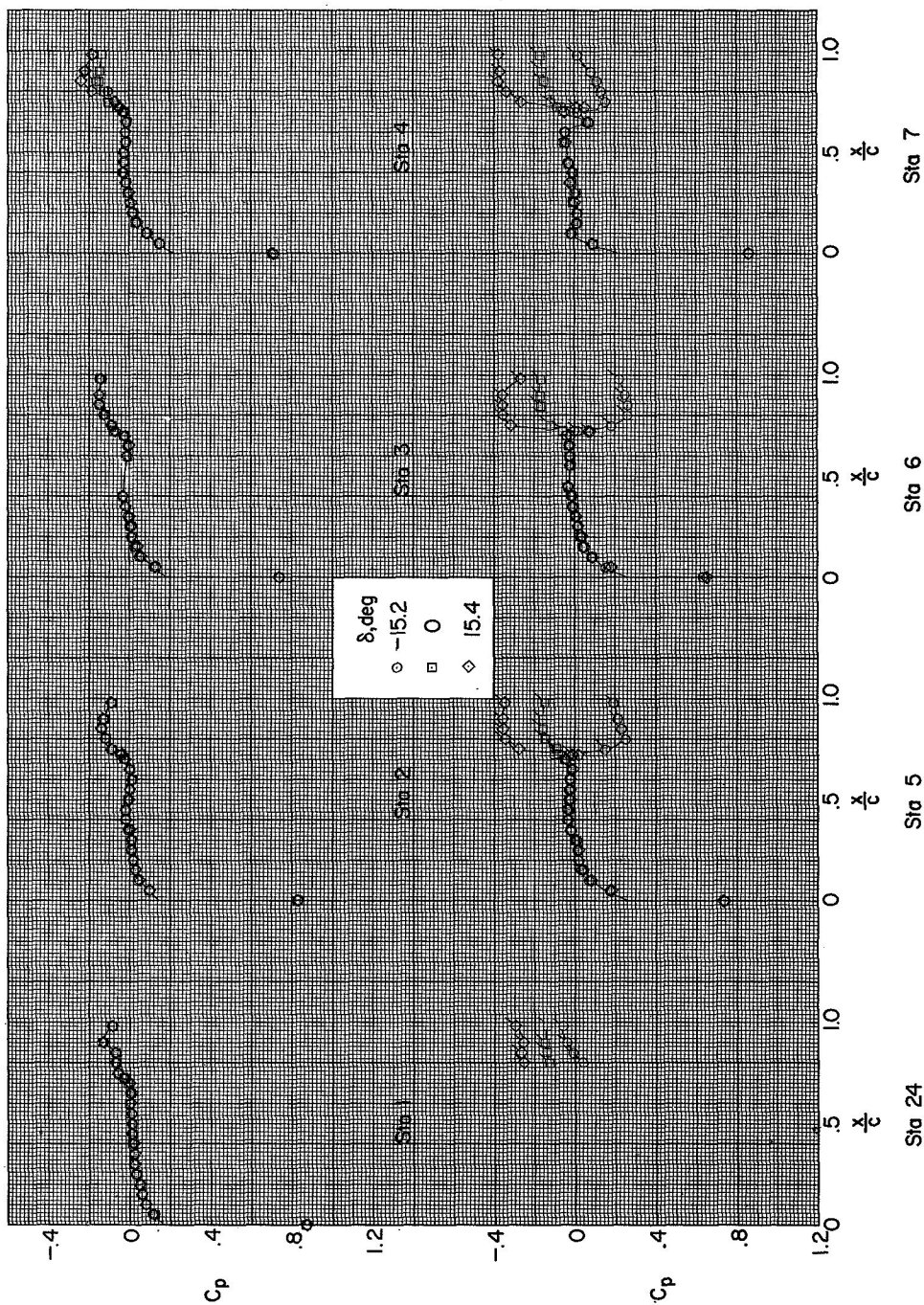
(c) $\alpha = 12^\circ$.

Figure 7.- Concluded.



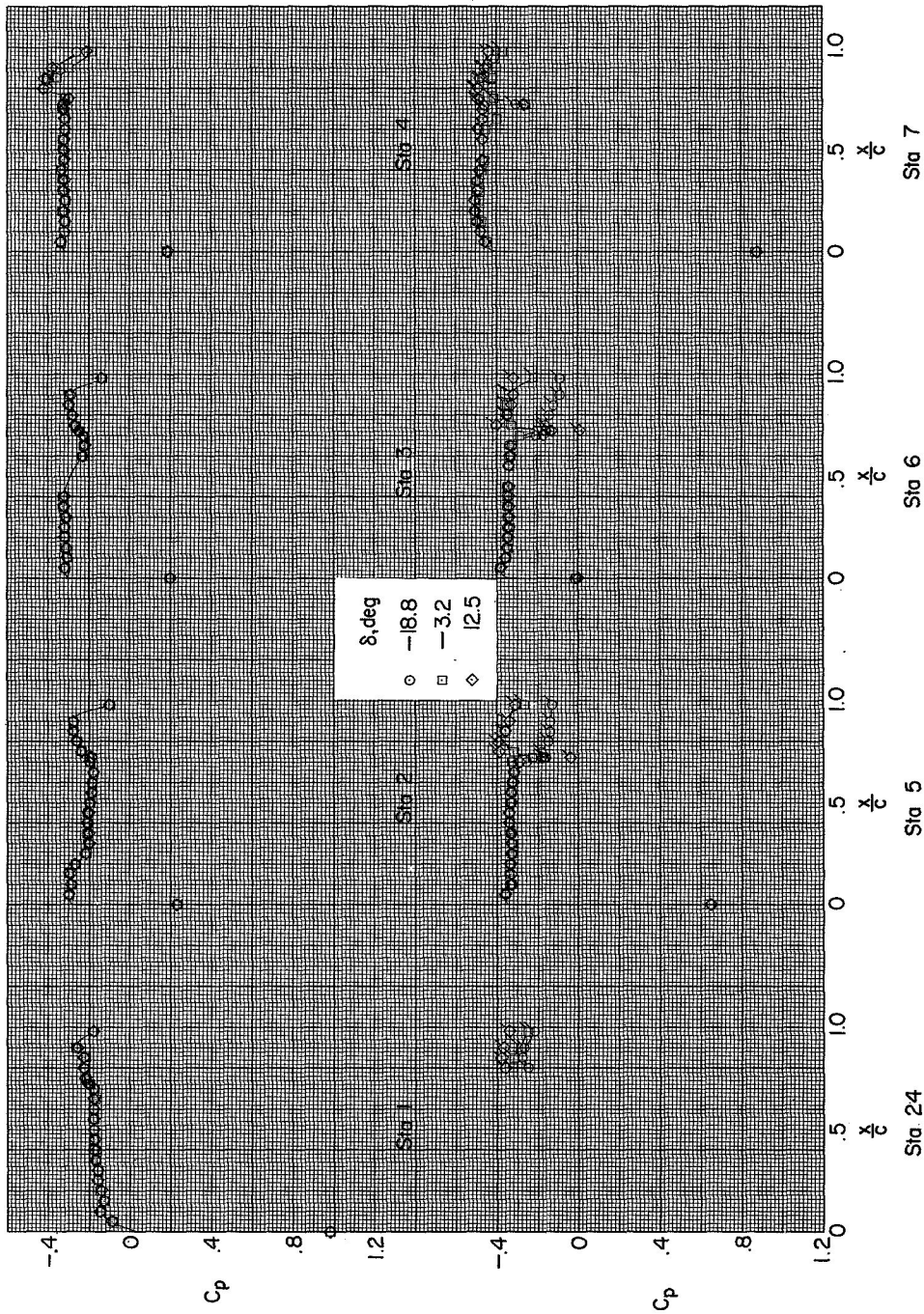
(a) $\alpha = -12^\circ$.

Figure 8.- Upper-surface chordwise pressure distributions for configuration 6. Flagged symbols indicate orifices on control. $M = 1.61$; $R = 3.6 \times 10^6$.



(b) $\alpha = 0^\circ$.

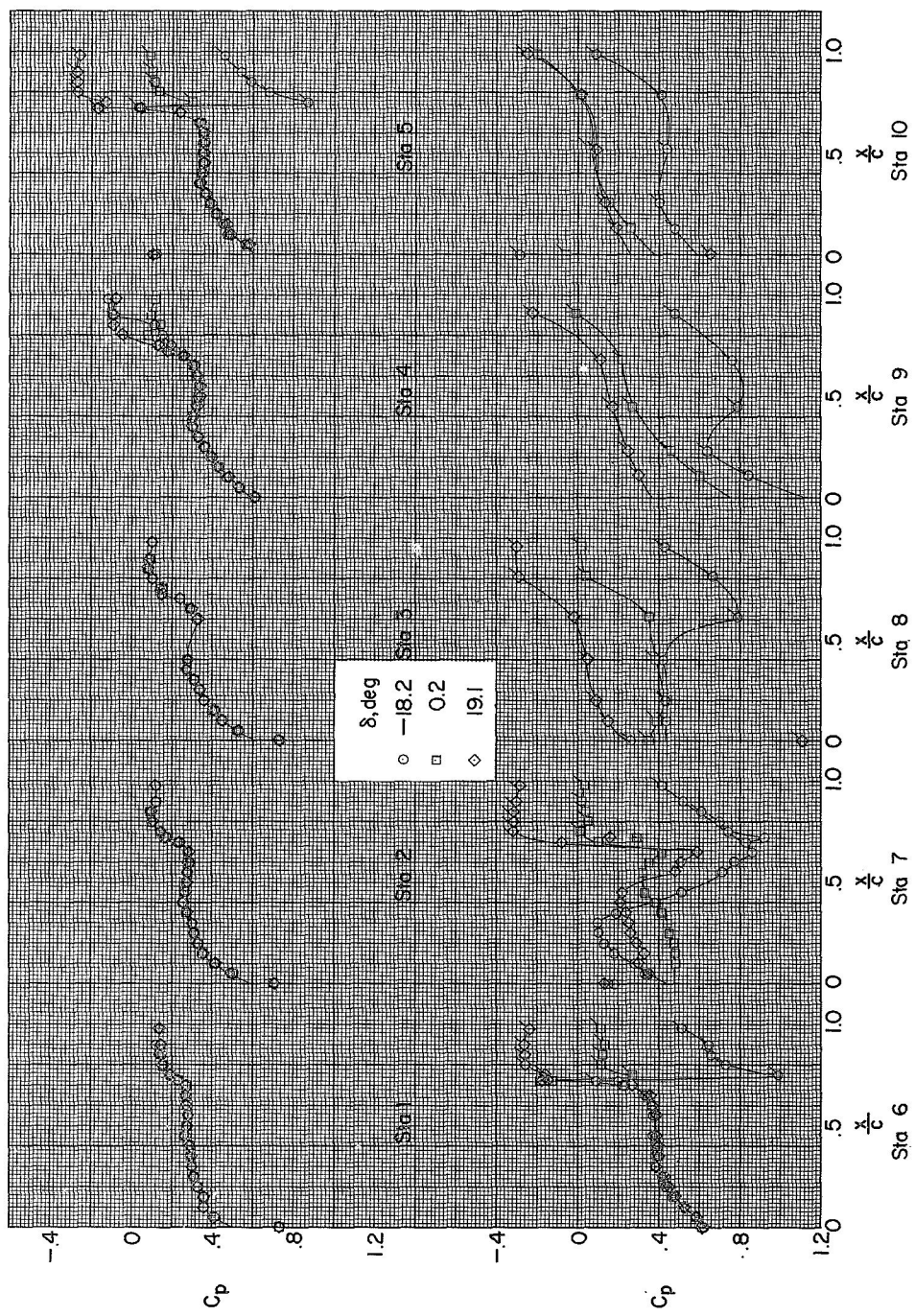
Figure 8.- Continued.



(c) $\alpha = 12^\circ$.

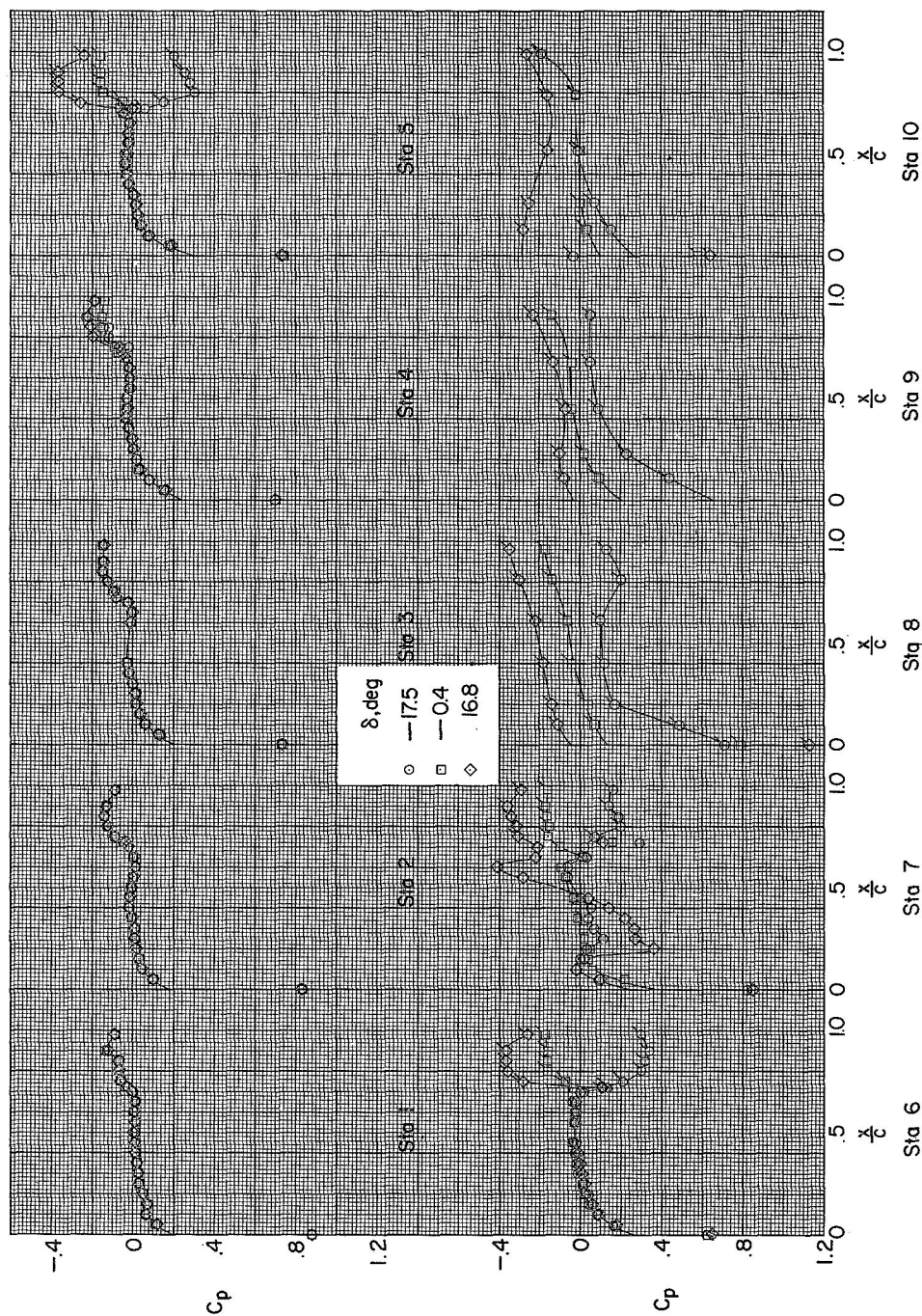
Figure 8.- Concluded.

44



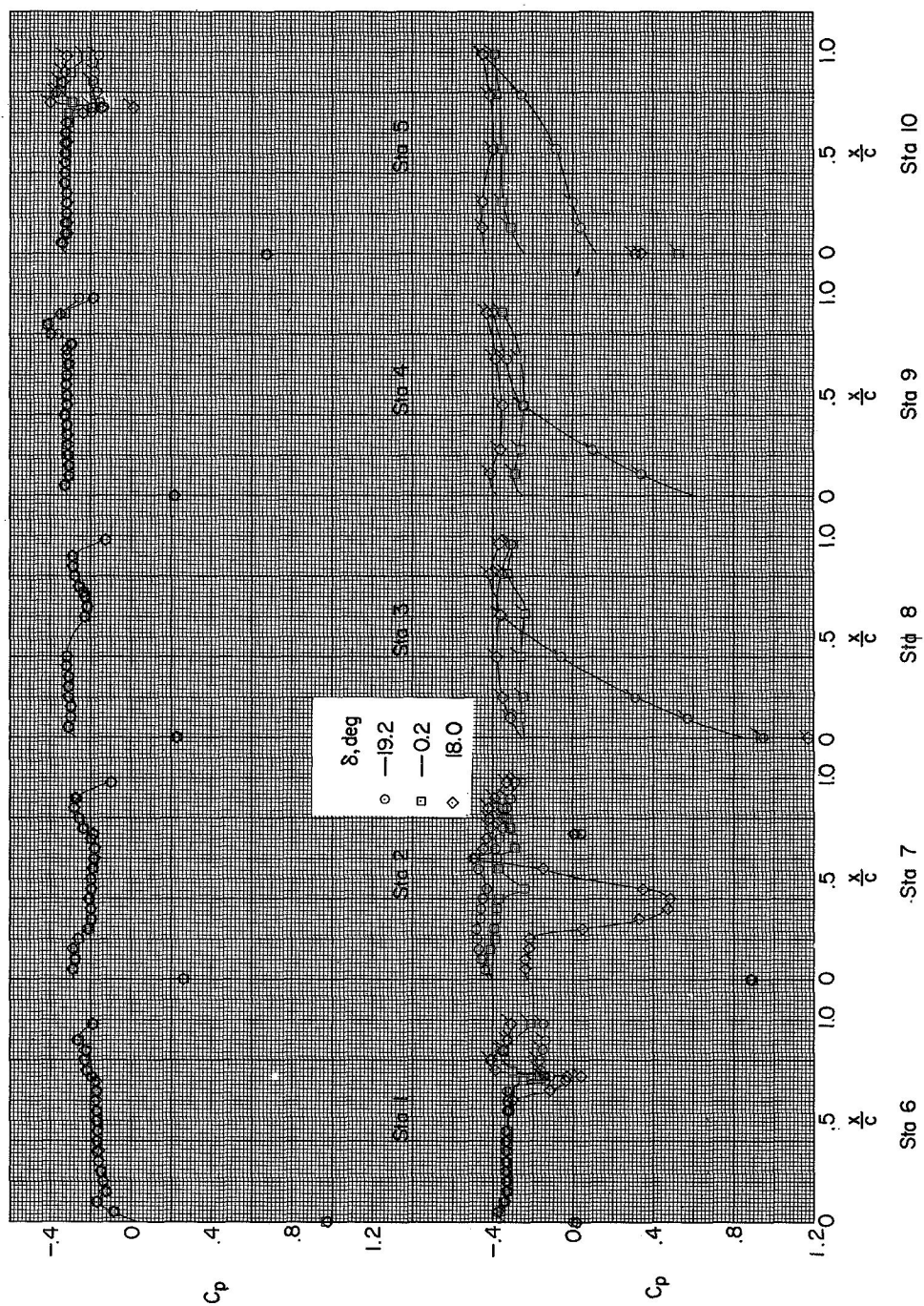
(a) $\alpha = -12^\circ$.

Figure 9.- Upper-surface chordwise pressure distributions for configuration 7. Flagged symbols indicate orifices on control. $M = 1.61$; $R = 3.6 \times 10^6$.



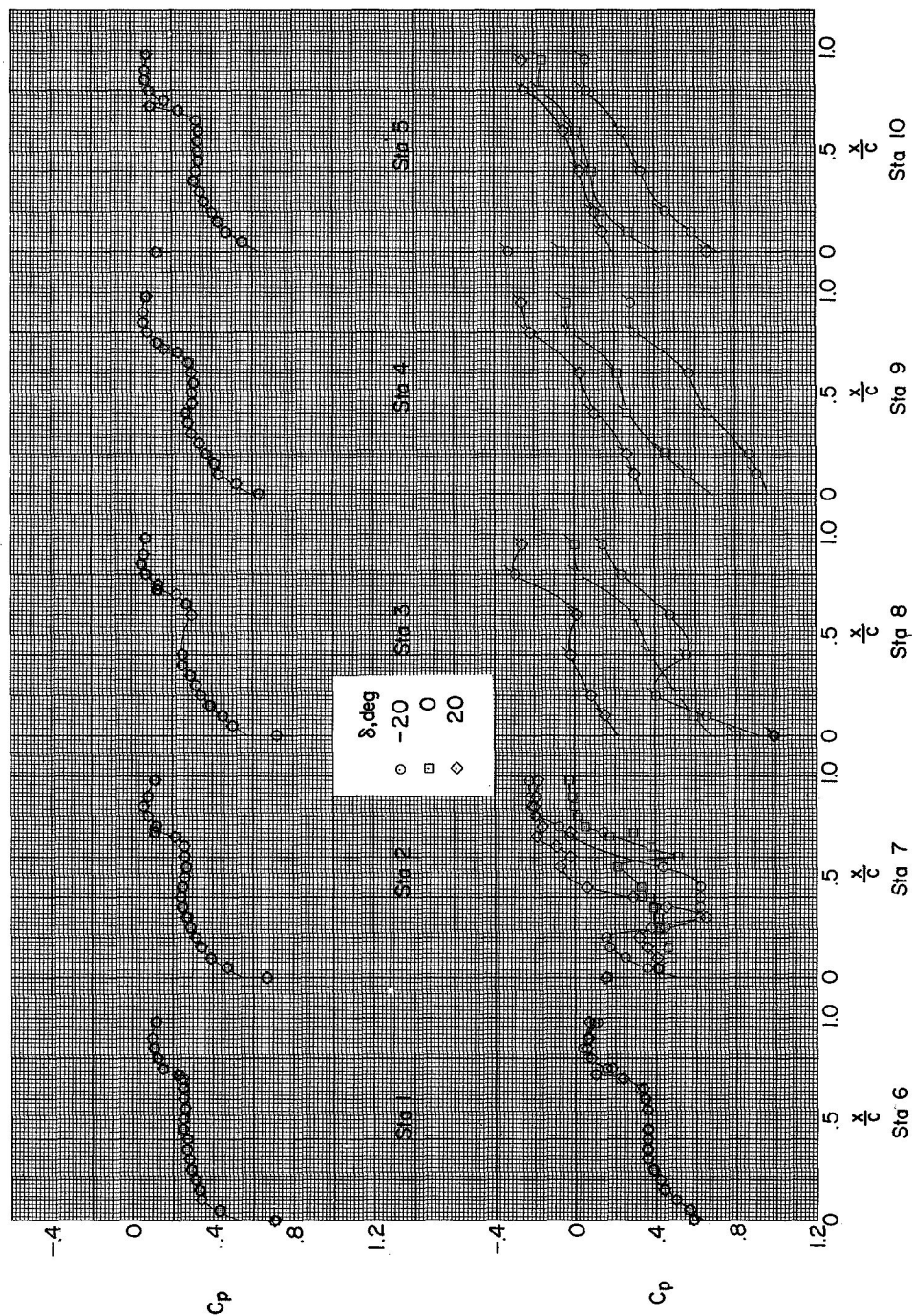
(b) $\alpha = 0^\circ$.

Figure 9.- Continued.



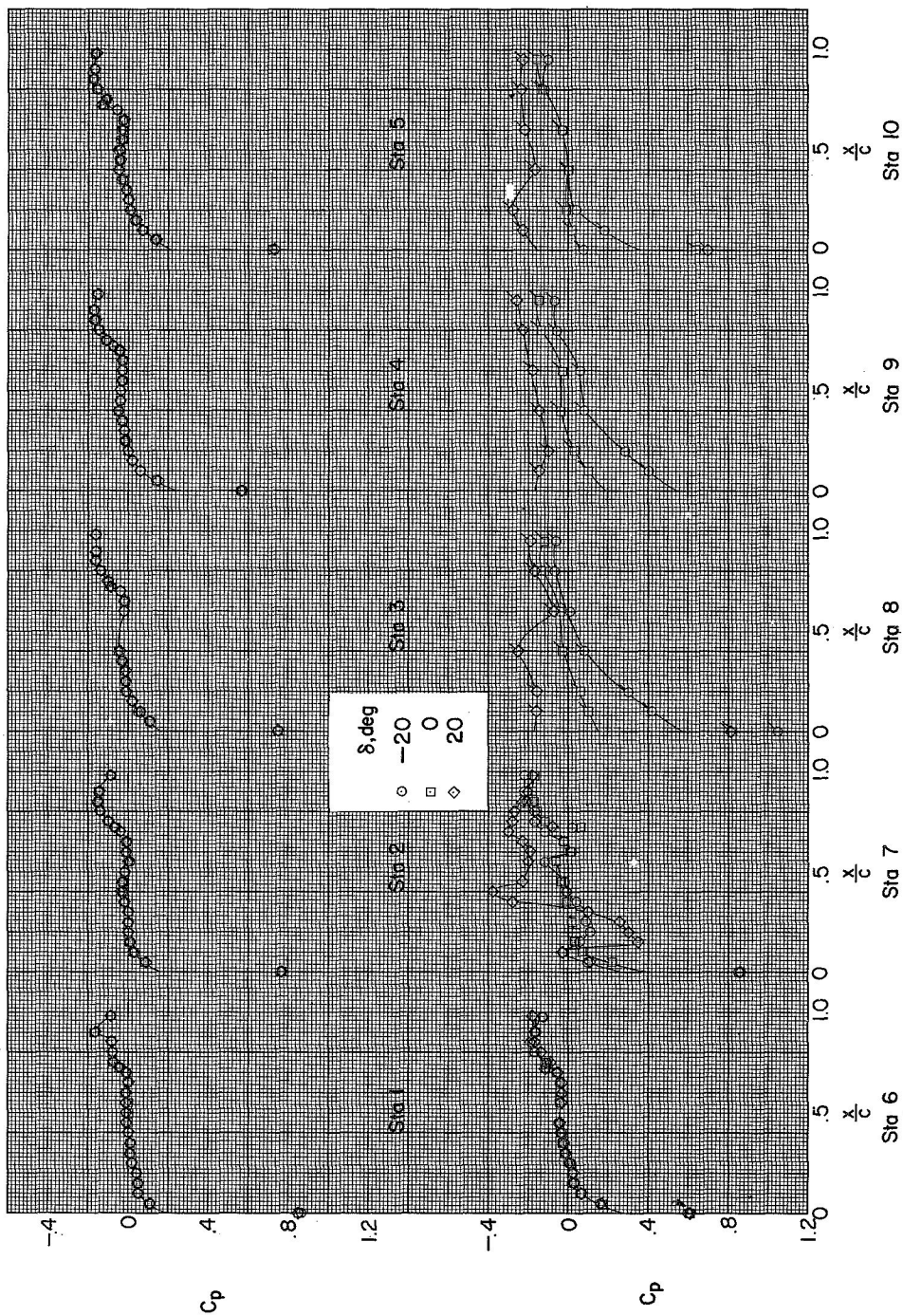
(c) $\alpha = 12^\circ$.

Figure 9.- Concluded.



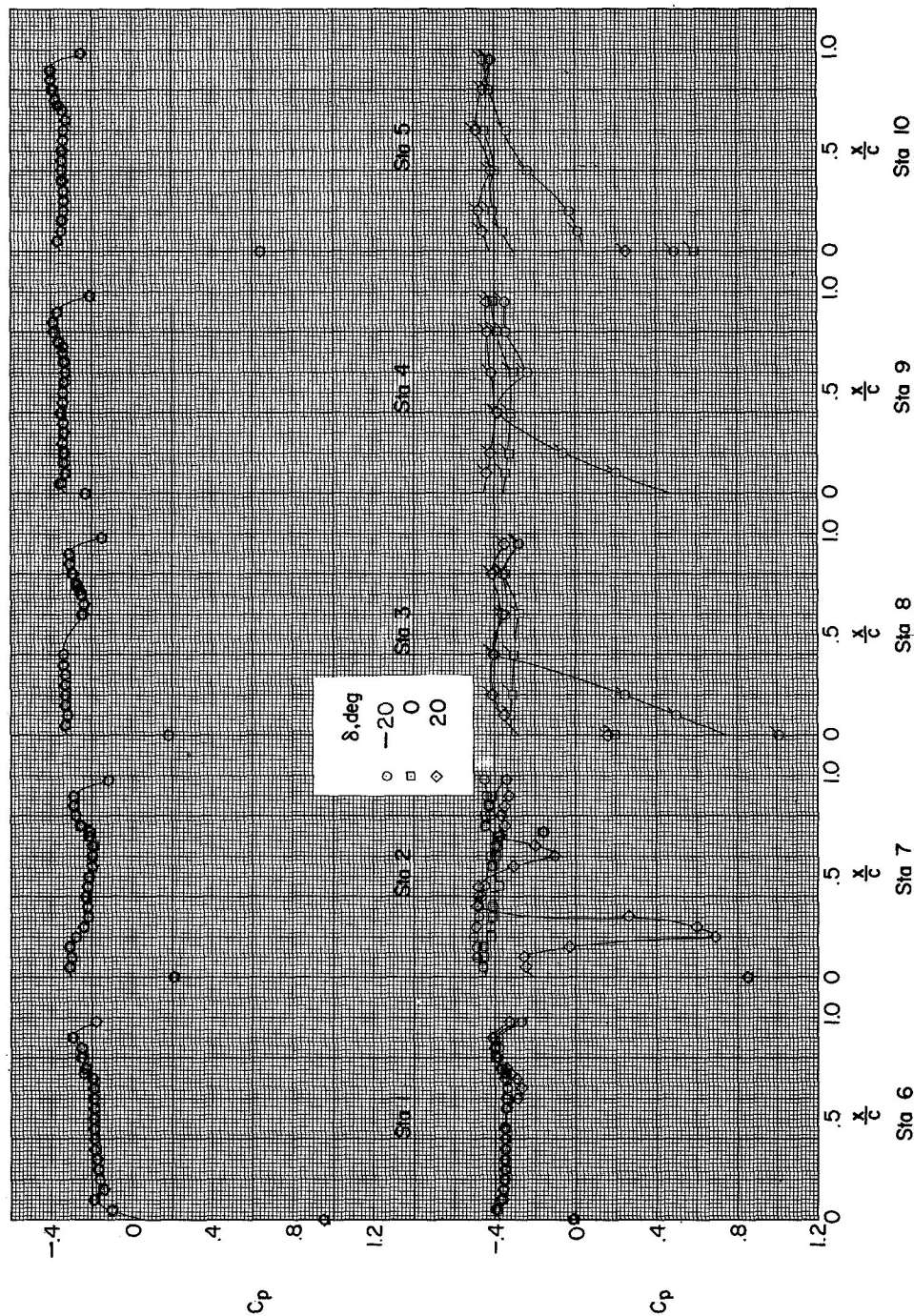
(a) $\alpha = -12^\circ$.

Figure 10.- Upper-surface chordwise pressure distributions for configuration 9. Flagged symbols indicate orifices on control. $M = 1.61$; $R = 3.6 \times 10^6$.



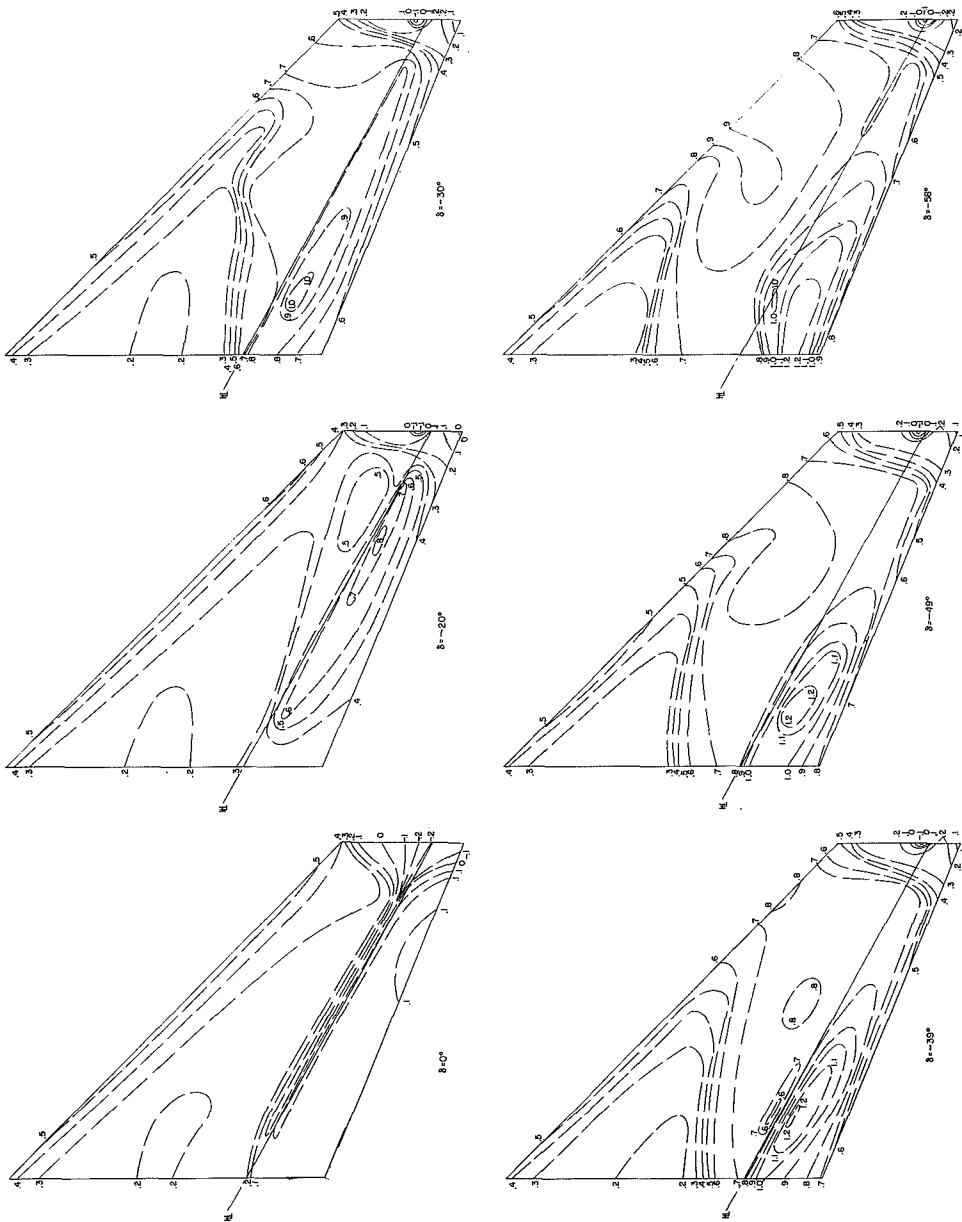
(b) $\alpha = 0^\circ$.

Figure 10.- Continued.



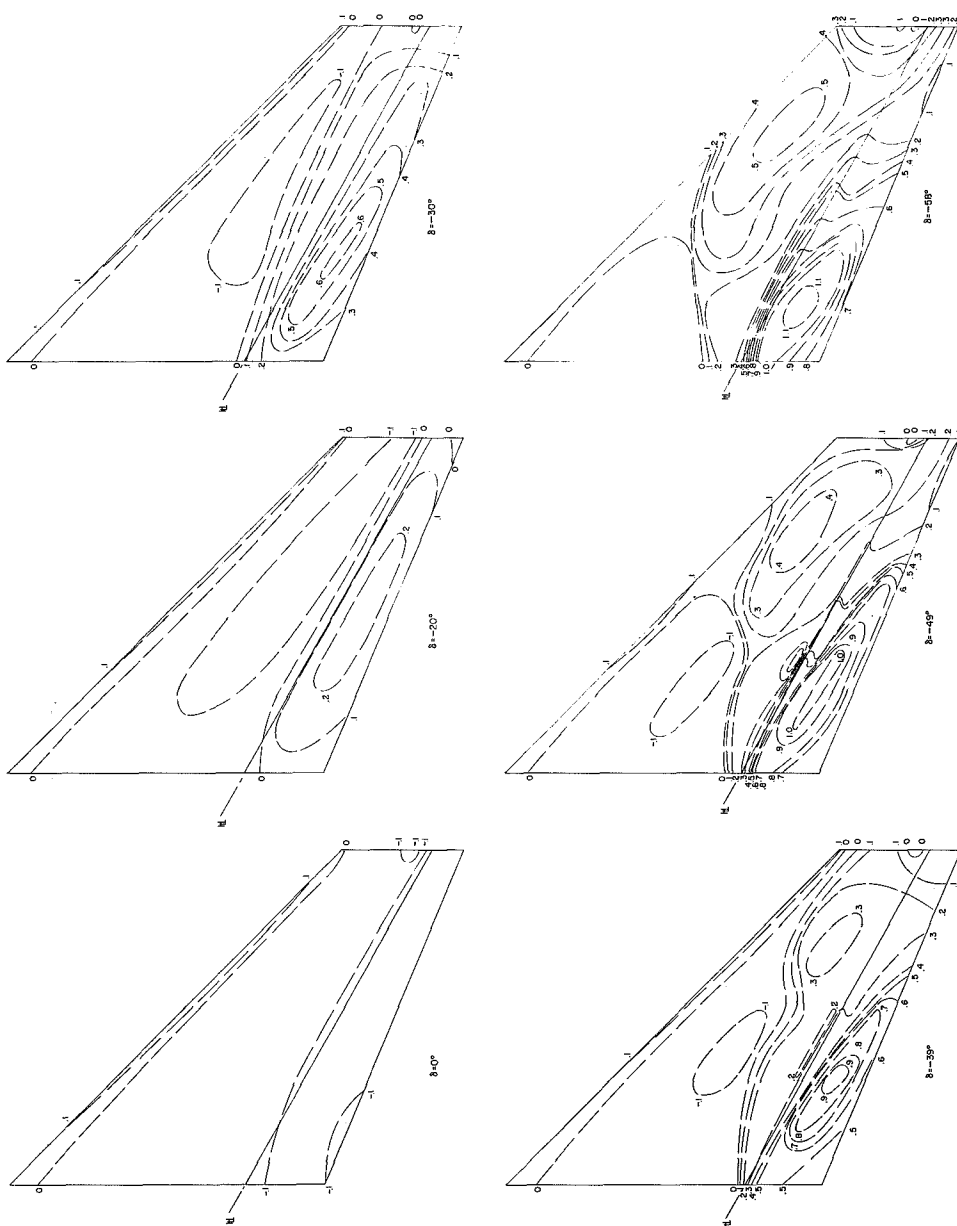
(c) $\alpha = 12^\circ$.

Figure 10.- Concluded.



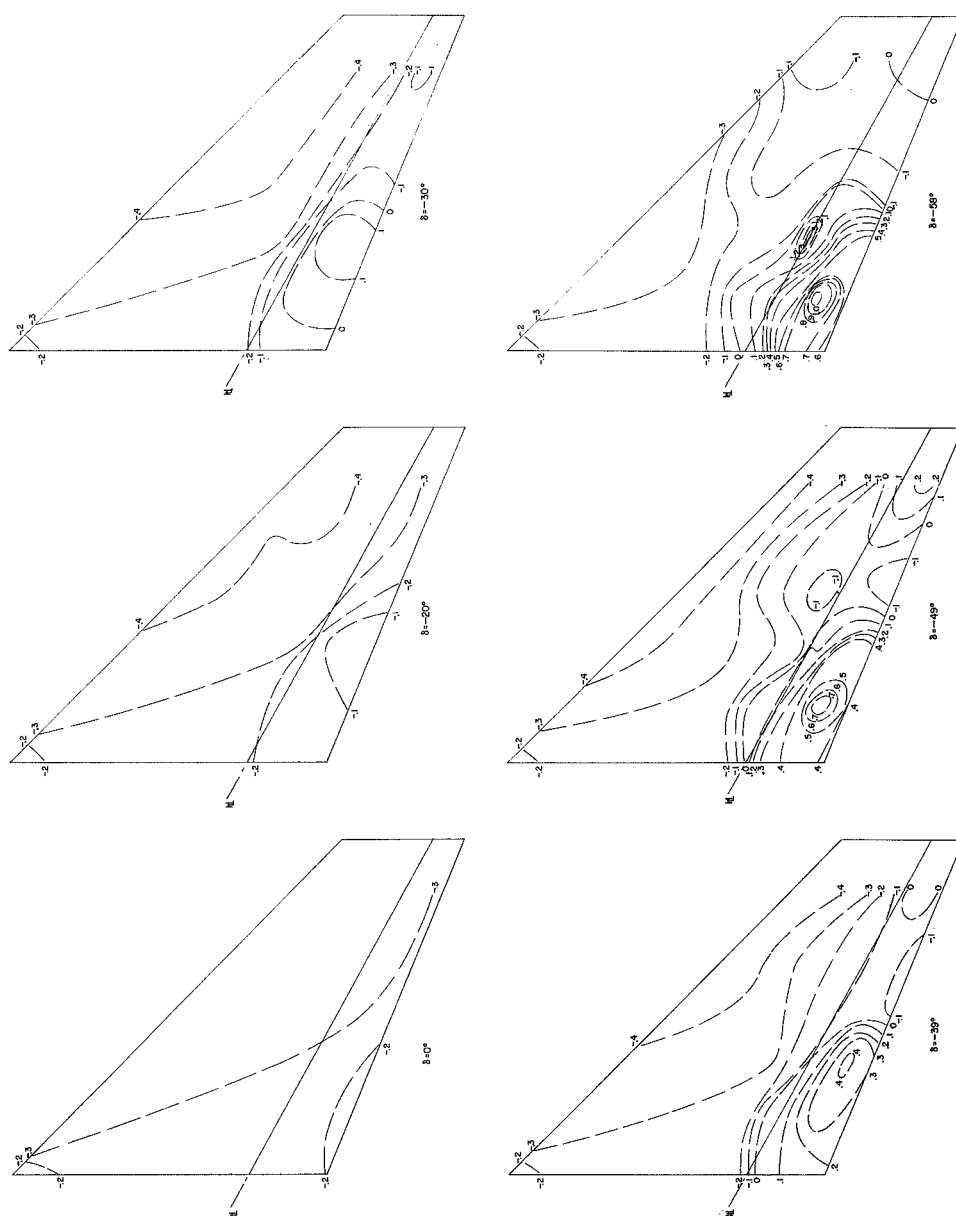
(a) $\alpha = -12^\circ$.

Figure 11.- Upper-surface pressure-coefficient contours for configuration 1. Numbers indicate lines of constant pressure coefficient. $M = 1.61$; $R = 1.7 \times 10^6$.



(b) $\alpha = 0^\circ$.

Figure 11.- Continued.



(c) $\alpha = 12^\circ$.

Figure 11.- Concluded.

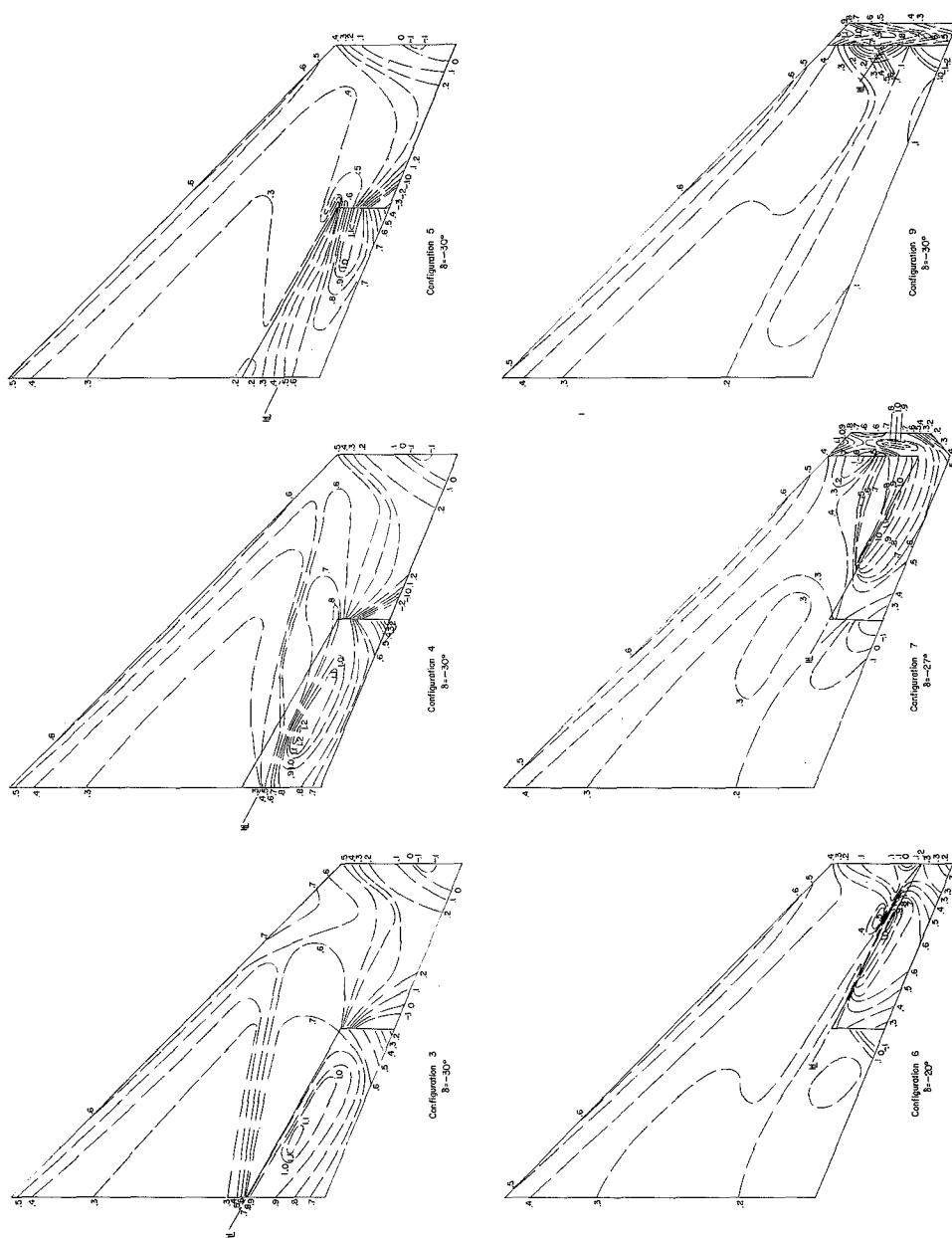
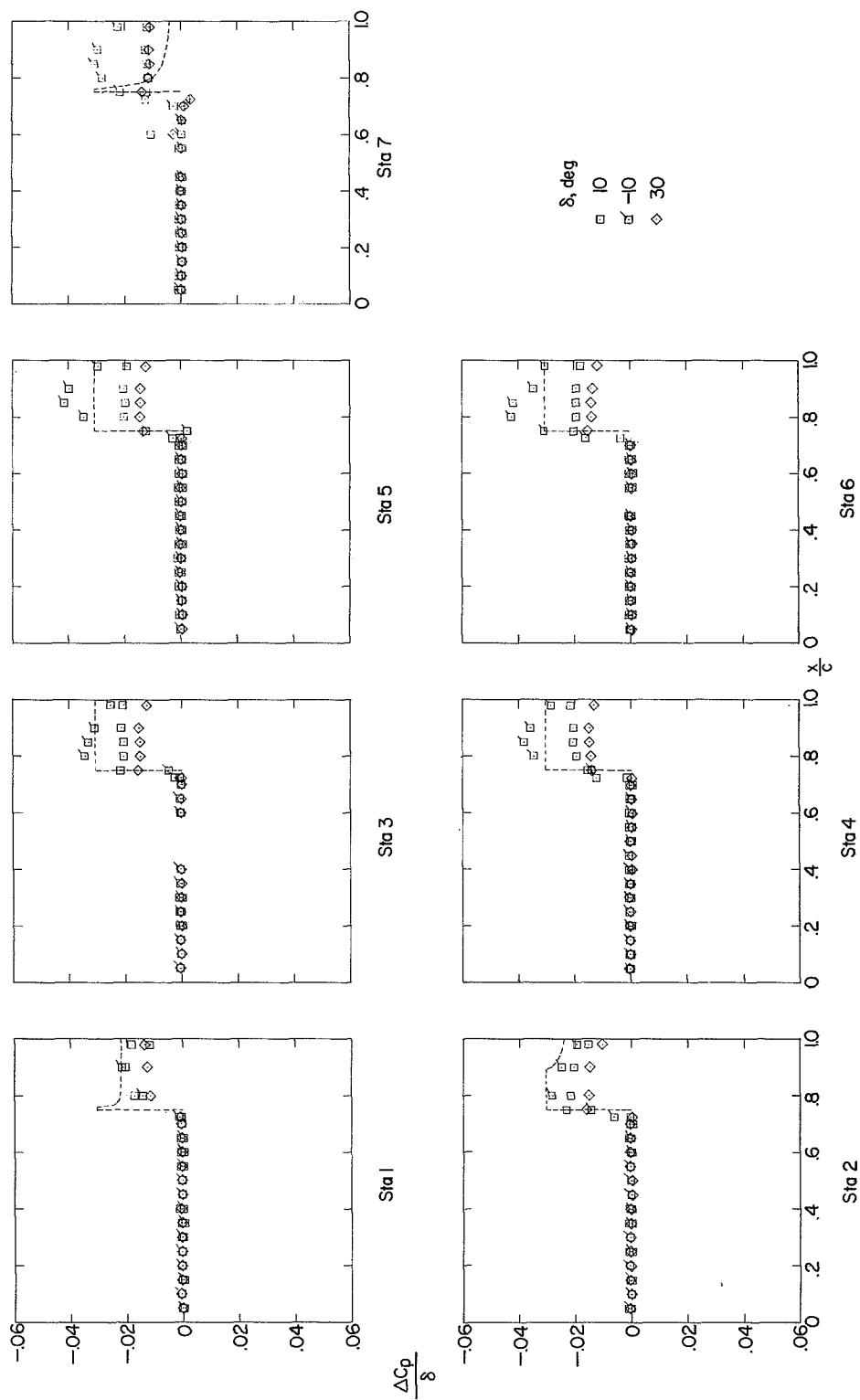
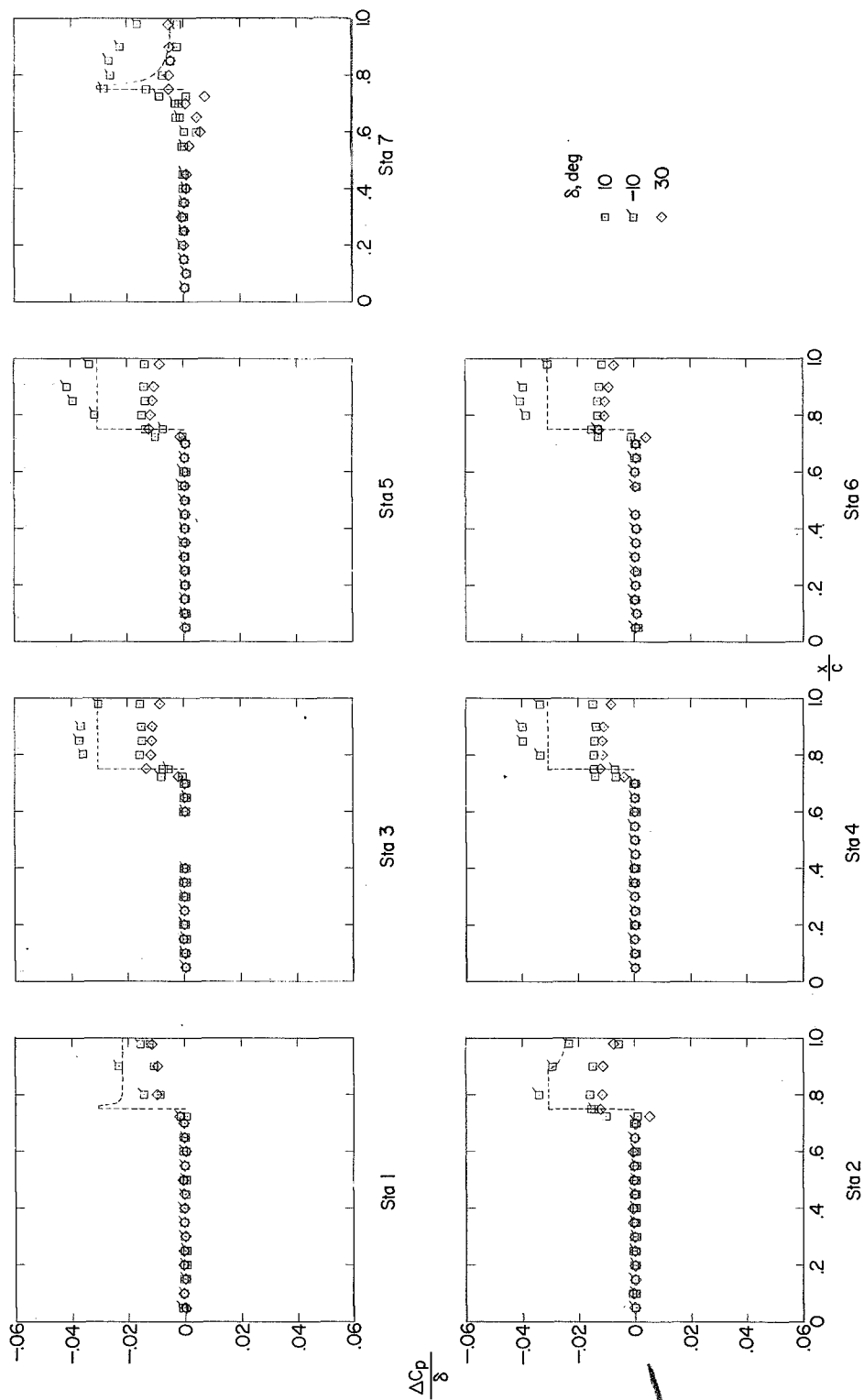


Figure 12.- Upper-surface pressure contours for several control configurations at the maximum negative control deflections obtained. $M = 1.61$; $R = 3.6 \times 10^6$; $\alpha = -12^\circ$.



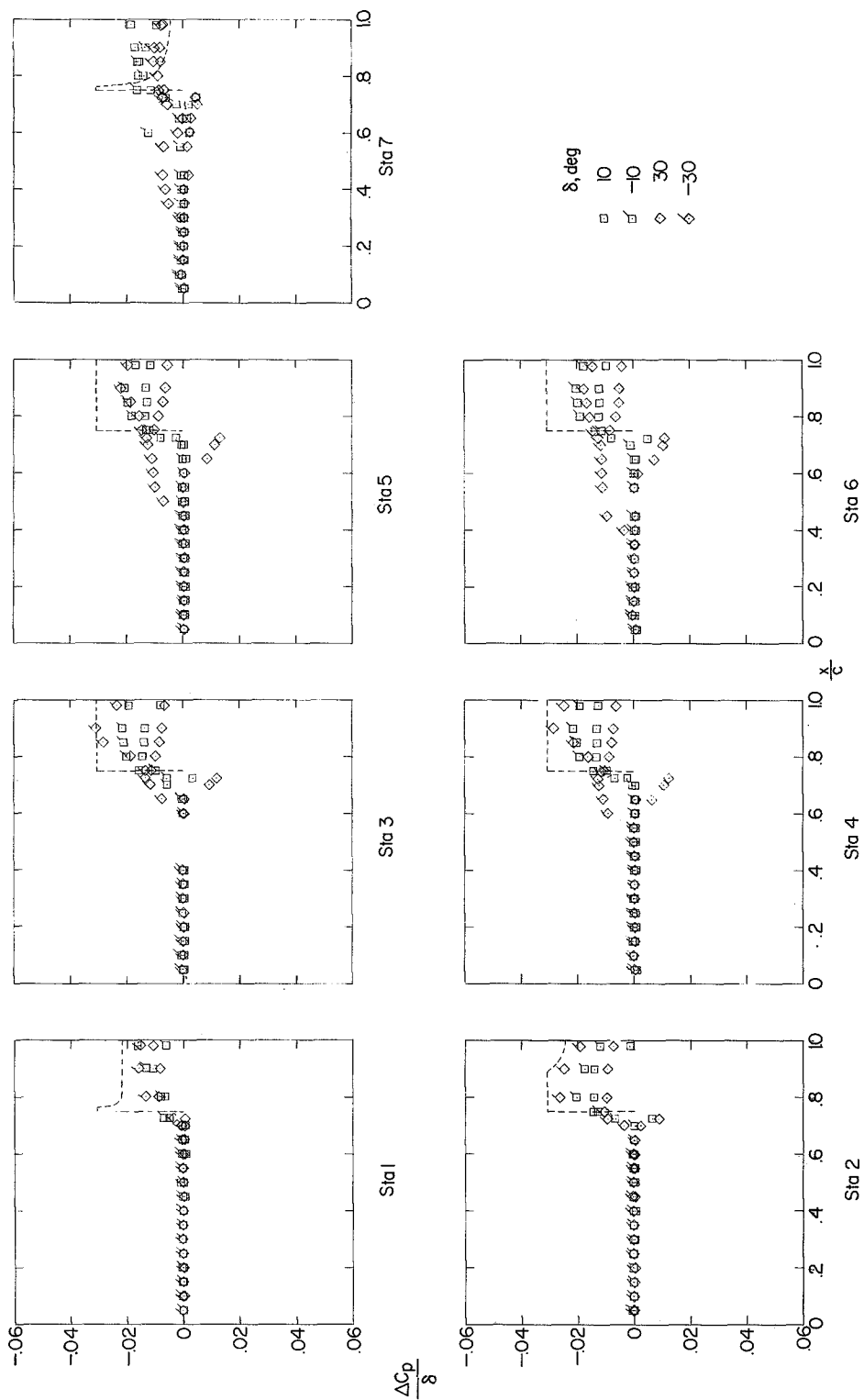
(a) $\alpha = -12^\circ$.

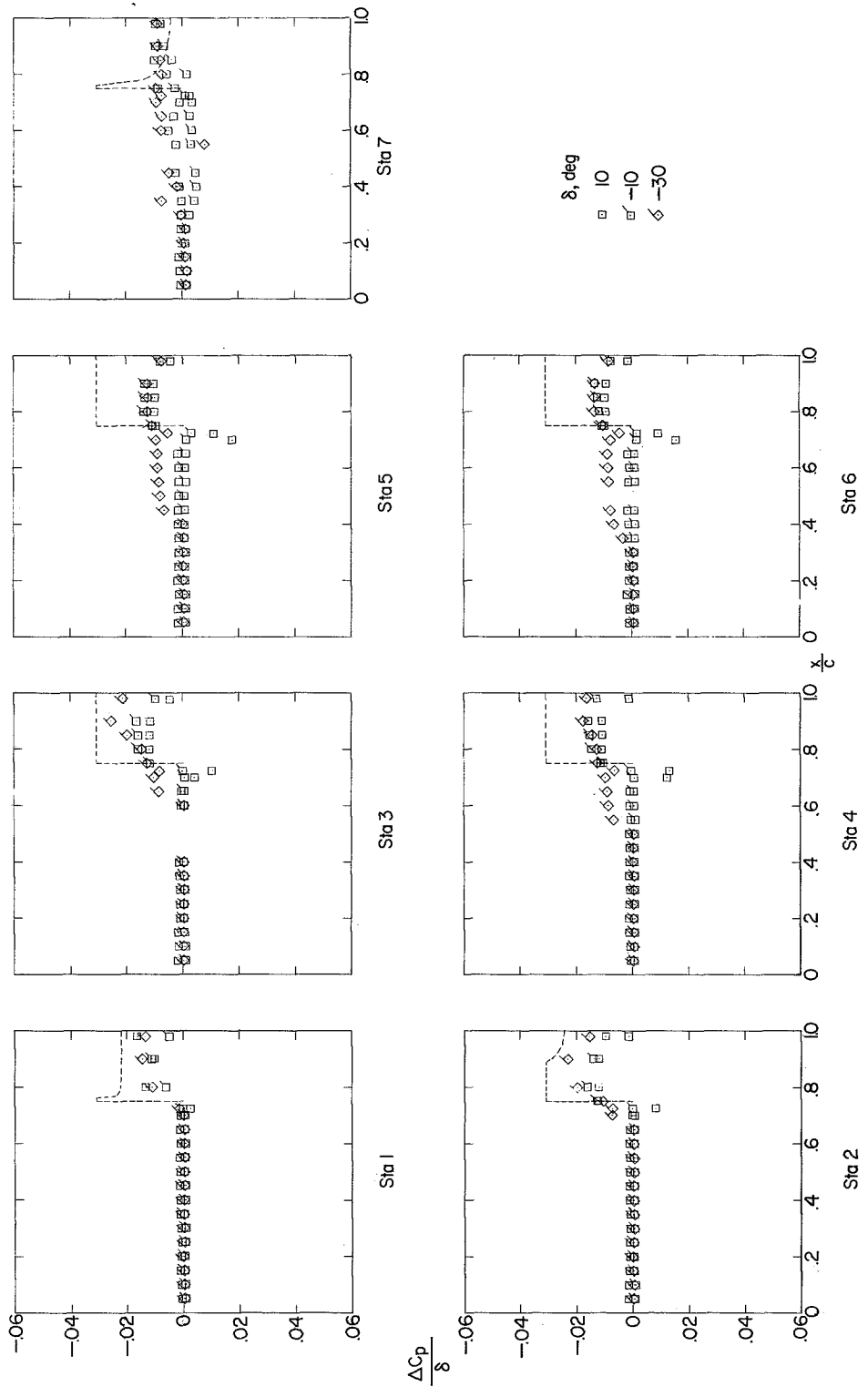
Figure 13.- Incremental upper-surface chordwise pressure distributions due to control deflection for configuration 1. Dashed lines indicate linear-theory predictions. $M = 1.61$;
 $R = 3.6 \times 10^6$.



(b) $\alpha = -6^\circ$.

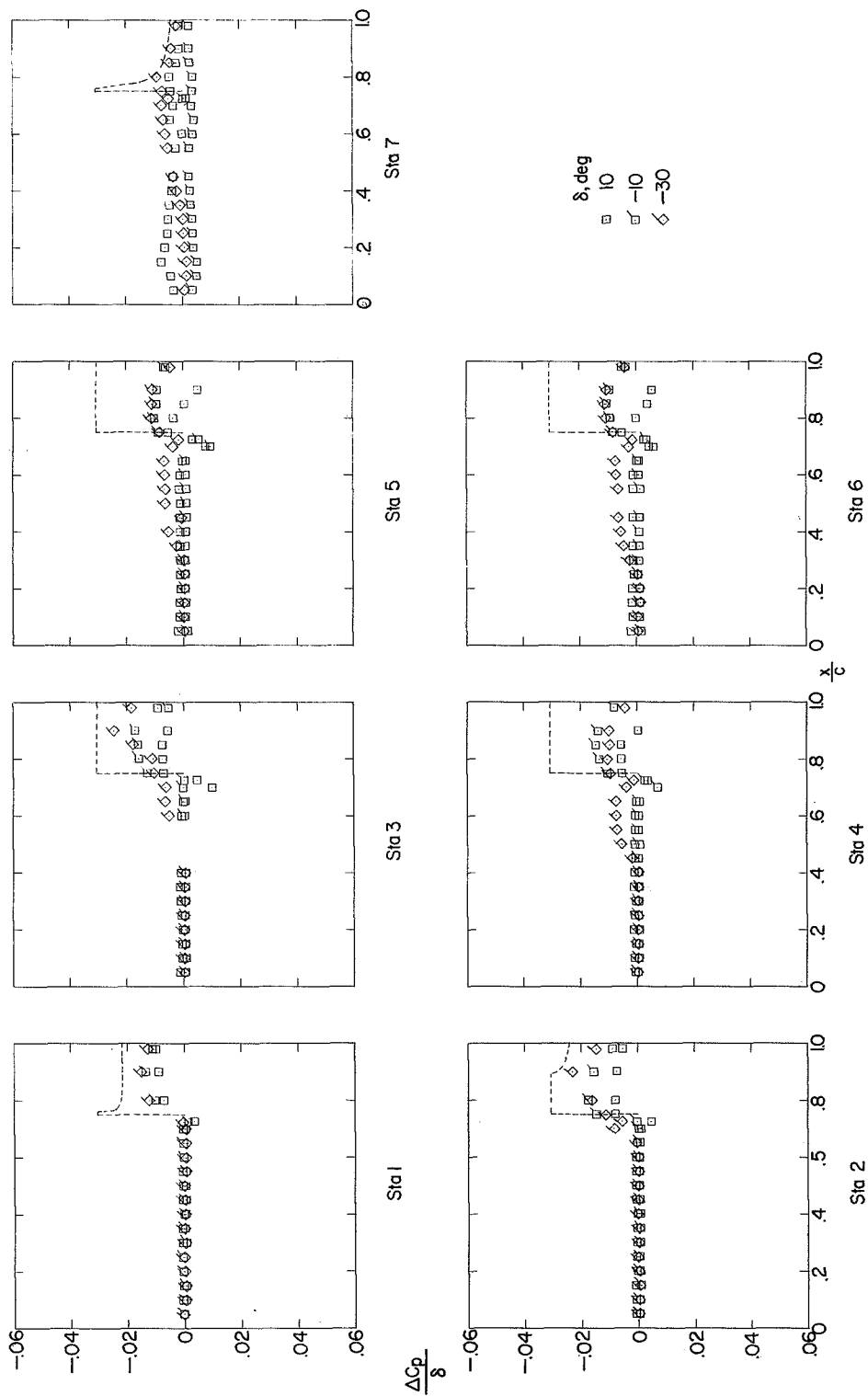
Figure 13.- Continued.





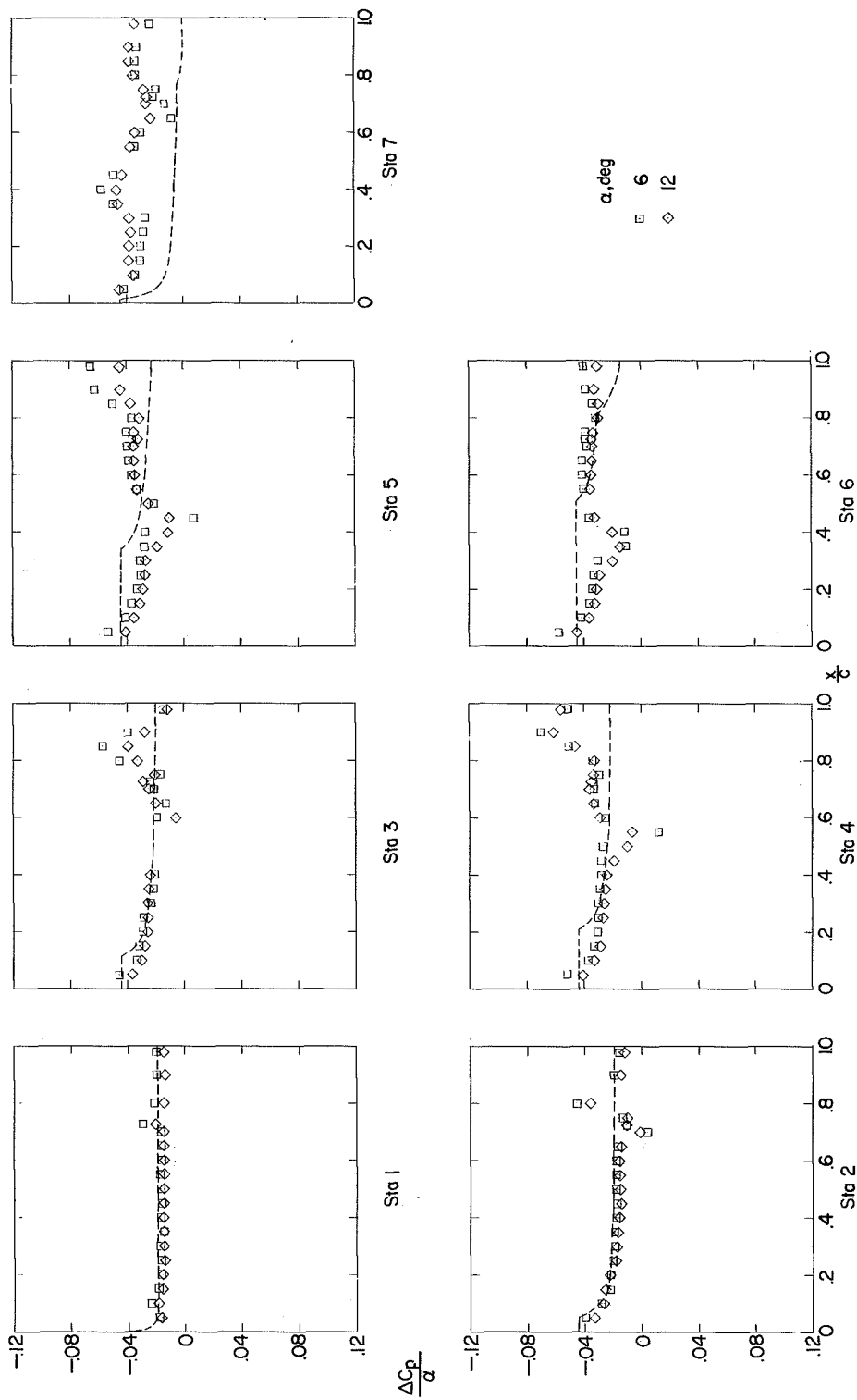
(d) $\alpha = 6^\circ$.

Figure 13.- Continued.



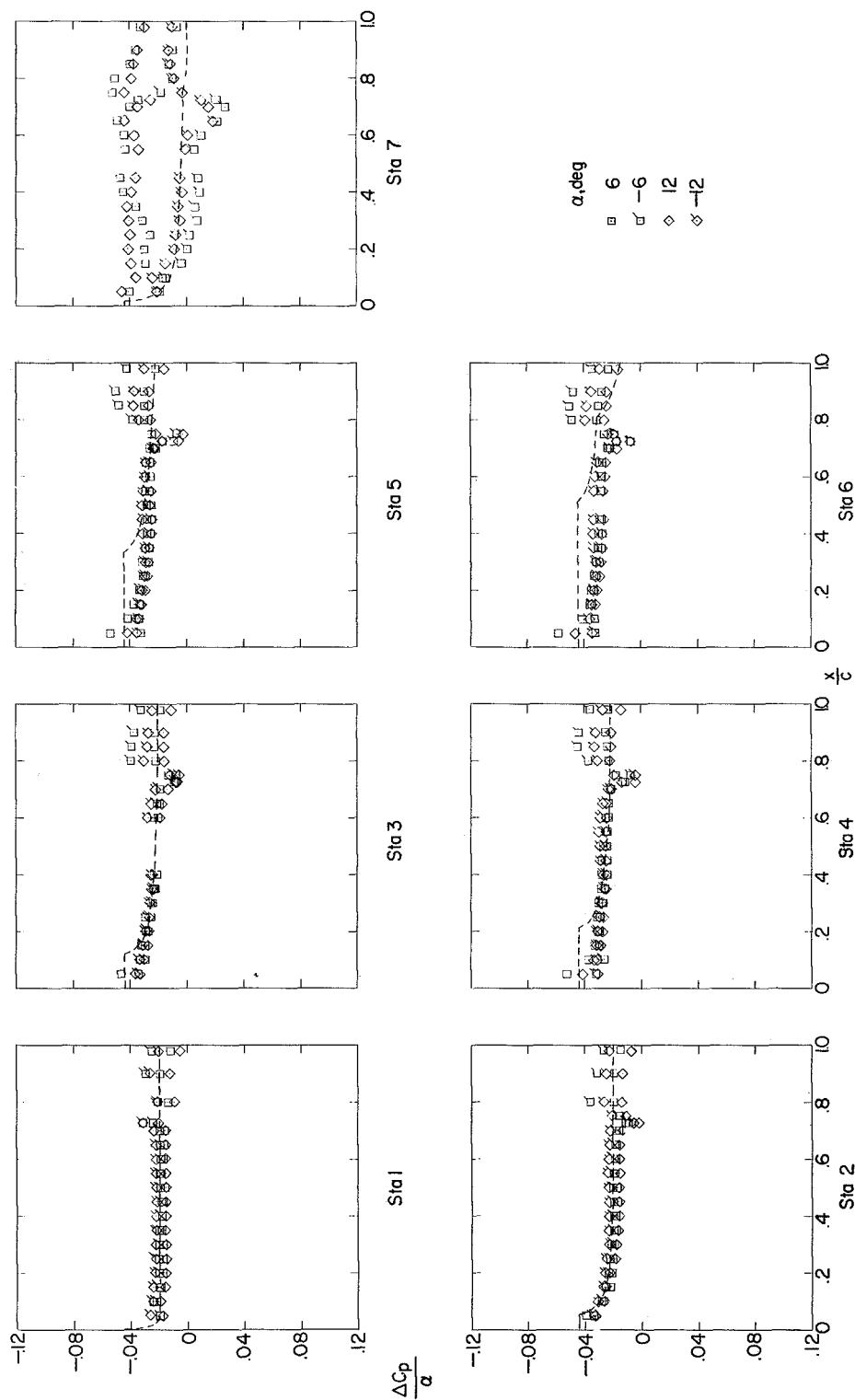
(e) $\alpha = 12^\circ$.

Figure 13.- Concluded.



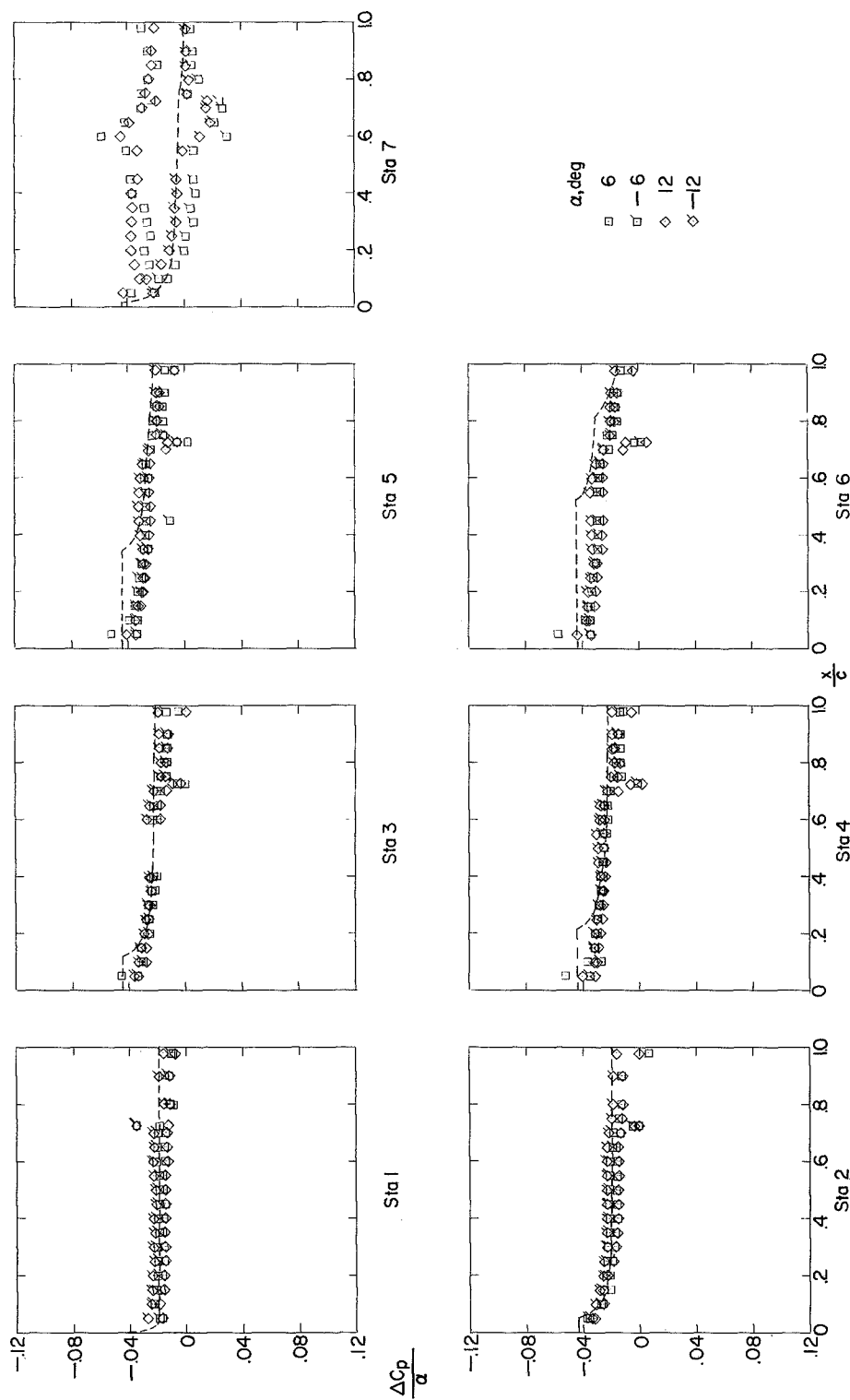
(a) $\delta = -30^\circ$.

Figure 14.- Incremental upper-surface chordwise pressure distributions due to angle of attack for configuration 1. Dashed lines indicate linear-theory predictions. $M = 1.61$; $R = 3.6 \times 10^6$.



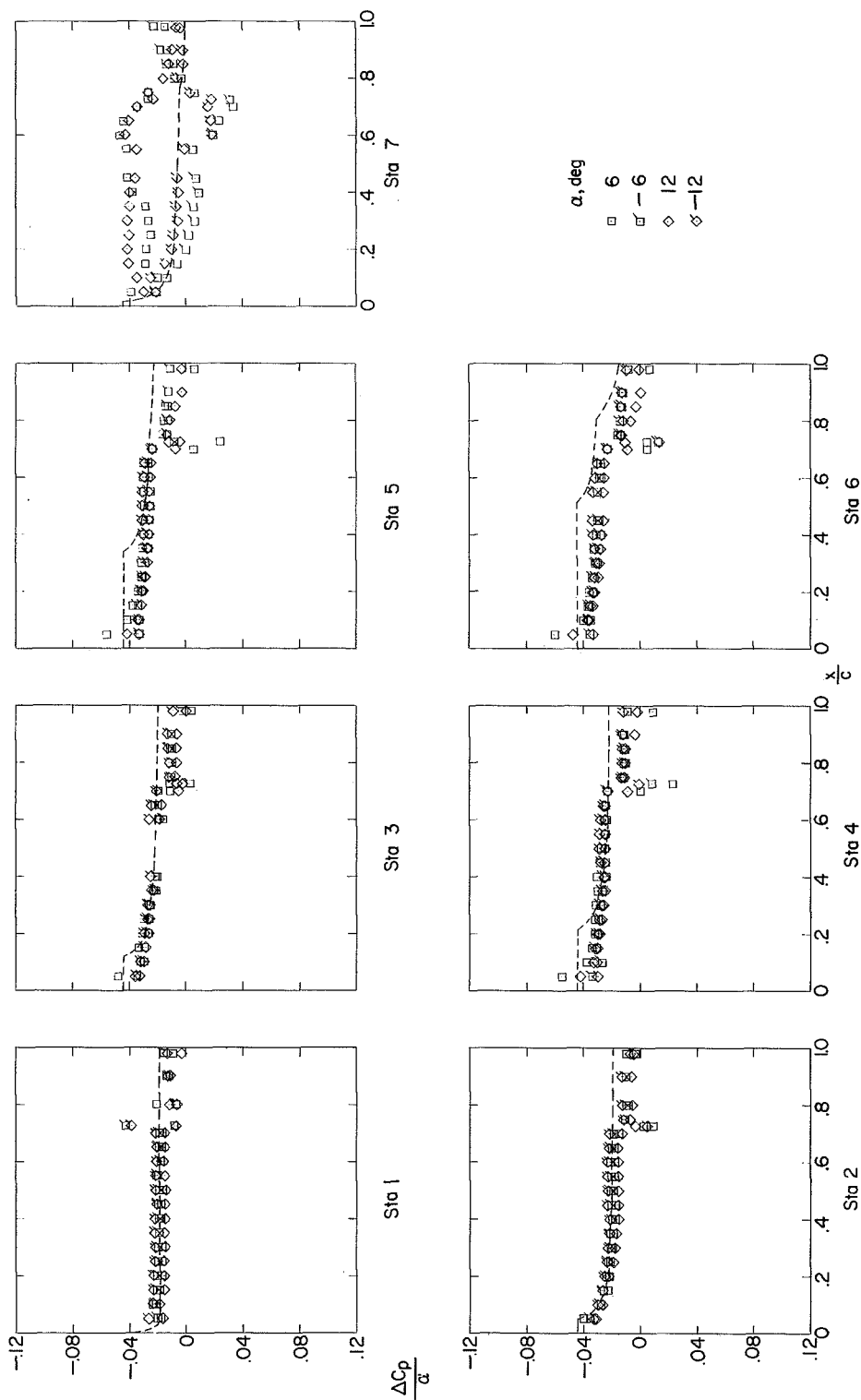
(b) $\delta = -10^\circ$.

Figure 14.- Continued.



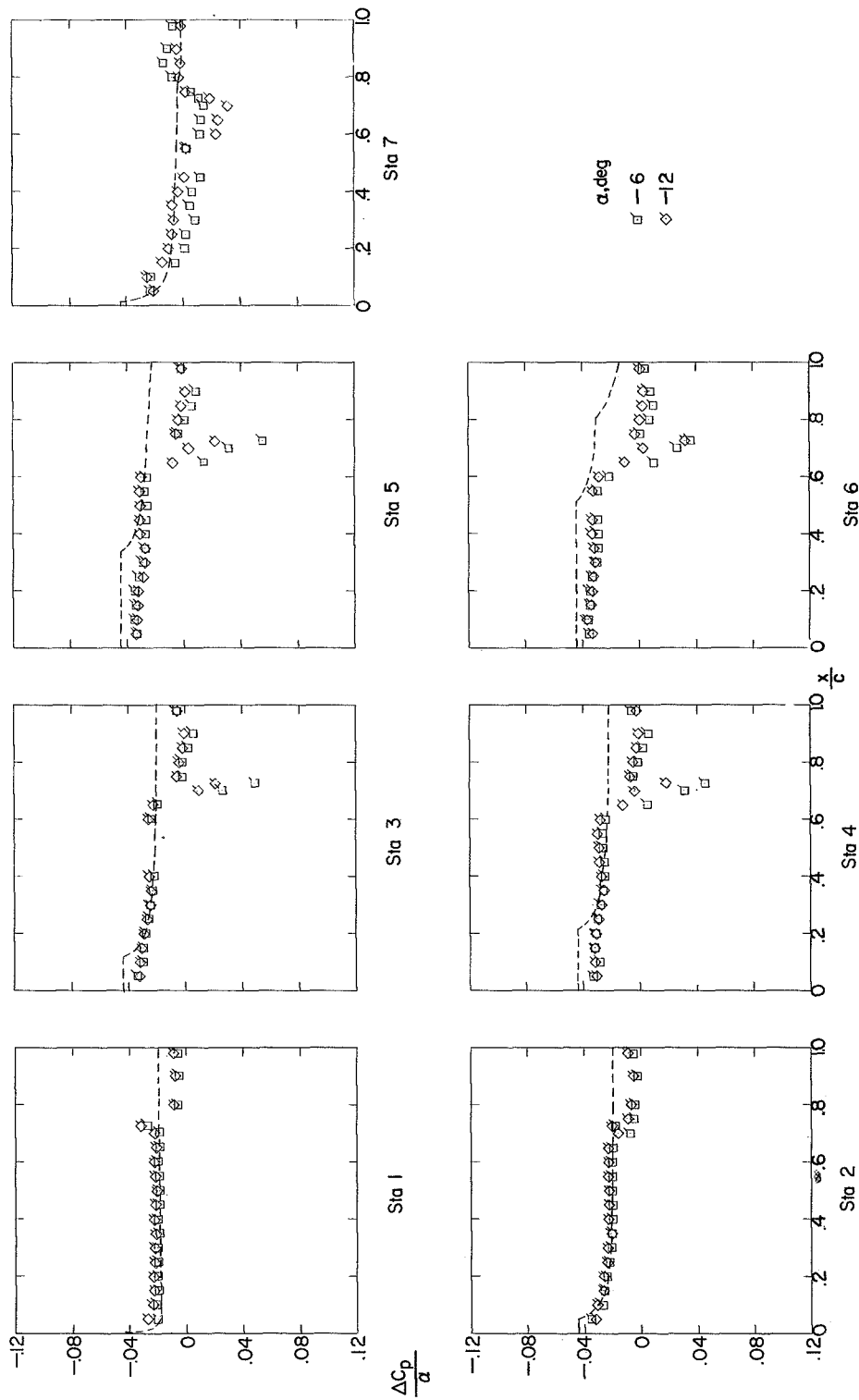
(c) $\delta = 0^\circ$.

Figure 14.- Continued.



(d) $\delta = 10^\circ$.

Figure 14.- Continued.



(e) $\delta = 30^\circ$.

Figure 14.- Concluded.

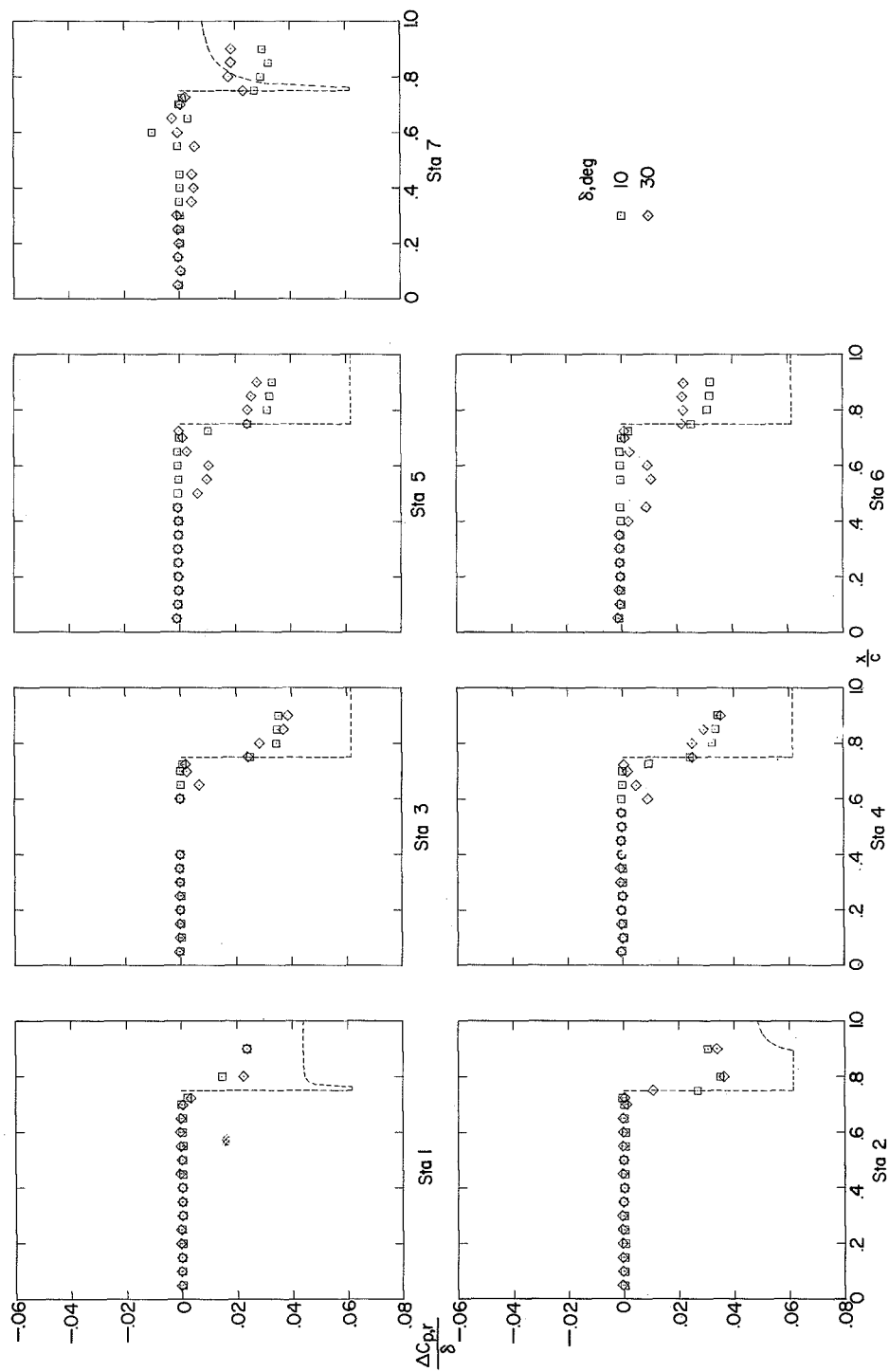
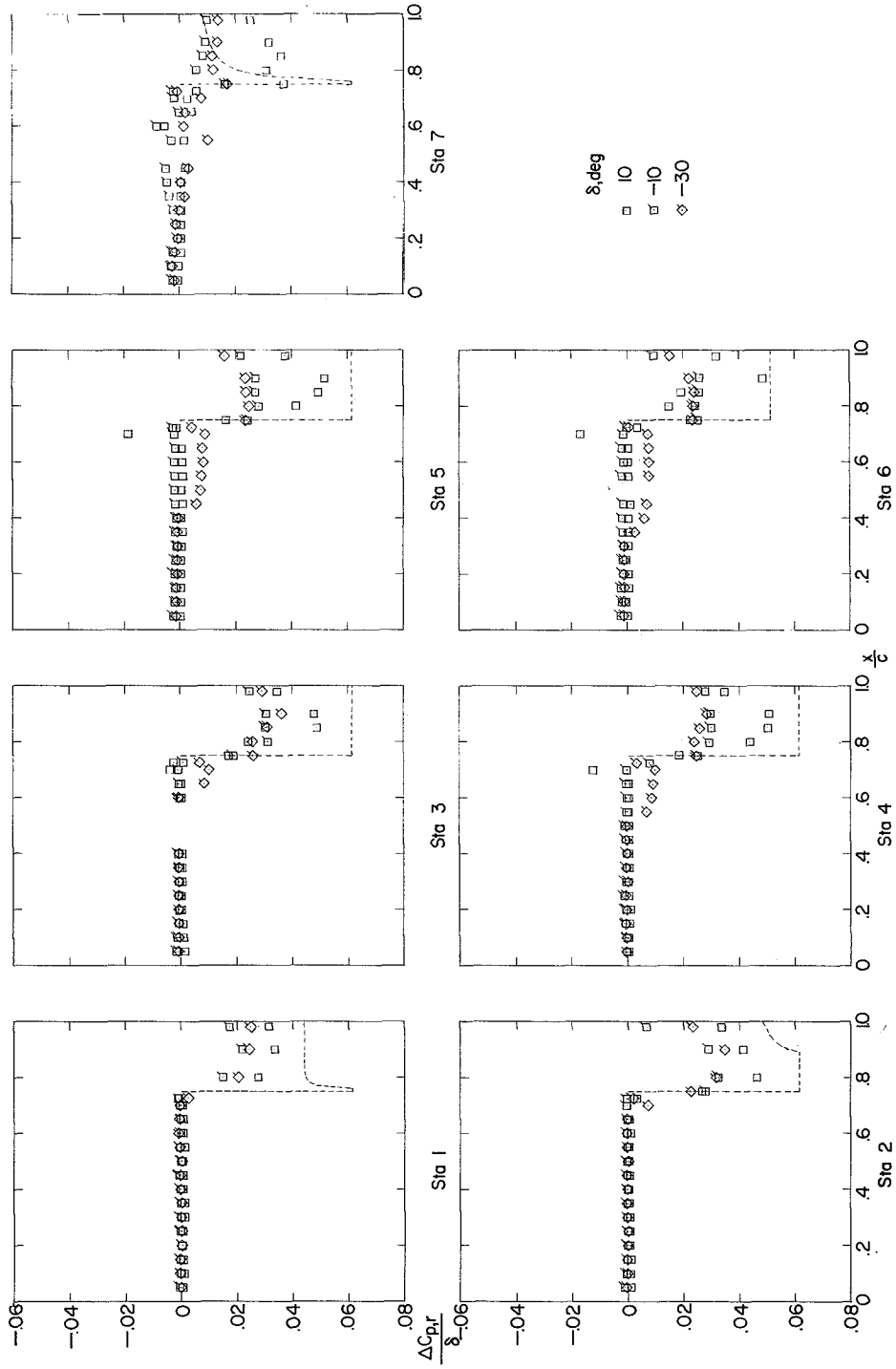
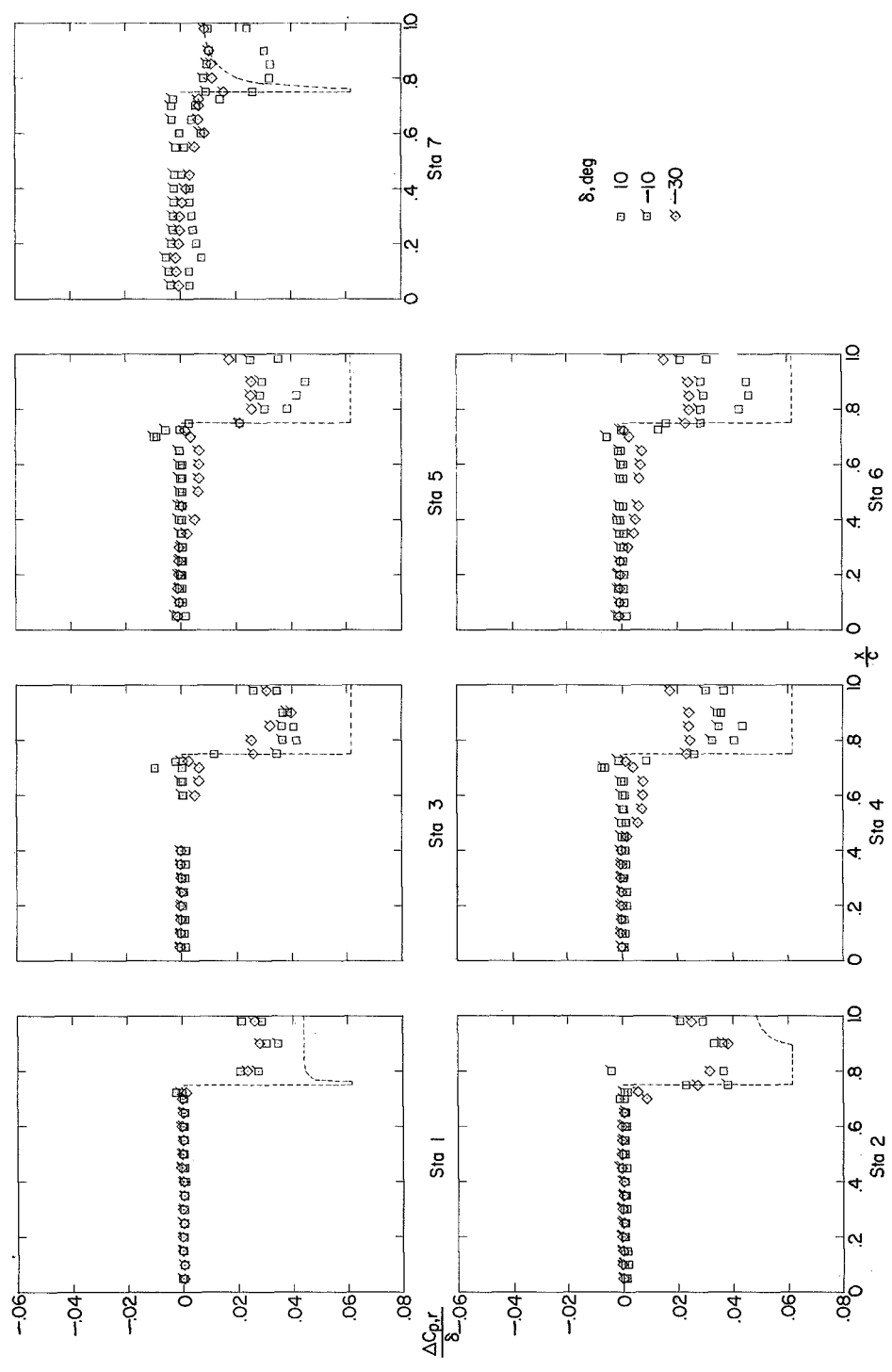


Figure 15.- Incremental resultant chordwise pressure distributions due to control deflection for configuration 1. Dashed lines indicate linear-theory predictions. $M = 1.61$; $R = 3.6 \times 10^6$.



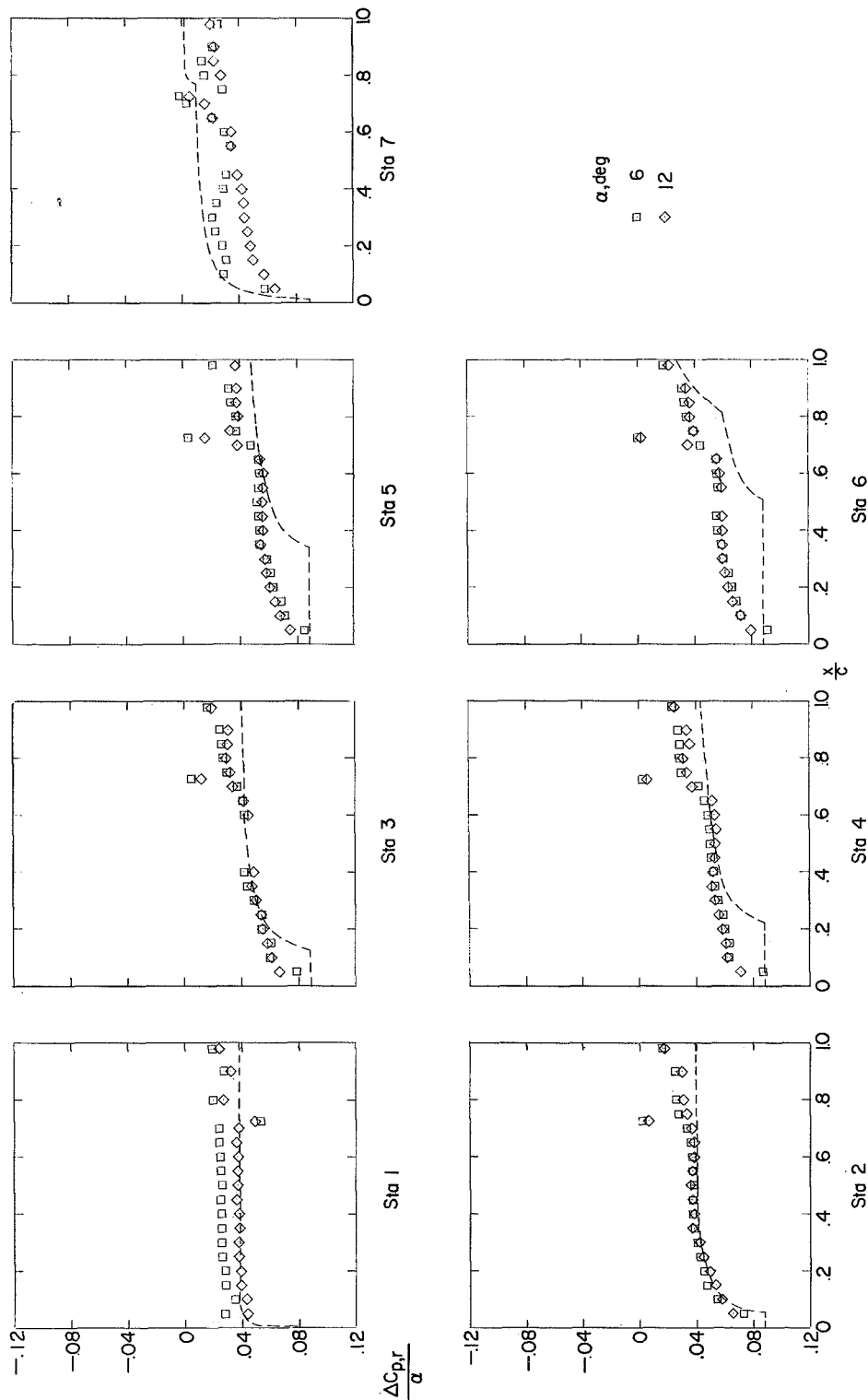
(b) $\alpha = 6^\circ$.

Figure 15.- Continued.



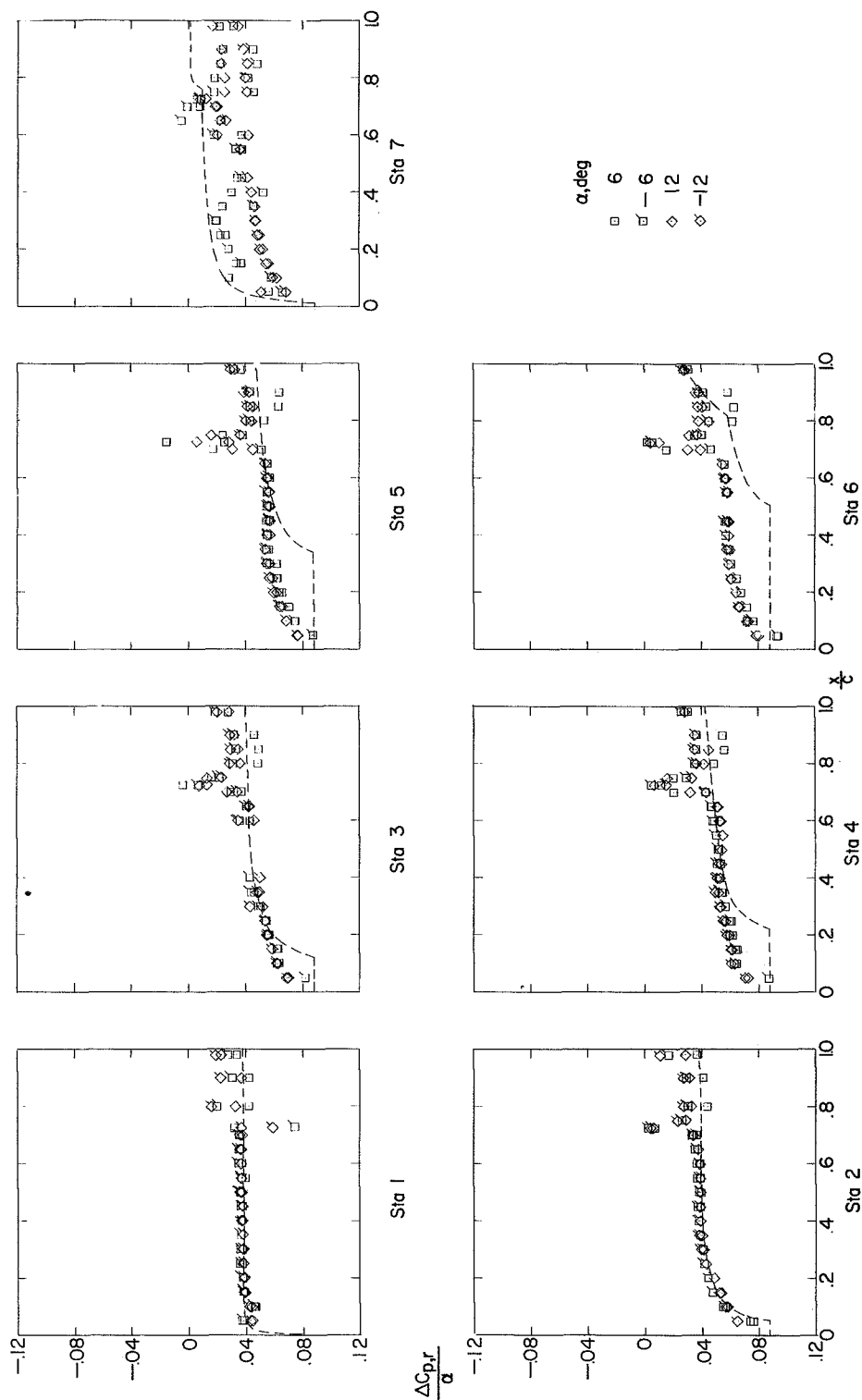
(c) $\alpha = 12^\circ$.

Figure 15.- Concluded.



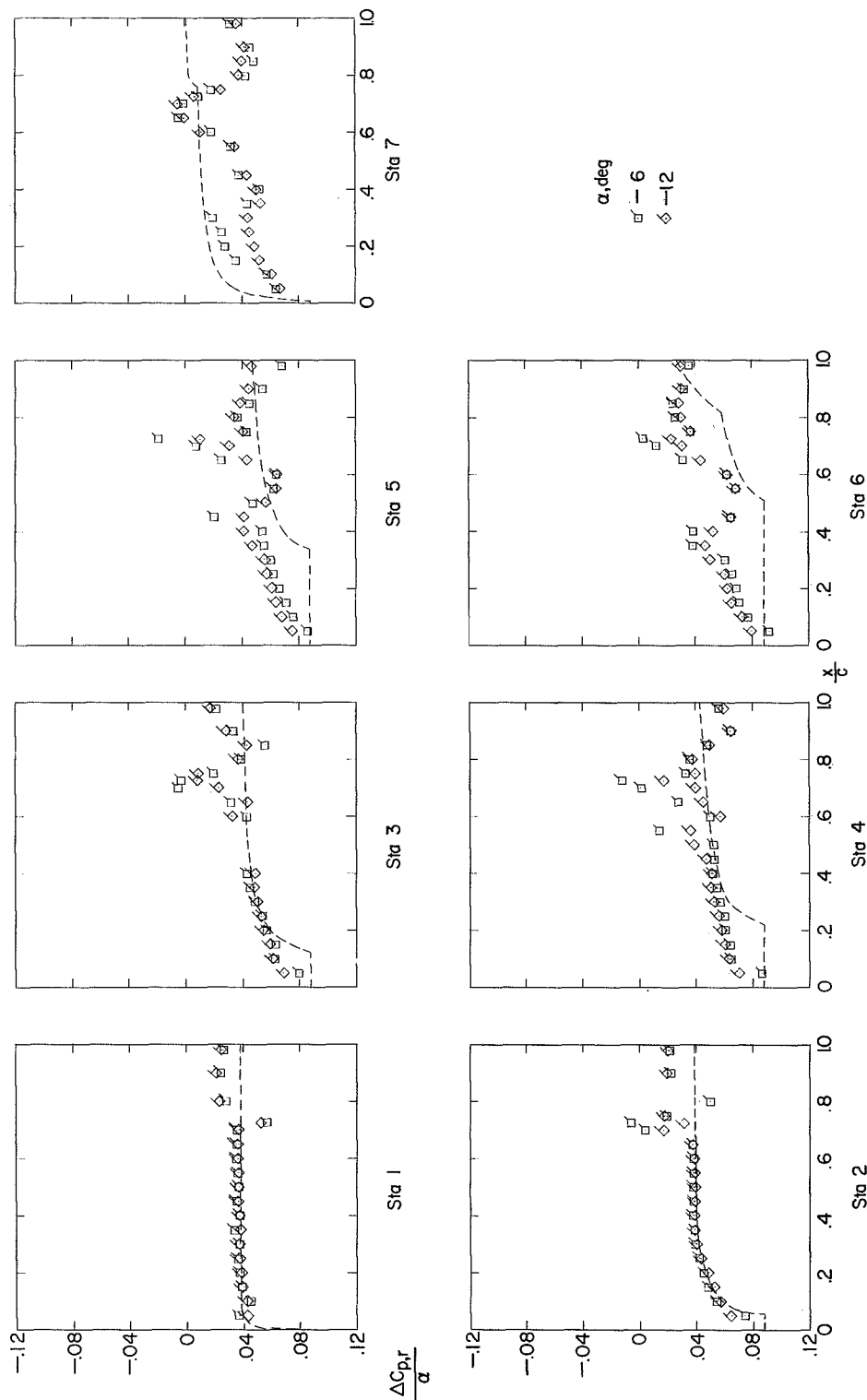
(a) $\delta = 0^\circ$.

Figure 16.- Incremental resultant chordwise pressure distributions due to angle of attack for configuration 1. Dashed lines indicate linear-theory predictions. $M = 1.61$; $R = 3.6 \times 10^6$.



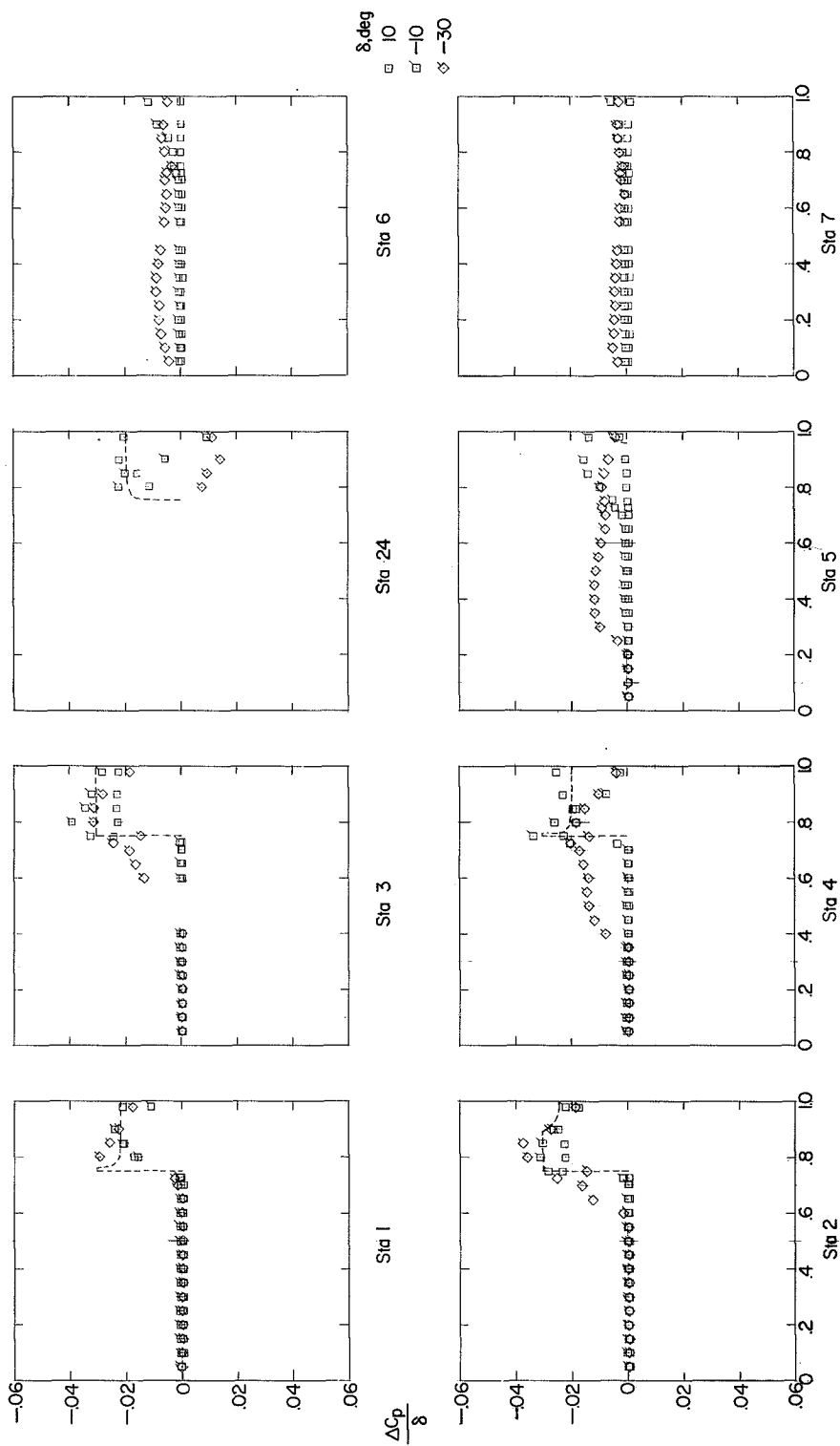
(b) $\delta = 10^\circ$.

Figure 16.- Continued.



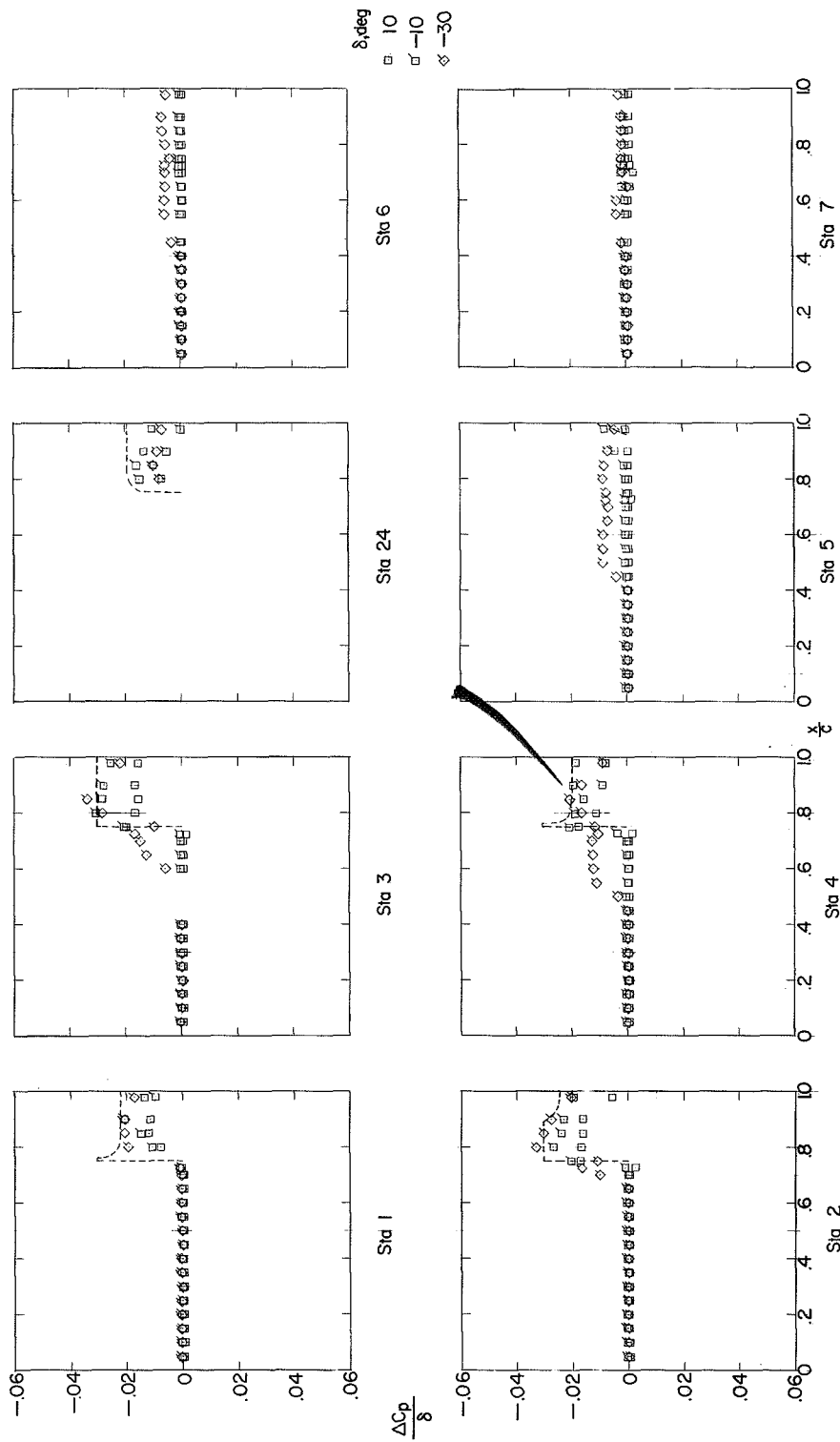
(c) $\delta = 30^\circ$.

Figure 16.- Concluded.



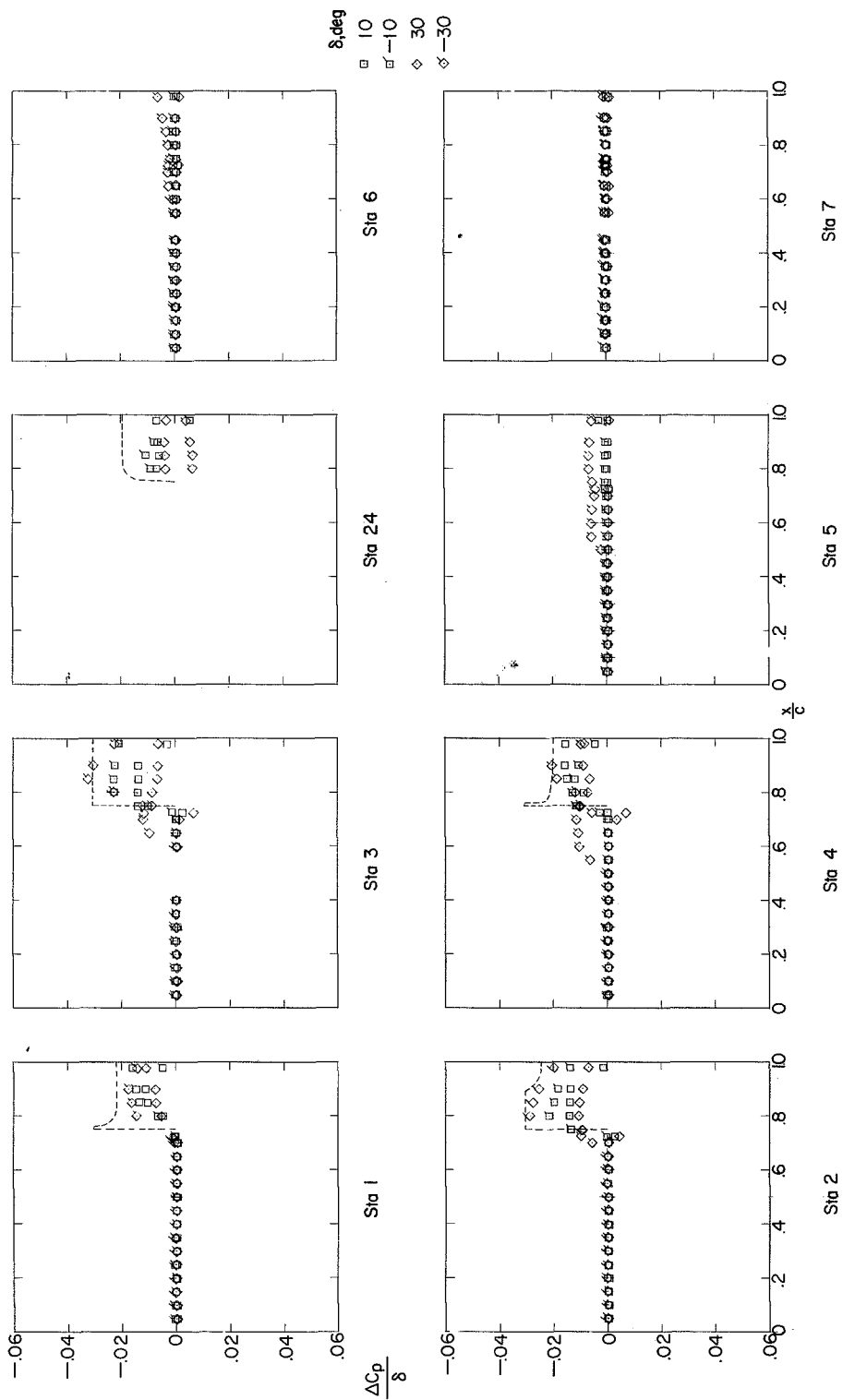
(a) $\alpha = -12^\circ$.

Figure 17.- Incremental upper-surface chordwise pressure distributions due to control deflection for configuration 3. Dashed lines indicate linear-theory predictions. $M = 1.61$;
 $R = 3.6 \times 10^6$.



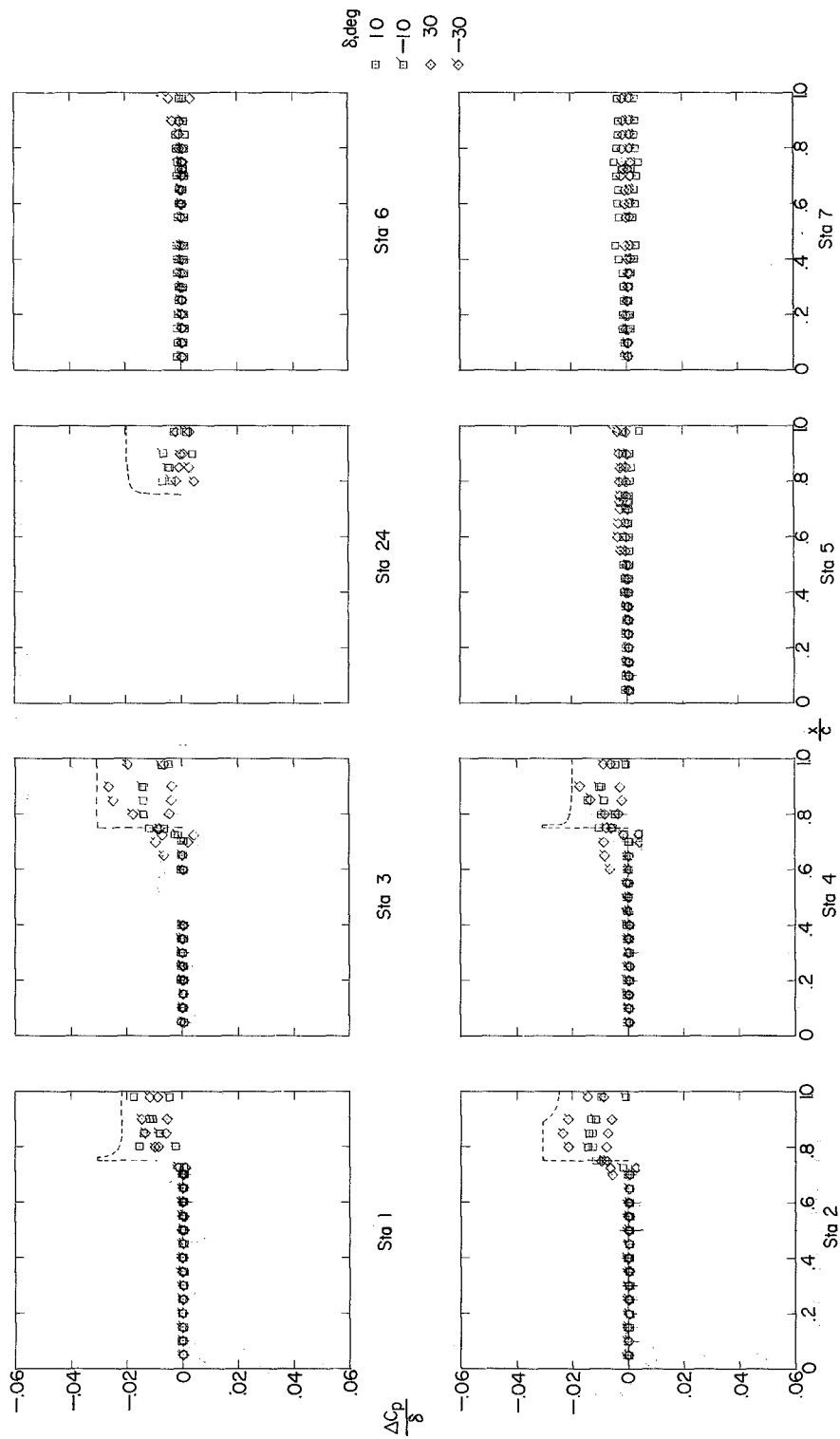
(b) $\alpha = -6^\circ$.

Figure 17.- Continued.



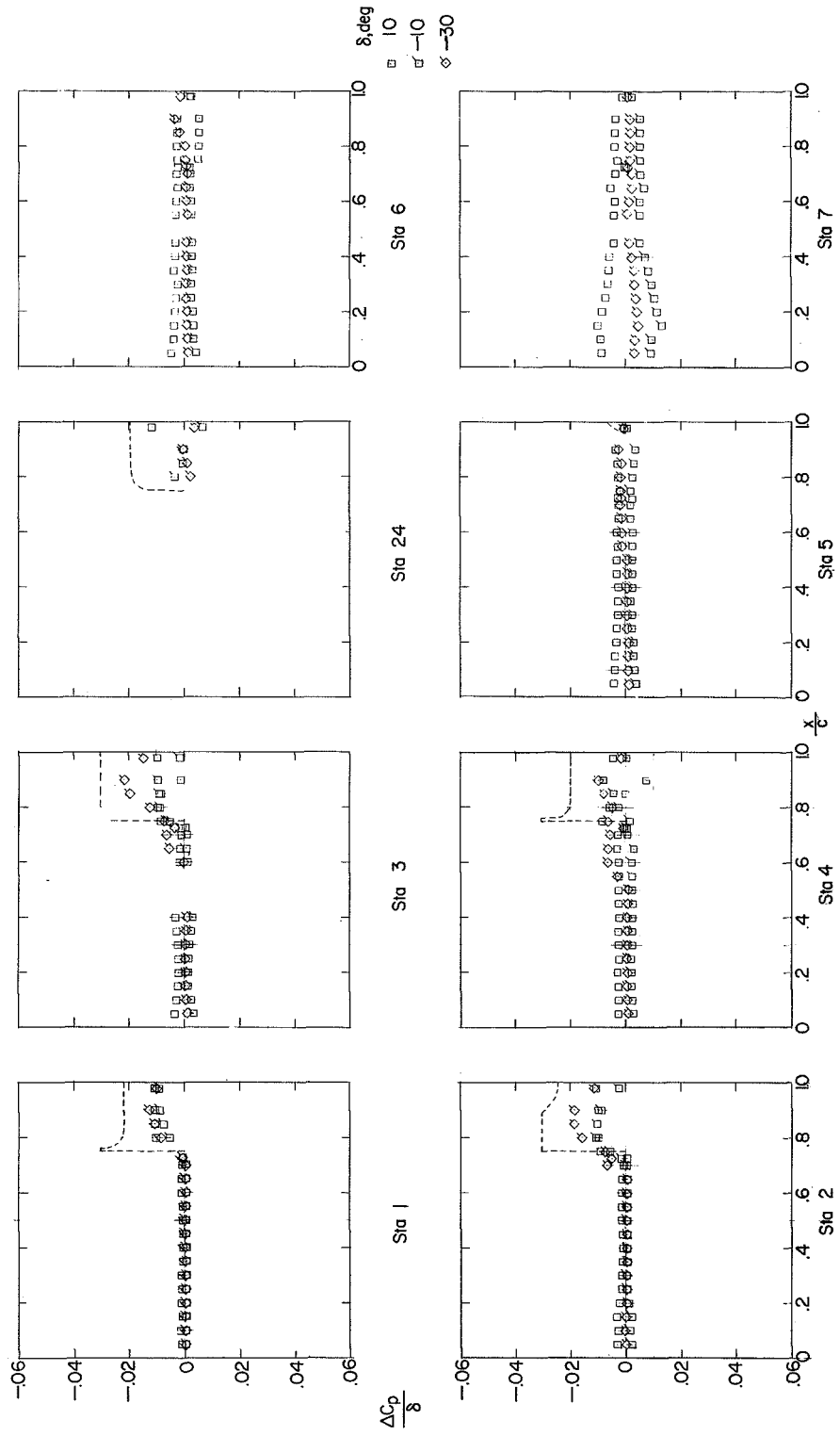
(c) $\alpha = 0^\circ$.

Figure 17.- Continued.



(d) $\alpha = 6^\circ$.

Figure 17.- Continued.



(e) $\alpha = 12^\circ$.

Figure 17.- Concluded.

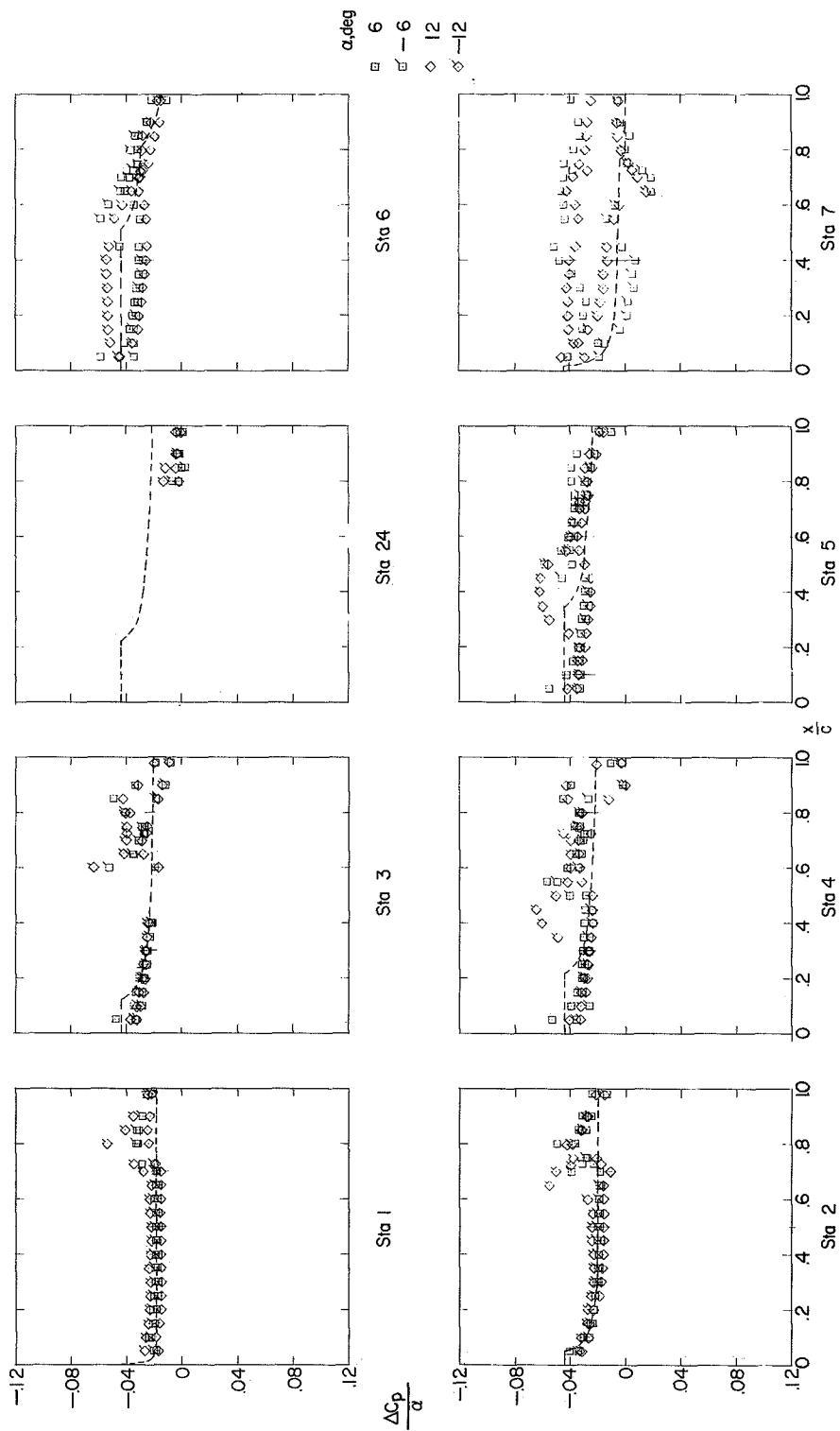
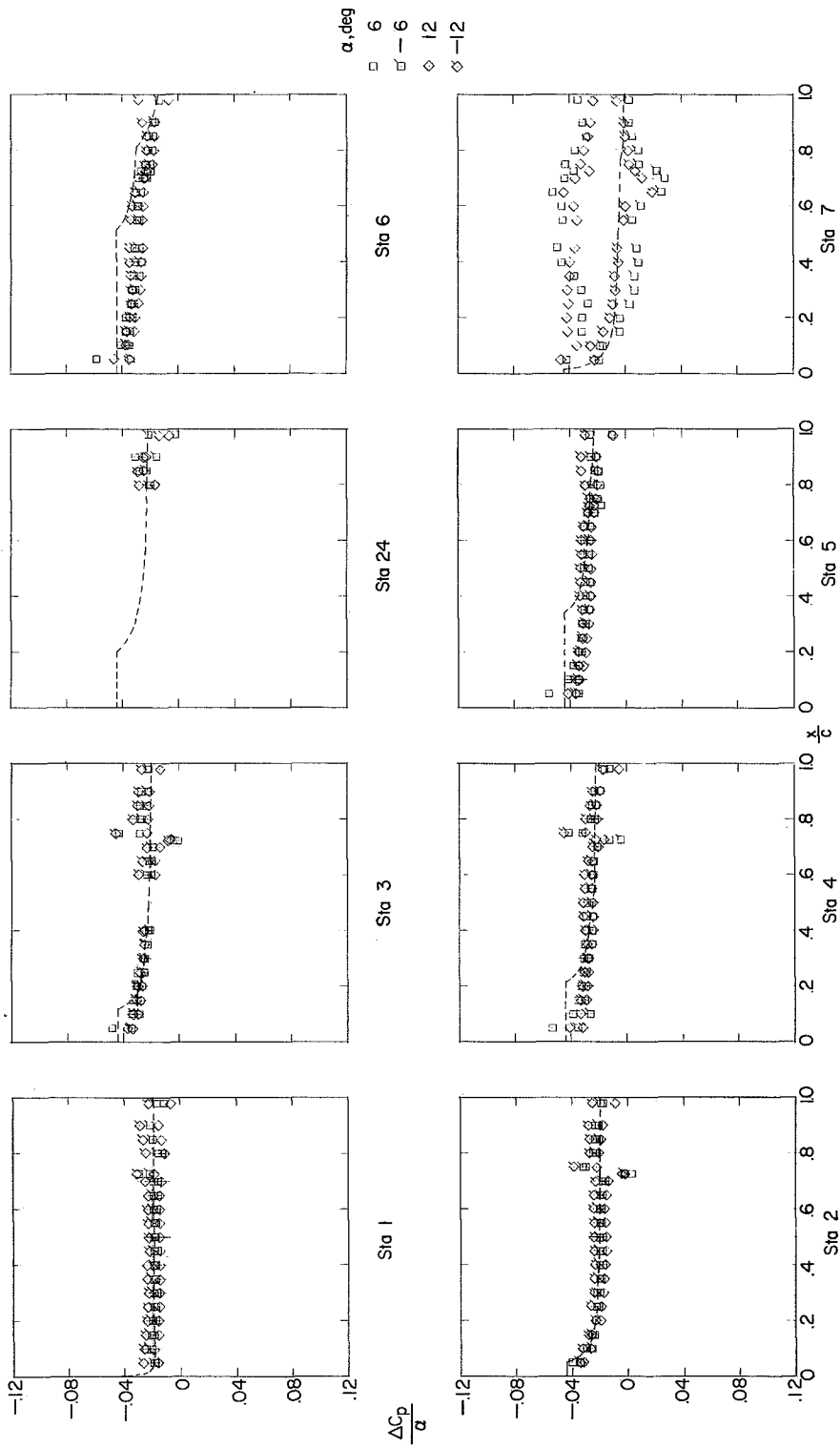
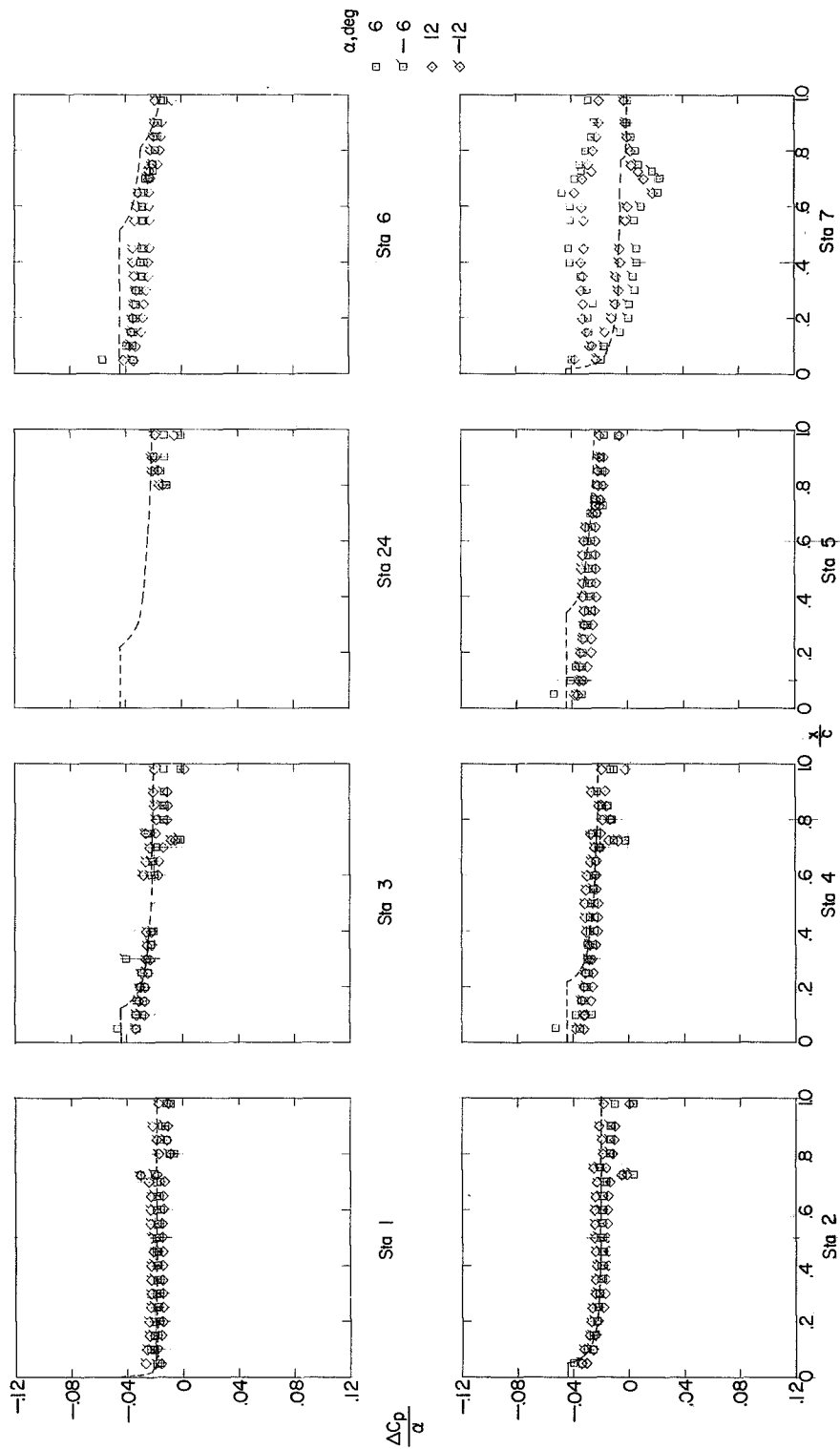


Figure 18.- Incremental upper-surface chordwise pressure distributions due to angle of attack for configuration 3. Dashed lines indicate linear-theory predictions. $M = 1.61$;
 $R = 3.6 \times 10^6$.



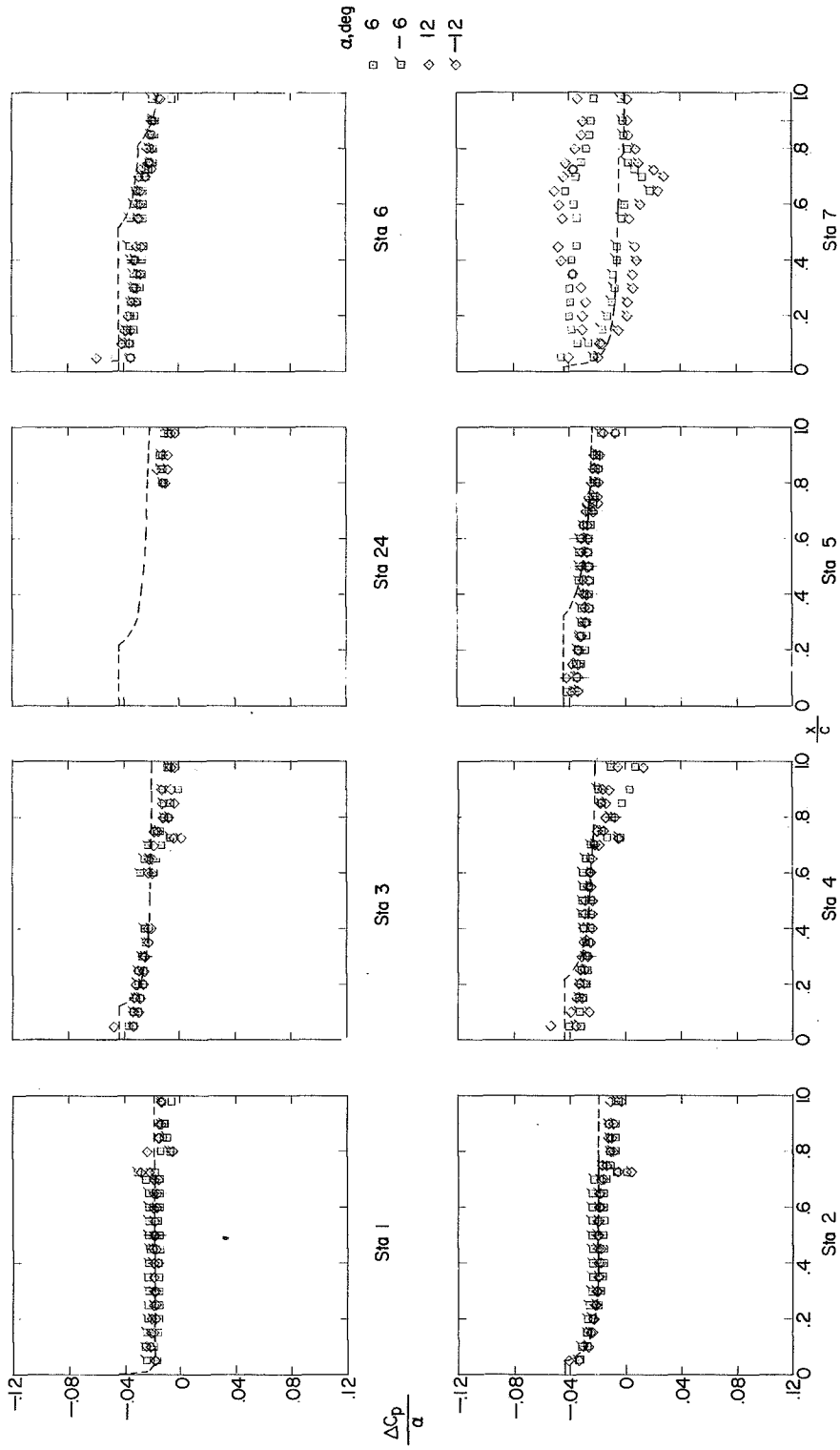
(b) $\delta = -10^\circ$.

Figure 18.- Continued.



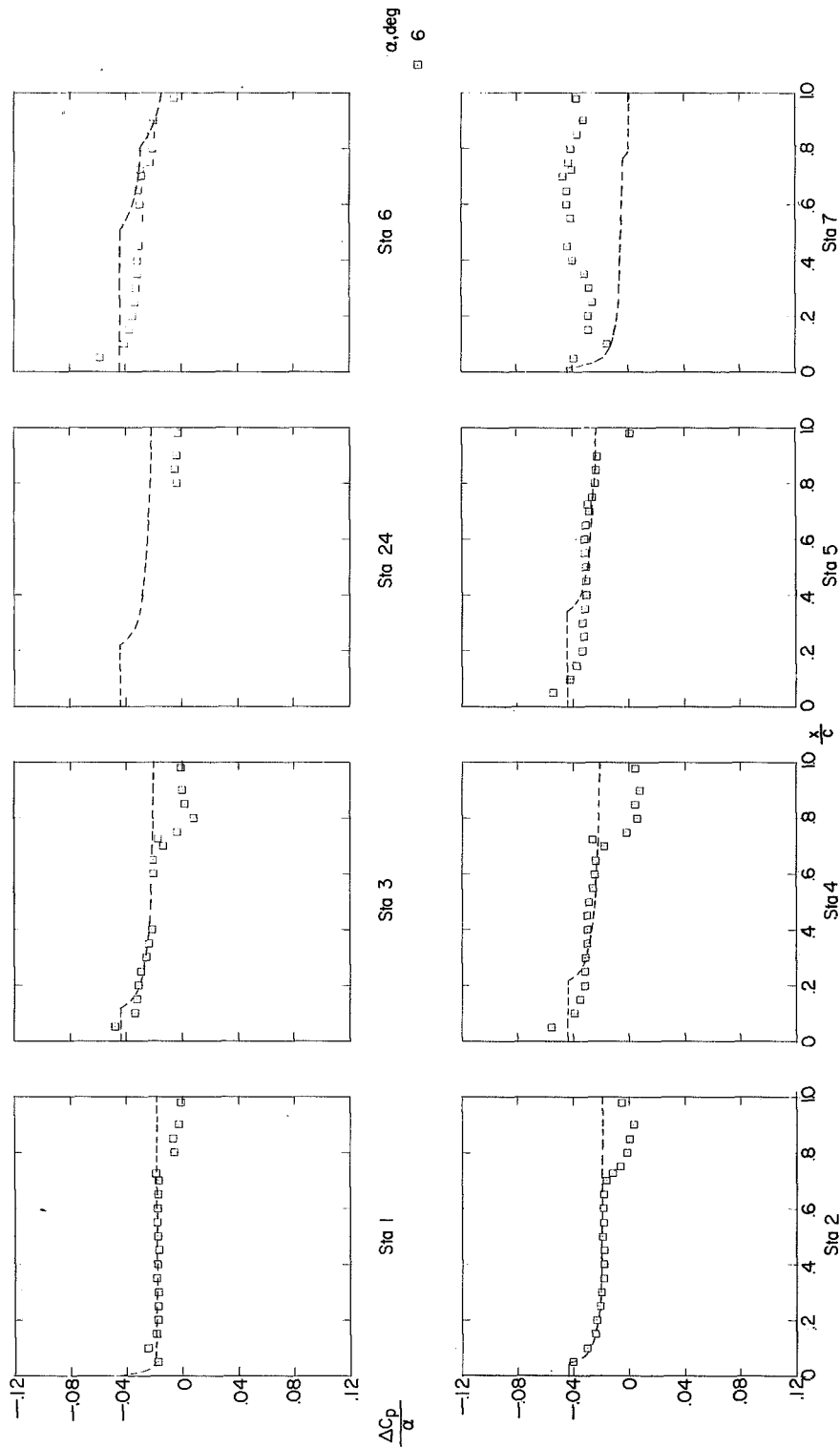
(c) $\delta = 0^\circ$.

Figure 18.- Continued.



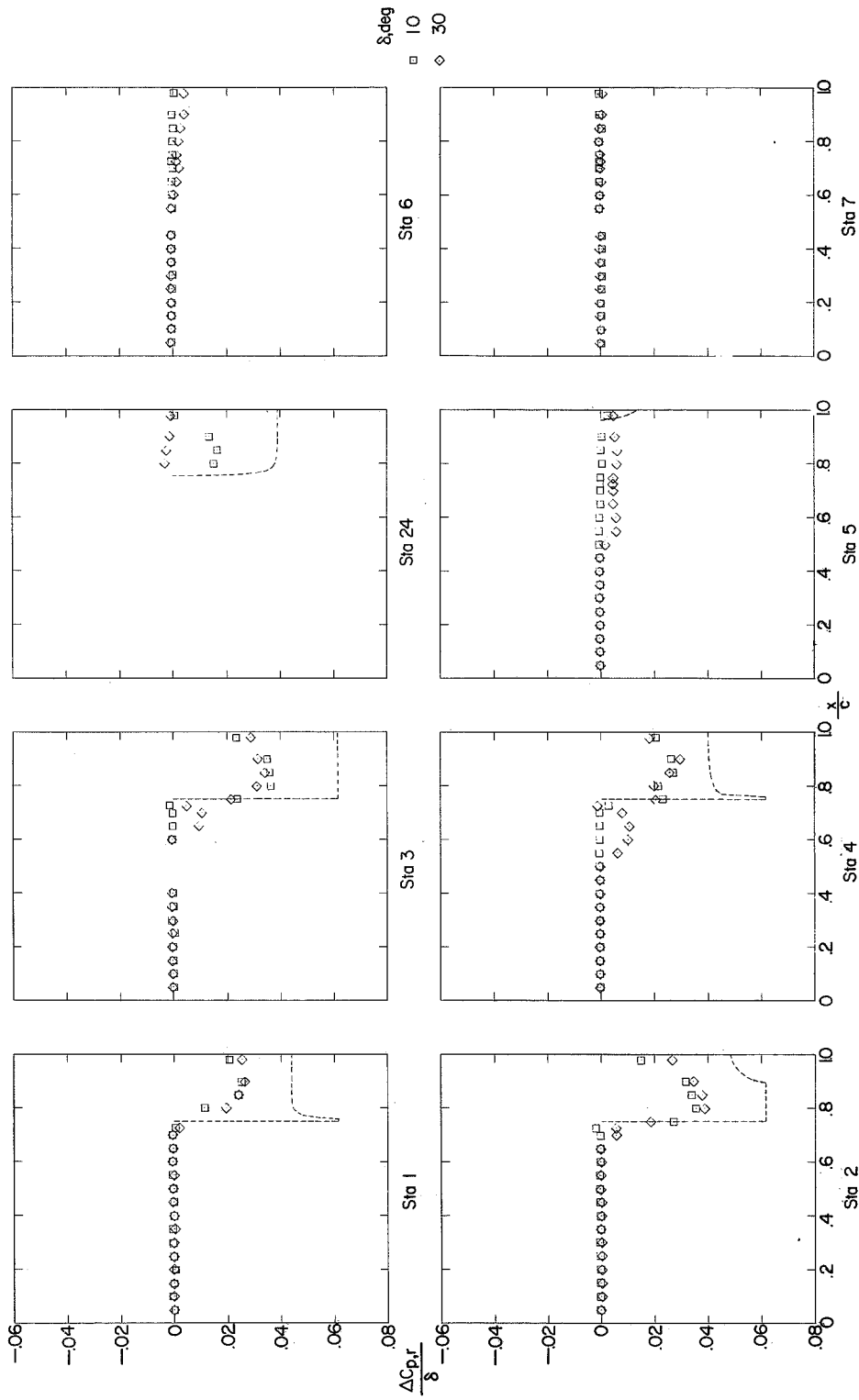
(d) $\delta = 10^\circ$.

Figure 18.- Continued.



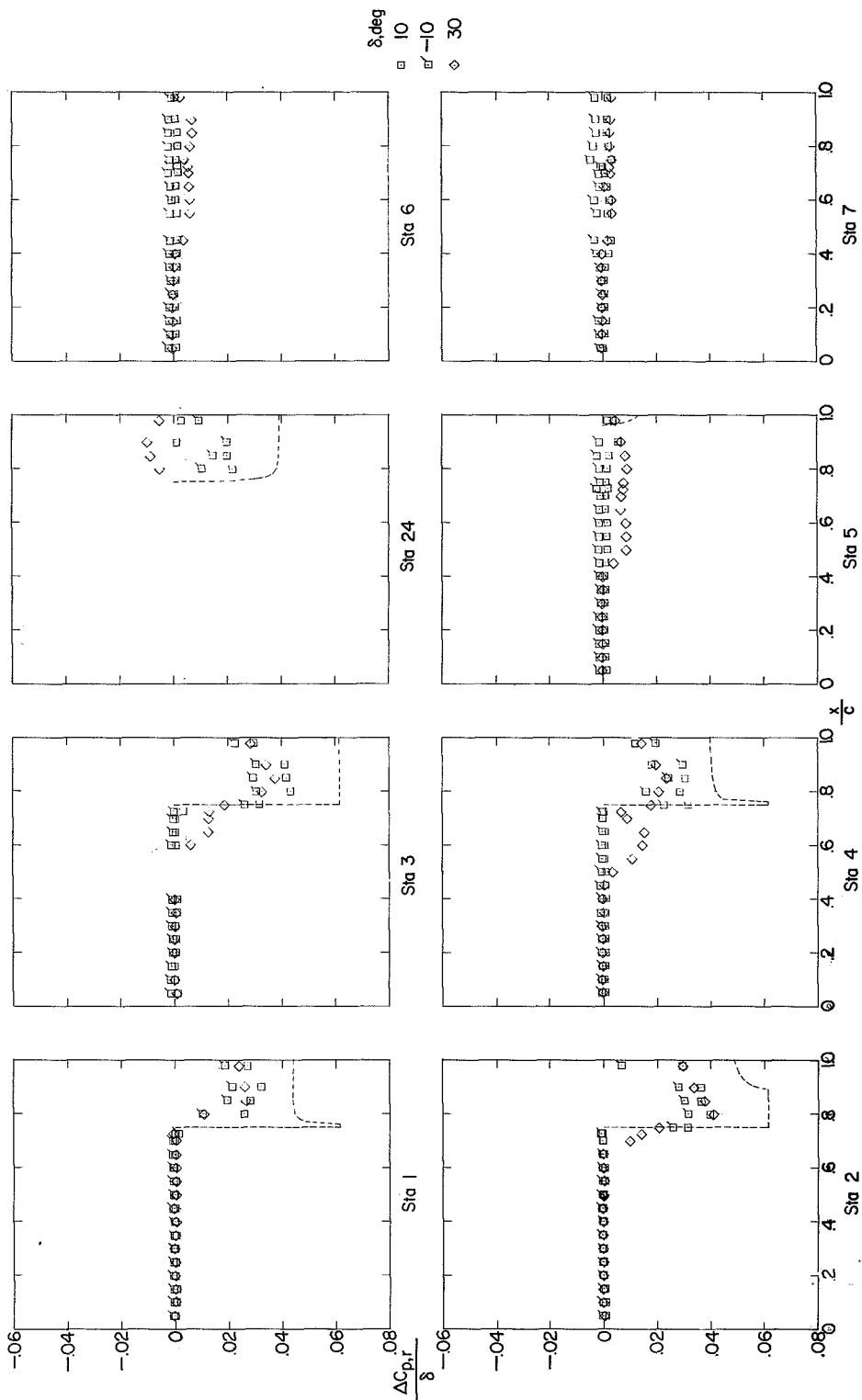
(e) $\delta = 30^\circ$.

Figure 18.- Concluded.



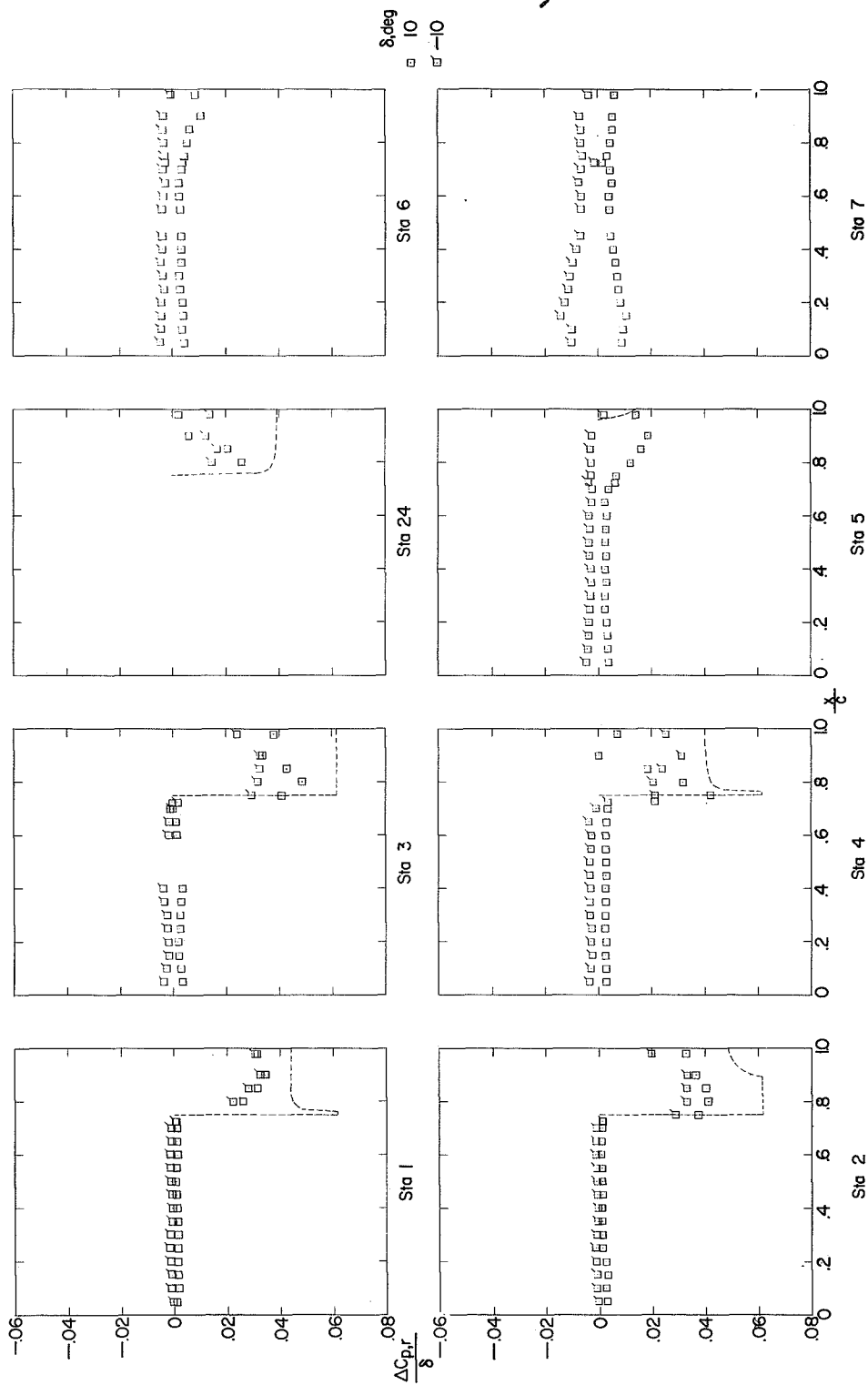
(a) $\alpha = 0^\circ$.

Figure 19.- Incremental resultant chordwise pressure distributions due to control deflection for configuration 3. Dashed lines indicate linear-theory predictions. $M = 1.61$; $R = 3.6 \times 10^6$.



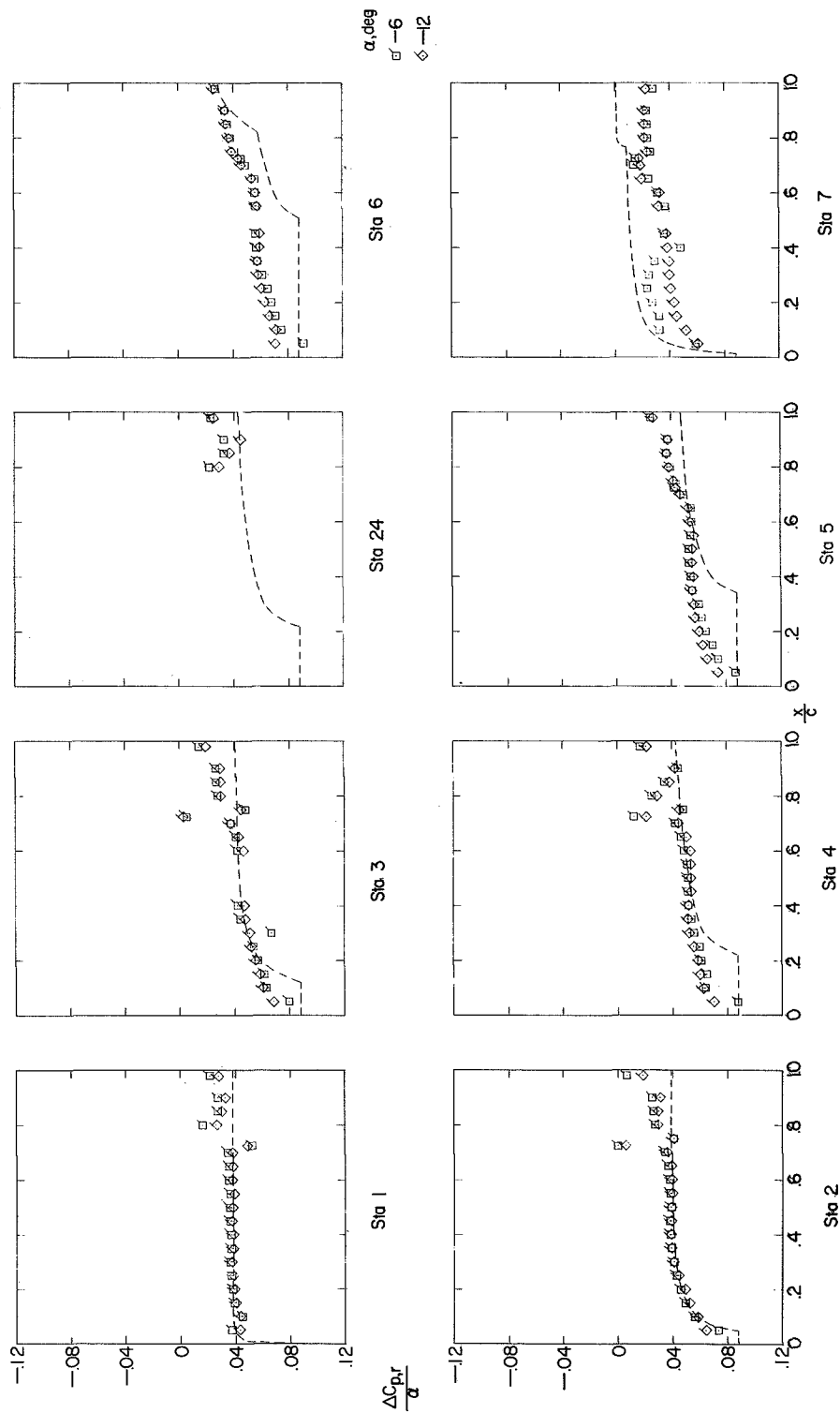
(b) $\alpha = 6^\circ$.

Figure 19.- Continued.



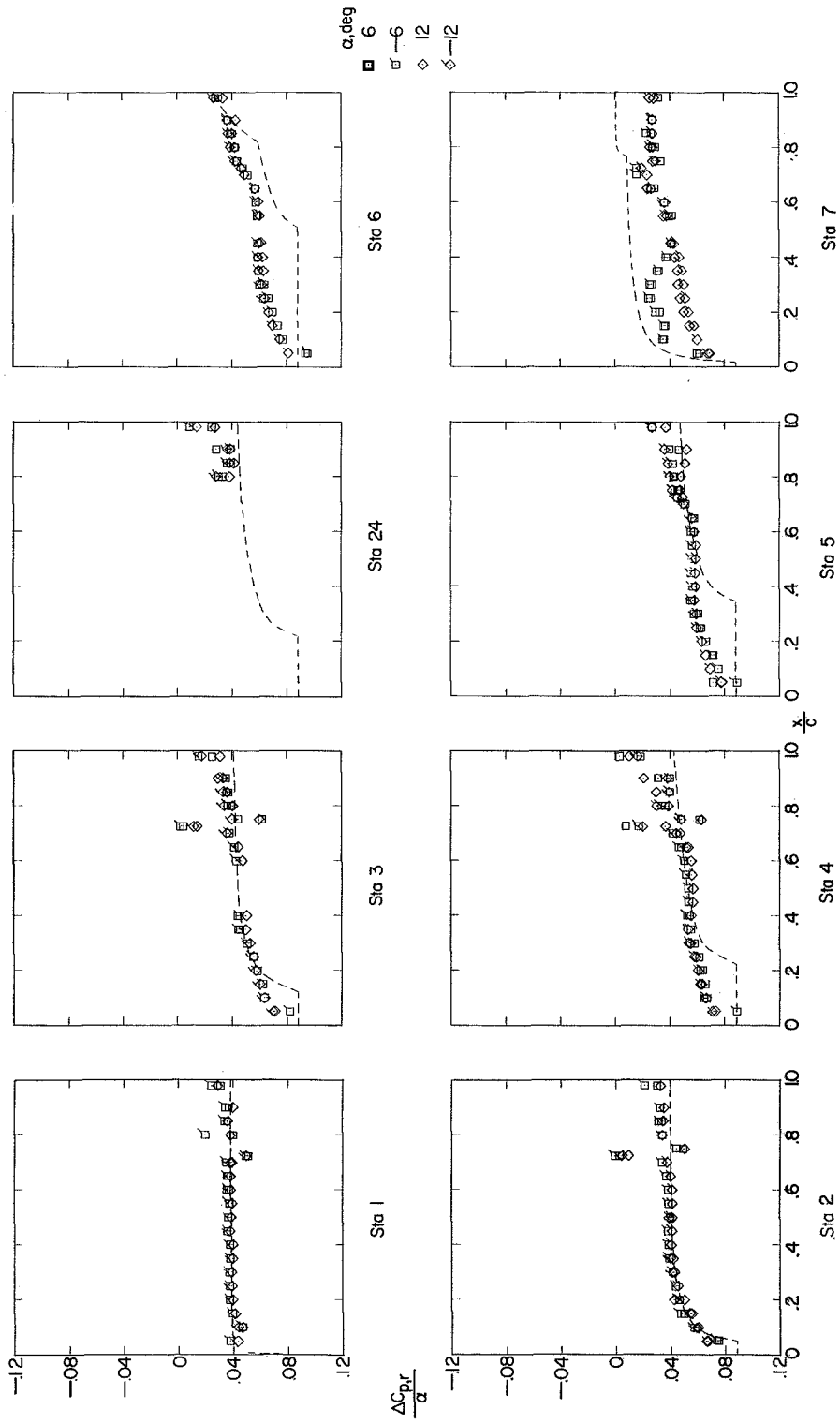
(c) $\alpha = 12^\circ$.

Figure 19.- Concluded.



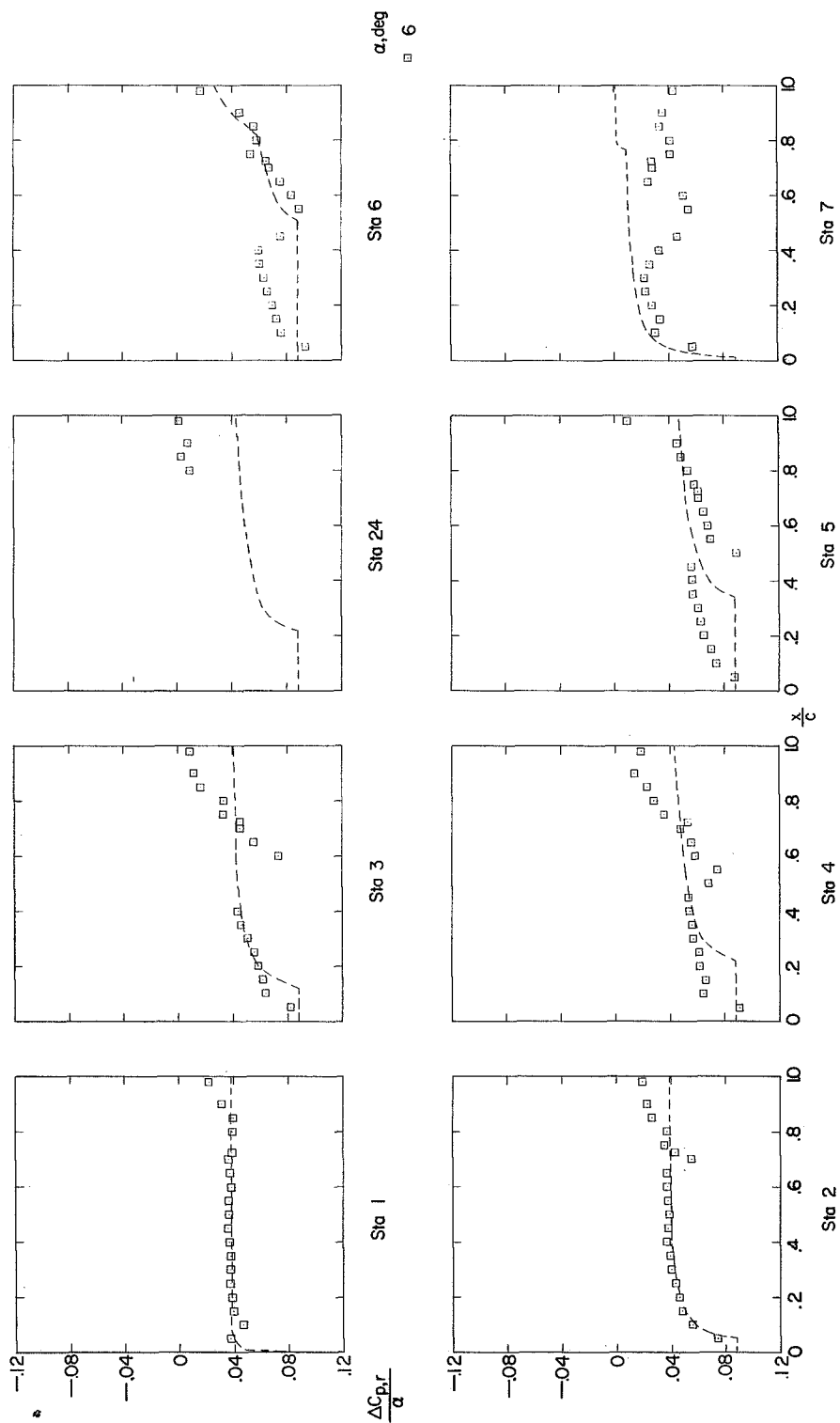
(a) $\delta = 0^\circ$.

Figure 20.- Incremental resultant chordwise pressure distributions due to angle of attack for configuration 3. Dashed lines indicate linear-theory predictions. $M = 1.61$; $R = 3.6 \times 10^6$.



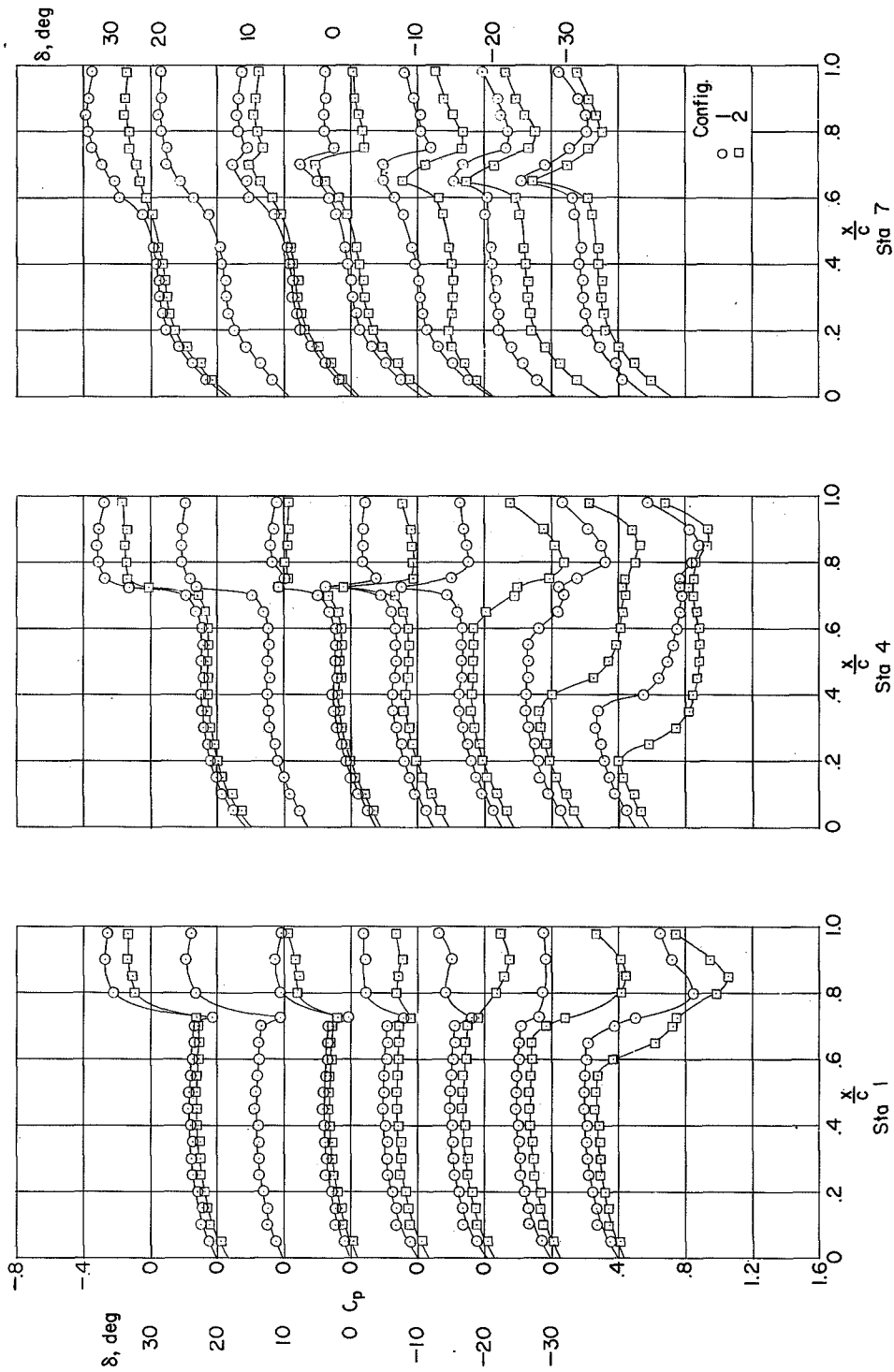
(b) $\delta = 10^\circ$.

Figure 20.- Continued.



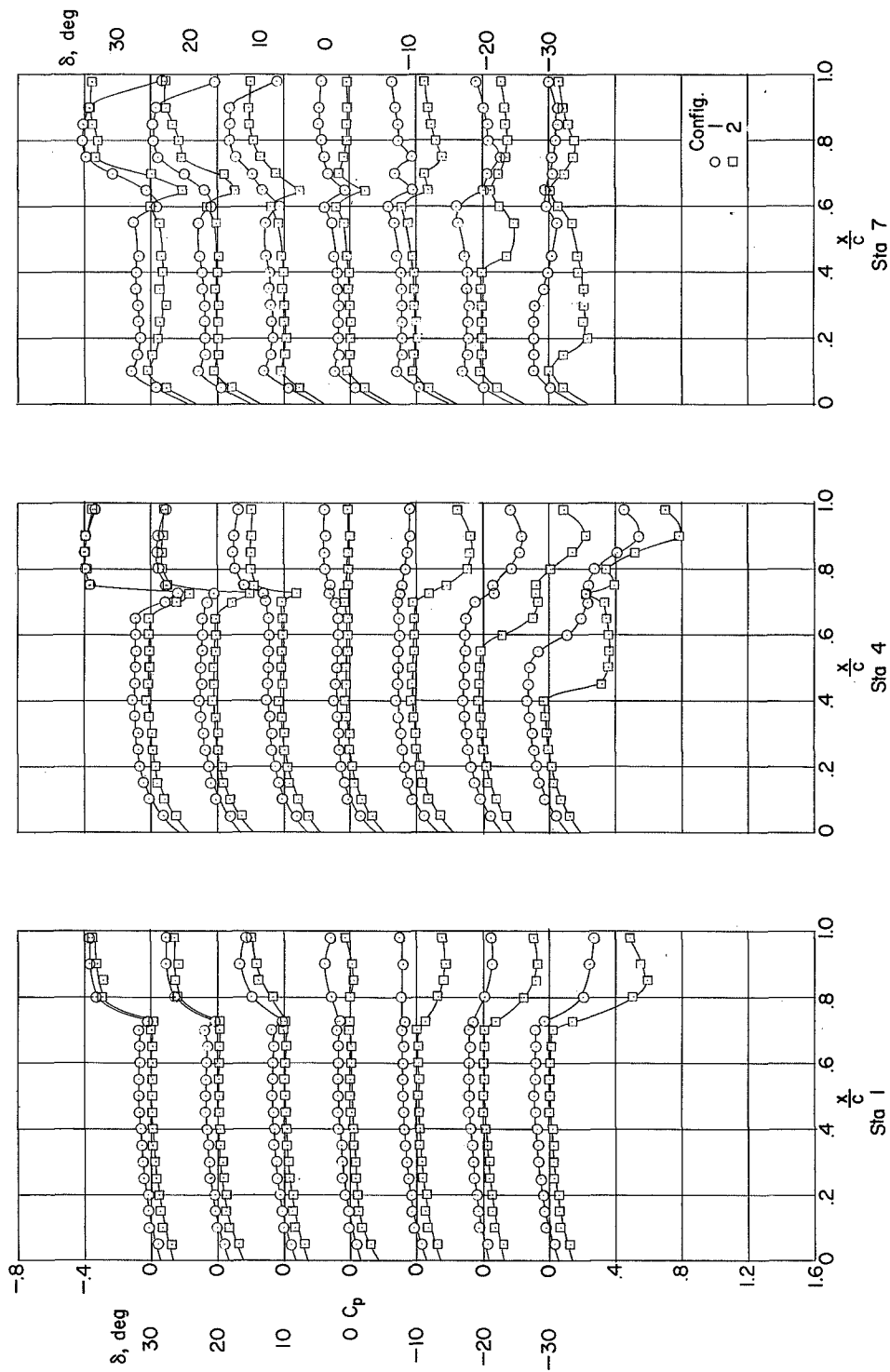
(c) $\delta = 300^\circ$

Figure 20.- Concluded.



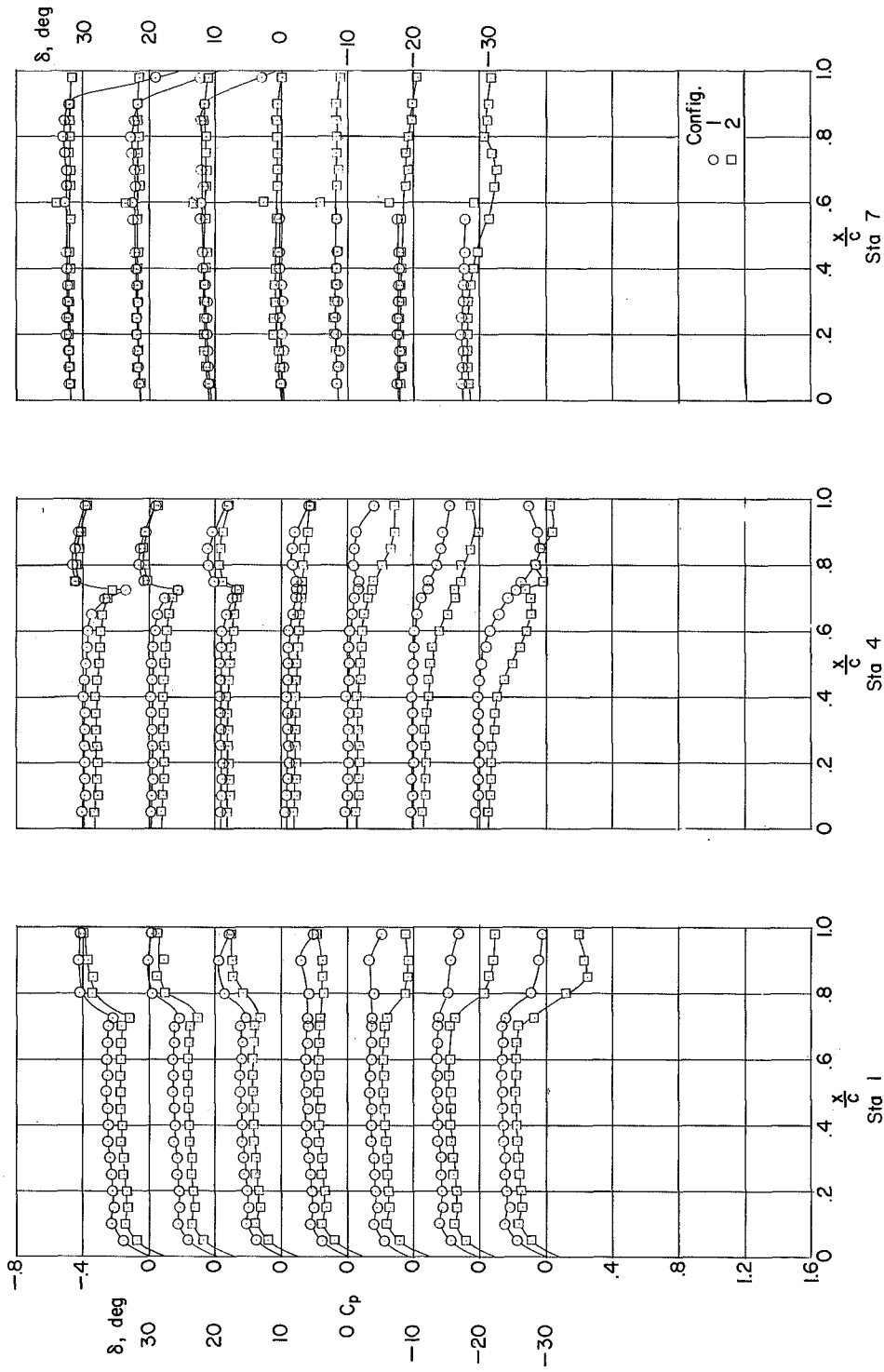
(a) $\alpha = -12^\circ$.

Figure 21.- Comparison of the chordwise pressure distributions for configuration 1 (sharp trailing edge) with those for configuration 2 (blunt trailing edge). $M = 1.61$; $R = 1.7 \times 10^6$.



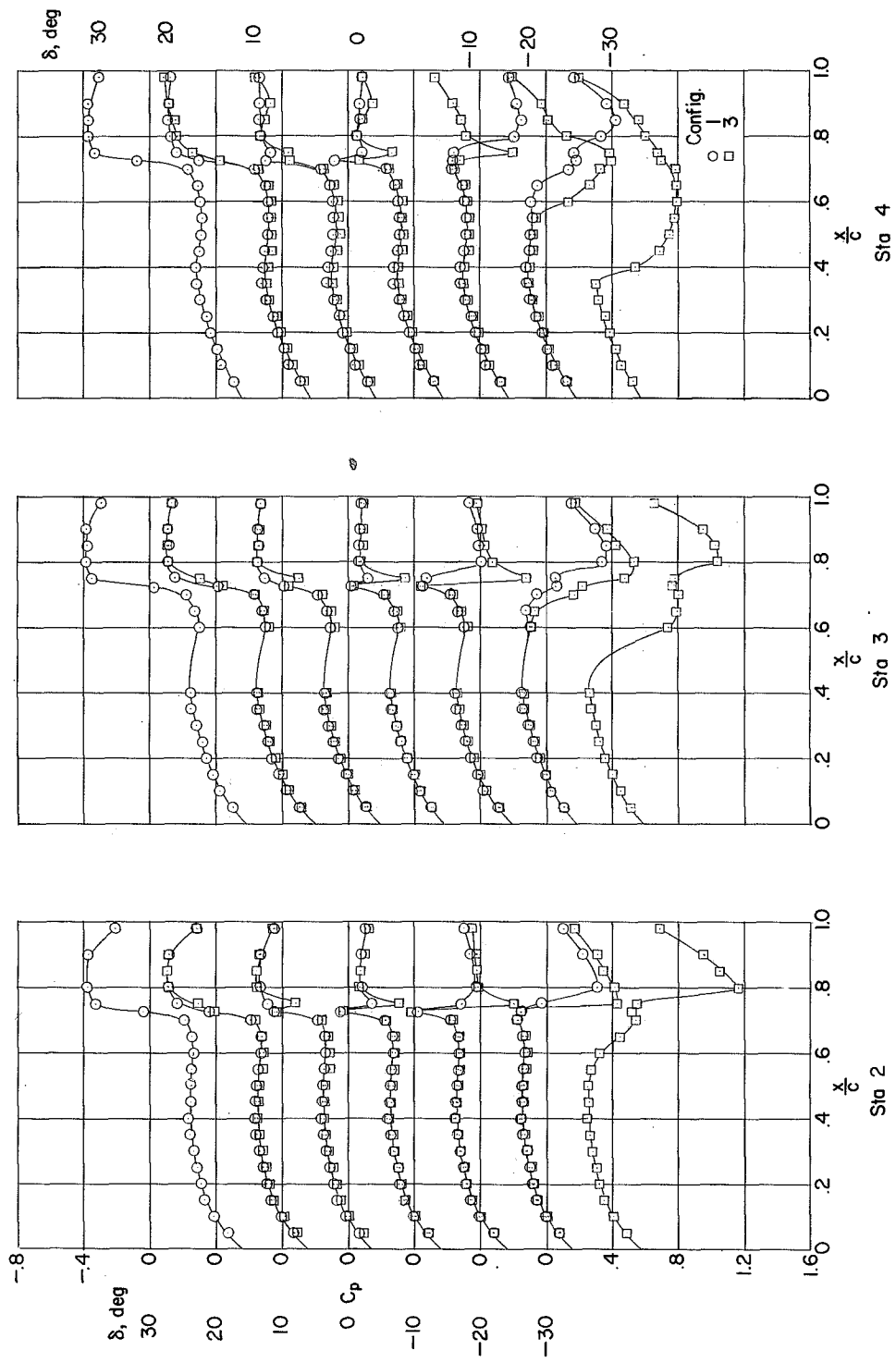
(b) $\alpha = 0^\circ$.

Figure 21.- Continued.



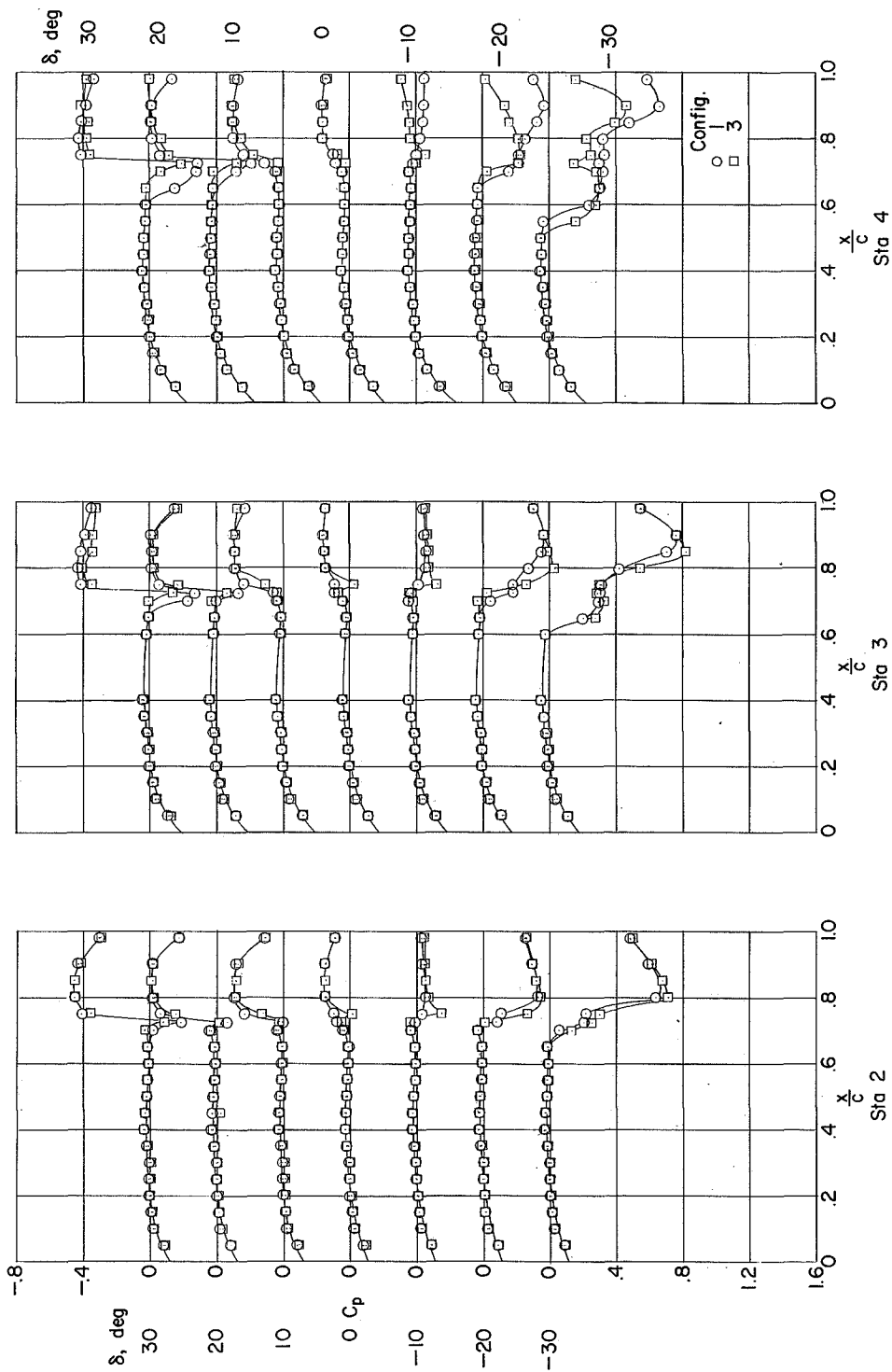
(c) $\alpha = 12^\circ$

Figure 21.- Concluded.



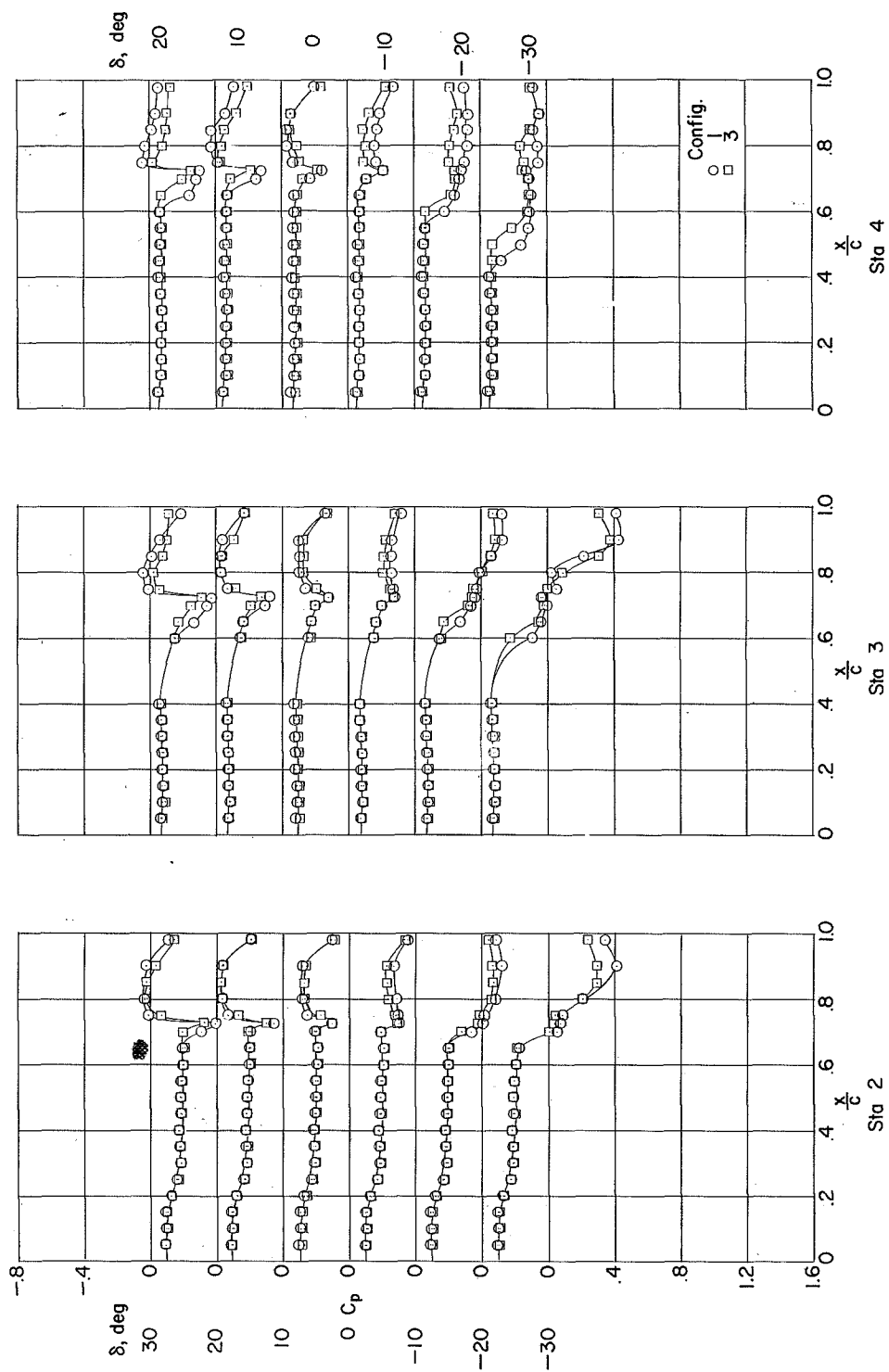
(a) $\alpha = -12^\circ$.

Figure 22.- Comparison of the chordwise pressure distributions for configuration 1 (full-span control) with those for configuration 3 (half-span control). $M = 1.61$; $R = 3.6 \times 10^6$.



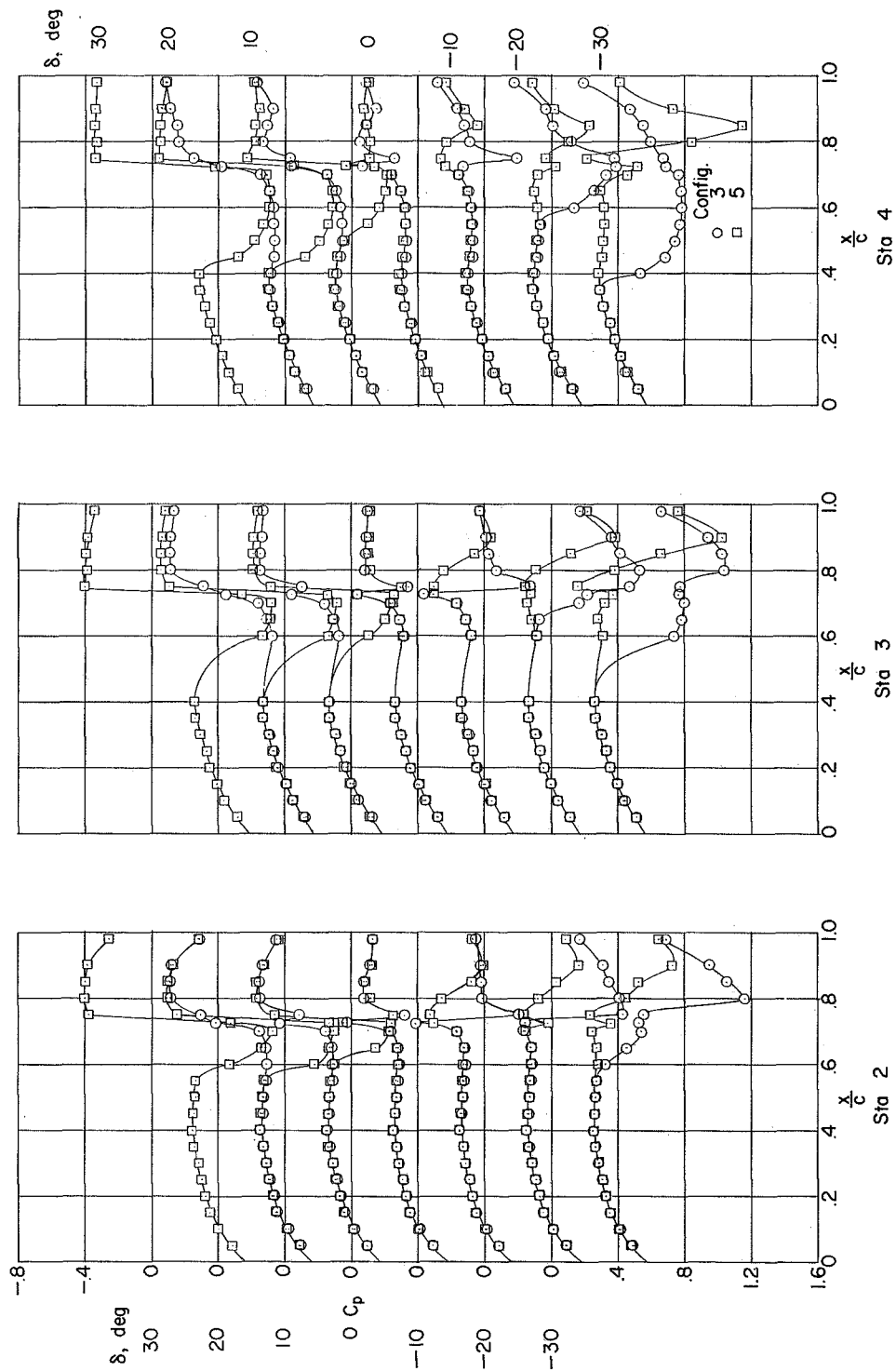
(b) $\alpha = 0^\circ$.

Figure 22.- Continued.



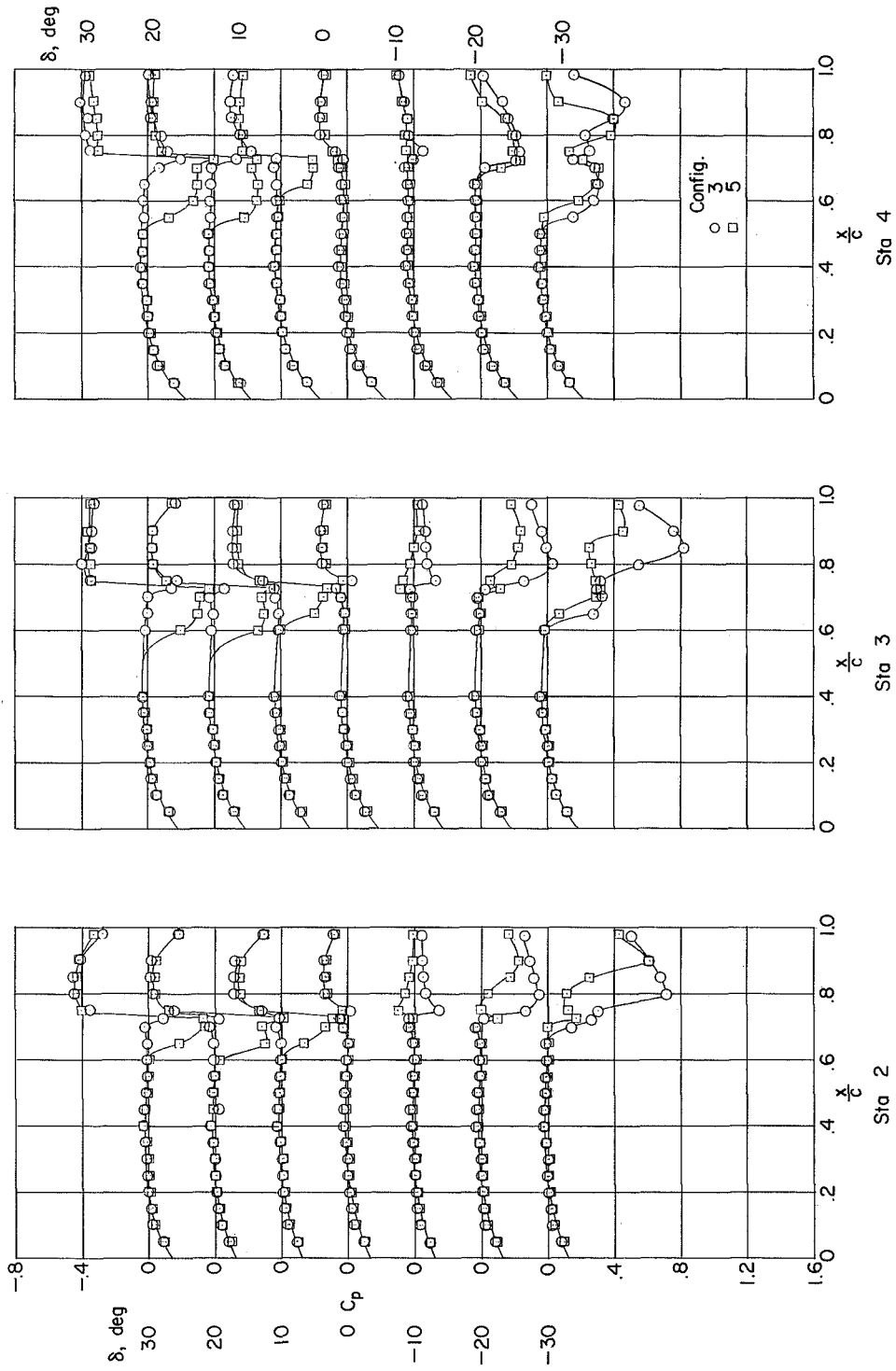
(c) $\alpha = 12^\circ$.

Figure 22.- Concluded.



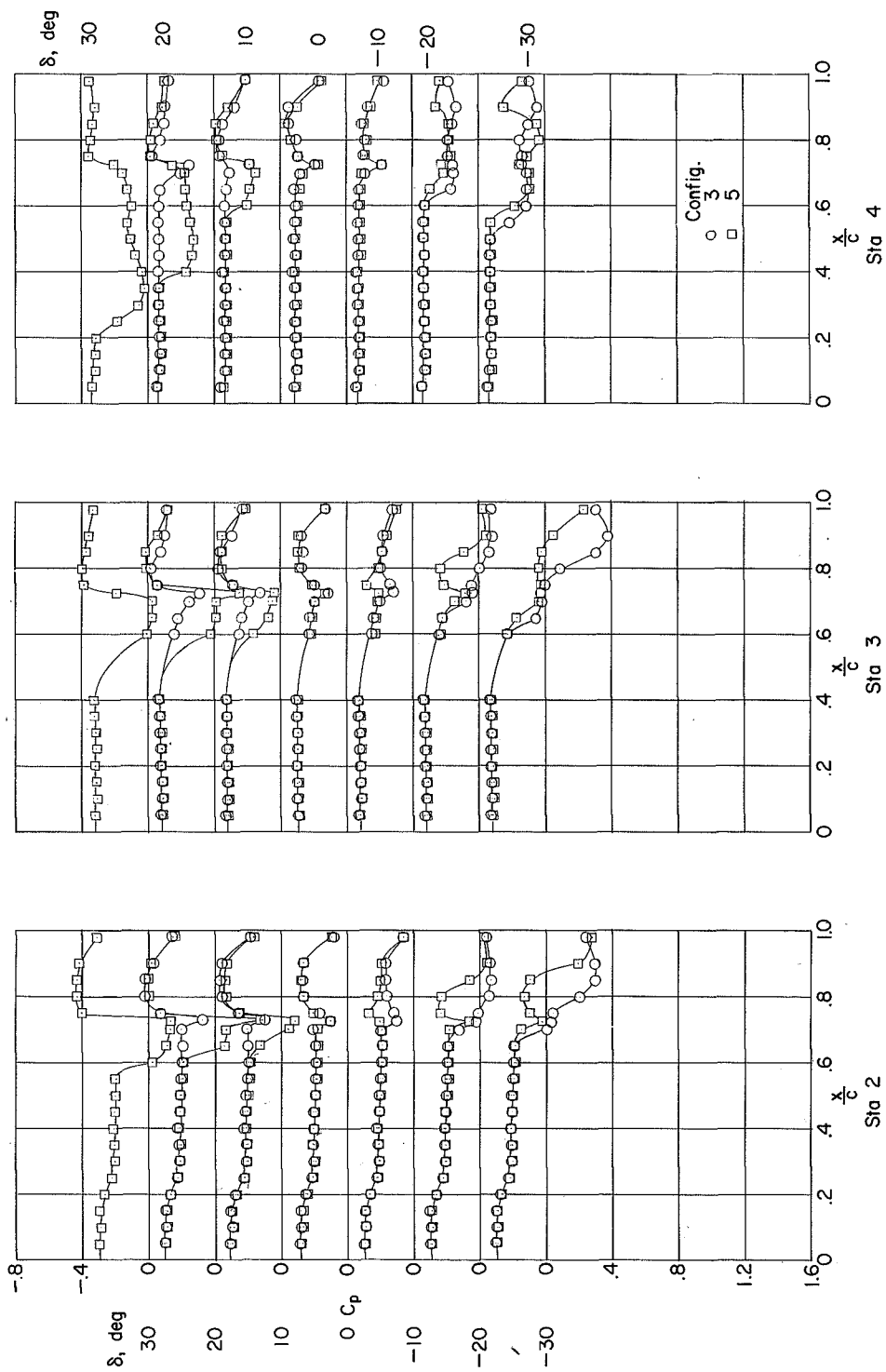
(a) $\alpha = -12^\circ$.

Figure 23.- Comparison of the chordwise pressure distribution on the controls for configuration 3 (hinge line at $x/c = 0.75$) with those for configuration 5 (hinge line at $x/c = 0.875$).



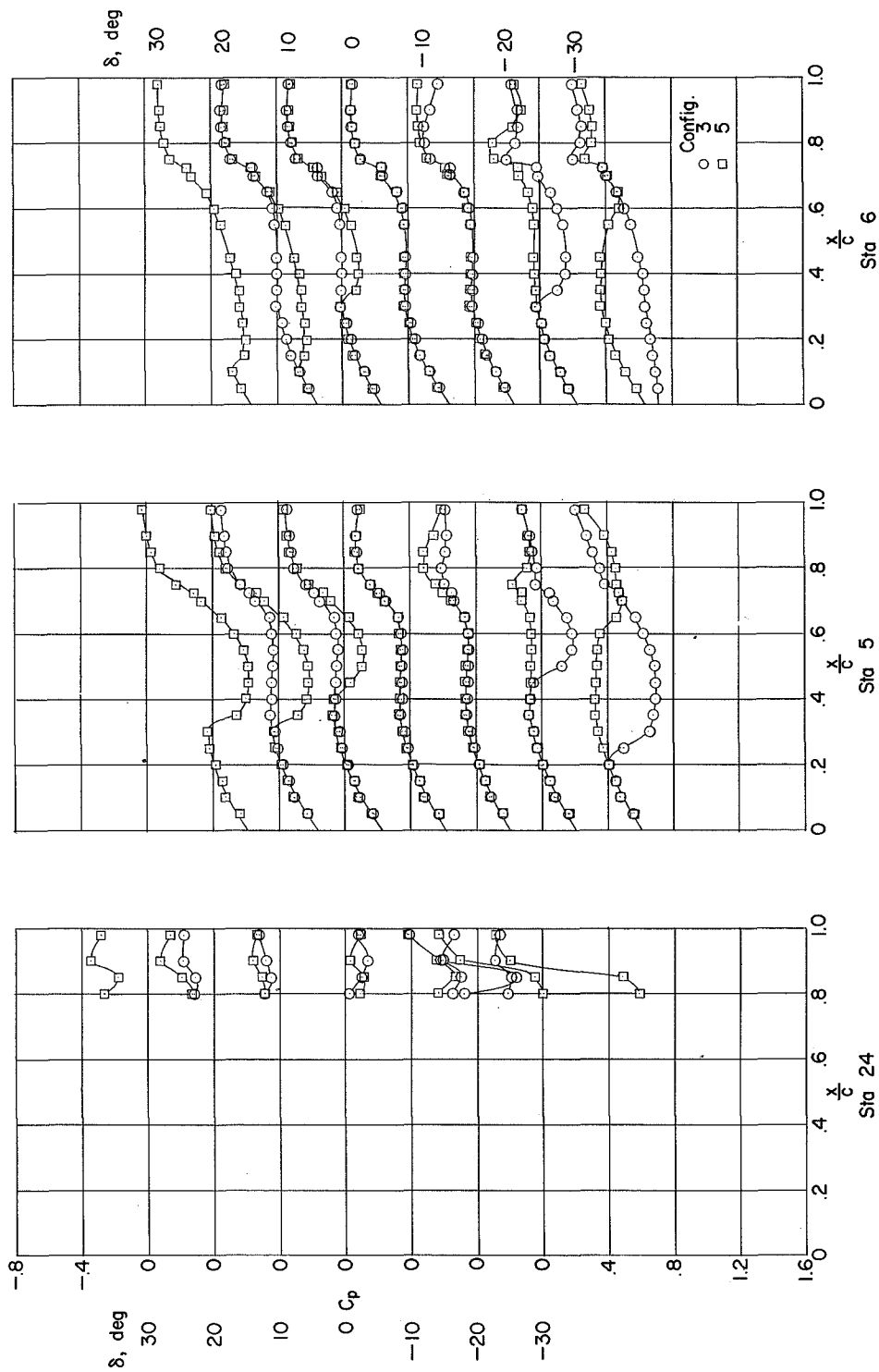
(b) $\alpha = 0^\circ$.

Figure 23.- Continued.



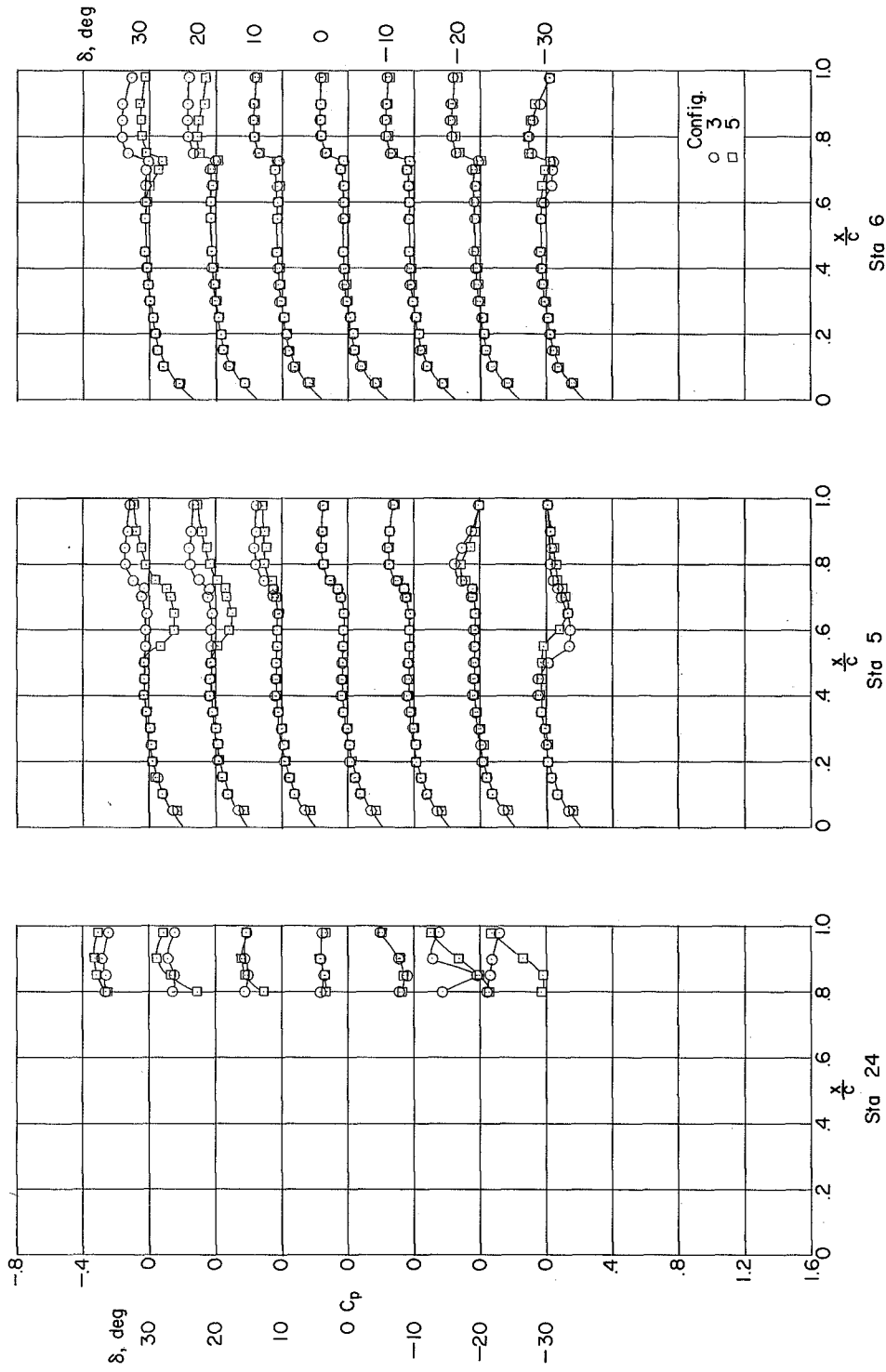
(c) $\alpha = 12^\circ$.

Figure 23.- Concluded.



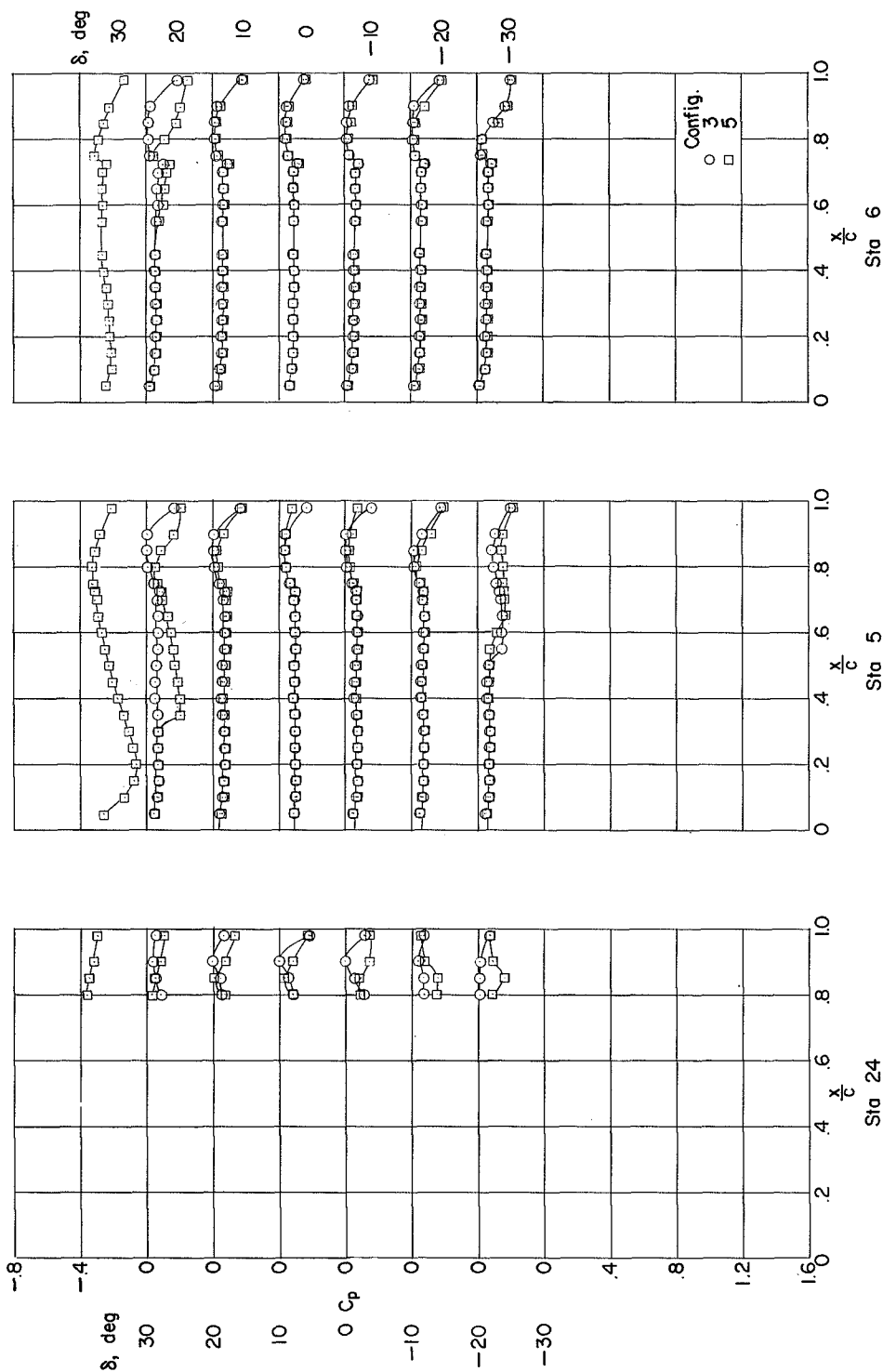
(a) $\alpha = -12^\circ$.

Figure 24.- Comparison of the chordwise pressure distribution outboard of the controls for configuration 3 (hinge line at $x/c = 0.75$) with those for configuration 5 (hinge line at $x/c = 0.875$). $M = 1.61$; $R = 3.6 \times 10^6$.



(b) $\alpha = 0^\circ$.

Figure 24.- Continued.



(c) $\alpha = 12^\circ$.

Figure 24.- Concluded.

